UNIVERSITY OF CALIFORNIA
RIVERSIDE

Mitochondrial Dynamics in the Demyelinating Cerebellum

A Dissertation submitted in partial satisfaction
of the requirements for the degree of

Doctor of Philosophy

in

Biomedical Sciences

by

Kelley Christine Atkinson

September 2021

Dissertation Committee:
Dr. Seema Tiwari-Woodruff, Chairperson
Dr. Edward Zagha
Dr. Iryna Ethell

The Dissertation of Kelley Christine Atkinson is approved:

_____

_____

_____

Committee Chairperson

University of California, Riverside

Acknowledgements

To Dr. Seema Tiwari-Woodruff: Thank you so much for supporting me and mentoring me these past five years.

To Dr. Ethell and Dr. Zagha: Thank you so much for your mentorship and guidance.

To the Tiwari-Woodruff lab: Thank you all for the fun memories. I will always remember the laughter, the conversation, and all the help you gave me.

To dad, mom, Kailynne and Mike: Thank you for pushing me to be the best person I can be and for always believing in me. I love you.

The research for these studies was generously funded by the National Multiple Sclerosis Society and the National Institutes of Health.

The text of Chapter 6 of this dissertation is a reprint of the material as it appears in the Journal of Neurobiology of Disease 2019 (Chapter 6). The co-author Dr. Seema Tiwari-Woodruff listed in those publications directed and supervised the research that forms the basis for this dissertation.

Dedication

To my family.

ABSTRACT OF THE DISSERTATION

Mitochondrial Dynamics in the Demyelinating Cerebellum

by

Kelley Christine Atkinson

Doctor of Philosophy, Graduate Program in Biomedical Sciences
University of California, Riverside, September 2021
Dr. Seema Tiwari-Woodruff, Chairperson

Multiple Sclerosis (MS) is an autoimmune demyelinating disease of the central nervous system that leads to significant motor, cognitive and visual disability. Approximately 80% of MS patients have inflammatory demyelination within the cerebellum and present with tremors, impaired motor control and loss of coordination. While most MS patients exhibit symptoms indicative of cerebellar dysfunction, the pathophysiology of cerebellar symptoms in MS is complex and remains to be elucidated. Purkinje cells (PCs) are a class of myelinated gamma- aminobutyric acid (GABA)ergic neurons located solely in the cerebellum. These specialized neurons are the sole output of the cerebellar cortex and thus are an essential component of cerebellar circuitry. I hypothesize that, while immune cell infiltration and demyelination have been shown to

contribute to PC dysfunction, another source of PC dysfunction may arise directly from metabolic deficits due to mitochondrial pathology. PCs require higher metabolic activity due to their extensively branched dendritic arbors in addition to the large number of glutamatergic inputs they receive from climbing and parallel fiber innervation. Mitochondrial dysfunction in neurons has been shown to contribute to MS disease mechanisms, as shown in human post-mortem MS brain tissue. Understanding the pathology and repair of dysfunctional Purkinje cells (PCs) will aid in the search for reparative and regenerative therapeutic approaches in MS patients. In this dissertation, I will test my hypothesis by investigating the role of cerebellar dysfunction during disease progression in both the experimental autoimmune encephalomyelitis (EAE) and cuprizone mouse models of MS while also assessing the treatment effects of Chloroindazole, an estrogen receptor beta (ERβ) ligand that has previously been shown to stimulate myelination and neuroprotection. Understanding the pathophysiology of mitochondria dysfunction in mouse models of MS while also elucidating the mechanism of action of remyelinating drugs on mitochondria for neuroprotection will help us identify superior therapeutics and improve the quality of life for patients with MS.

Table of Contents

List of Figures

Chapter 1

Chapter 3

Chapter 4

Chapter 5

Chapter 6

List of Tables

Chapter 2

Chapter 1: Introduction

Cerebellar dysfunction and multiple sclerosis (MS)

Multiple sclerosis (MS) is a demyelinating, autoimmune, inflammatory disease of the central nervous system (CNS) that affects 2.3 million people worldwide and leads to chronic disability (Browne et al., 2014). Approximately 80% of MS patients have inflammatory demyelination within the cerebellum and during their lifetime presented with tremors, impaired motor control and loss of coordination (Kurtzke et al., 1977; Weinshenker et al., 1991; Koch et al., 2007). In addition, primary progressive MS (PPMS) and secondary progressive MS (SPMS) patients exhibit abundant cerebellar cortex demyelination in postmortem tissue, which is correlated with earlier death (Weinshenker et al., 1991; Kutzelnigg et al., 2007). While most MS patients exhibit symptoms indicative of cerebellar dysfunction, the pathophysiology of cerebellar symptoms in MS is complex and remains to be fully elucidated.

Purkinje cells (PCs) are a class of myelinated gamma-aminobutyric acid (GABA)ergic neurons located solely in the cerebellum (Morton and Bastian, 2004). These specialized neurons are the sole output of the cerebellar cortex and proper function is finely calibrated to maintain normal cerebellar function (de Solages et al., 2008; Wise et al., 2010; Person and Raman, 2012). PCs have shown alterations in MS postmortem tissue. PC loss and demyelination have been found within cerebellar lesions (Kutzelnigg et al., 2007; Redondo et al., 2015). In addition, PCs show fusion and heterokaryon formation in

MS postmortem tissue, possibly due to the inflammatory environment, to initiate neuronal repair (Kemp et al., 2012). Furthermore, PCs in MS present with aberrant expression of $Na_v1.8$, a voltage-gated Na^+ channel that rapidly recovers from inactivation normally found in unmyelinated C type nociceptive fibers in the periphery (Black et al., 2000). All of these alterations likely contribute to more spontaneous PC firing and further PC dysfunction (Shields et al., 2012). Due to these, PC dysfunction in MS can be deleterious to CNS circuitry.

PCs require higher metabolic activity due to their extensively branched dendritic arbors in addition to the large number of glutamatergic inputs they receive from climbing and parallel fiber innervation (Rolfe and Brown, 1997; Budd and Nicholls, 1998). Myelination of PCs provides trophic support to PC axons and facilitates rapid saltatory conduction to deep cerebellar nuclei (DCN) (Baumann and Pham-Dinh, 2001; Haines et al., 2011; Herbert and Monk, 2017). PCs show spontaneous electrophysiological activity in the form of simple and complex spikes that are Na^+- and Ca^{2+}-dependent that could be altered by demyelination and increased energy demand (Llinás and Hess, 1976; Llinas and Sugimori, 1980).

Mitochondria dysfunction and MS

While several elements are known to contribute to the neurodegeneration observed in MS, one factor that has been evident in MS as well as other neurodegenerative diseases is

mitochondria dysfunction. In the context of MS, the loss of myelin contributes to a loss in saltatory conduction and an increased energy demand needed for the axon to maintain its resting membrane potential (Shepherd, 1988; Waxman and Black, 1995; Kaplan et al., 1997). The CNS has an extremely highly metabolic rate and it consumes about 20% of oxygen at rest while only accounting for 2% of total body weight (Silver and Erecińska, 1998), meaning even slight changes in energy demand could be deleterious for the CNS as a whole.

Mitochondria have an outer mitochondrial membrane (OMM), inner mitochondrial membrane (IMM), and the matrix (**Figure 1A**). The IMM is where the electron transport chain (ETC) is located and where adenosine triphosphate (ATP) production occurs (Wallace, 1992; Elston et al., 1998; Cheng et al., 2010; Ross et al., 2013). The ETC pumps protons from the mitochondrial matrix into the intermembrane space. This creates an electrochemical proton gradient across the IMM, providing ATP in addition to helping maintain the mitochondria membrane potential (MMP; $\Delta\Psi_m$). Maintaining the MMP is essential. A low MMP is associated with limited ATP, low superoxide production, and mitochondria elimination with mitophagy, while a high MMP boosts ATP synthesis and superoxide production (Klingenberg, 1980; Korshunov et al., 1997; Lambert and Brand, 2004; Chinopoulos et al., 2009; Geisler et al., 2010; Belenguer et al., 2019).

Mitochondria are the only organelles in eukaryotic cells that have their own unique DNA, mitochondrial DNA (mtDNA), which is distinct from nuclear DNA. mtDNA encodes 13 polypeptides and features 4 of the 5 respiratory chain complexes (Taylor and Turnbull, 2005; Islam, 2017) and is inherited maternally (Youle and Van Der Bliek, 2012). Mitochondria contain multiple copies of mtDNA that encode for genomic expression. Notably, this mitochondrial genome is not protected by histones, making its mutation rate higher than nuclear DNA (Islam, 2017). Human mtDNA is a circular molecule of 16,569 base pairs that encodes the rRNAs and tRNAs necessary to support intramitochondrial protein synthesis using its own genetic code (Lin and Beal, 2006). This multi-copy nature is explained by heteroplasmy- where both mutated and wildtype mtDNA coexist in the same cell (Fetterman and Ballinger, 2019).

In addition to producing ATP, mitochondria have additional functions vital to cells such as regulating oxidative stress, intracellular Ca^{2+} signaling homeostasis, and steroid synthesis (Rottenberg and Scarpa, 1974; Giacomello et al., 2020). Ca^{2+} storage in mitochondria is involved in the regulation of ion homeostasis, cell signaling, and apoptosis (Glancy and Balaban, 2012). These are all critical for cells in the CNS, especially neurons due to these cells' high metabolic rate and increased sensitivity to oxidative damages (Kann and Kovács, 2007). Furthermore, neurons require ATP for proper execution of neurotransmission and plasticity (Bordone et al., 2019). Due to this,

proper neuronal development and survival are highly dependent on mitochondria function.

All of these functions claim to be altered in neurons or oligodendrocytes in MS postmortem tissue and animal models of MS due to changes in energy demand and energy production (Witte et al., 2009). While some studies appear to be assessed in neurons in postmortem tissue, many are actually only performed in human cell lines (Li et al., 2013). Witte et al. shows an increase in mitochondrial numbers in active lesions in astrocyte and axons using immunohistochemistry co-localization, which may be the best way to assess mitochondrial pathology in specific cell types (Witte et al., 2009). There are few studies that have assessed mitochondrial function in specific cell types in animal models (Madsen et al., 2017).

Mitochondrial fission/fusion

Mitochondrial dynamics is a broad term to describe how mitochondria fission and fusion regulate number, morphology, and positioning changes within a cell. Mitochondrial fission is defined as the division of one mitochondrion into two daughter mitochondria, while fusion is the union of two mitochondria resulting in one mitochondrion (Detmer and Chan, 2007; Chen and Chan, 2009; Garone et al., 2018). These two factors allow for this organelle to adapt to cell need at any given time and are

regulated by a variety of cellular pathways including proteolytic processing, ubiquitylation, SUMOylation, phosphorylation and dephosphorylation (Van der Bliek et al., 2013). When fusion or fission occur, the proteins are catalyzed by guanosine triphosphate (GTP)ase enzymes. In mammals, mitochondrial fission is mediated and controlled by dynamin-related protein 1 (Drp1) and dynamin 2 (Dnm2) (**Figure 1B**). Fusion has two GTPases which control the OMM, mitofusins 1 and 2 (Mfn1, Mfn2), while the IMM is controlled by optic atropy 1 (OPA1) in mammals (Chen et al., 2010). All of these proteins are important for maintaining cellular and mitochondrial function (Chen and Chan, 2009; Westermann, 2010; Barcelos et al., 2019). Too much mitochondrial fission will cause fragmented-like mitochondria that are elongated and thin, and too much mitochondrial fusion will cause a shortage in energy production in the cell (Youle et al. 2012). In addition, Drp1 is important for synapse formation in mice, and Mfn2 is protective against neurodegeneration (Ishihara et al., 2009).

Fission in mammals is dependent on the main regulator Drp1 which consists of 4 domains: the N-terminal GTPase domain, a middle assembly domain, a B/variable domain (Garone et al., 2018), and a C-terminal GTPase effector domain (GED) (Chang et al., 2010; Van der Bliek et al., 2013; Hu et al., 2017). Drp1-dependent mitochondrial fission consists of translocation of Drp1 to the OMM, subsequently higher-order assembly, GTP hydrolysis, and disassembly (Hu et al., 2017). Drp1's ability to bind to receptors on the OMM is mediated by the central stalk of the middle assembly domain to form a complex of Drp1 oligomeric helices (Garone et al., 2018). These Drp1 complexes

can move along the mitochondria tubule, inducing constriction and then fission (Westermann, 2010; Van der Bliek et al., 2013; Liu et al., 2020). Recruitment of Drp1 by mitochondrial fission factors Mff (Mff) regulate the division by recruiting Drp1 that oligomers into ring-like structures with GTP hydrolysis, contributing to the conformational change and mitochondrial constrictions.

Mitochondria fusion is controlled by two large GTPases, one controlling the OMM and the other the IMM. This process is characterized by three steps which include the tethering of the two mitochondria, the docking of the two membranes (IMM and OMM), and fusion of the two OMM (Garone et al., 2018). When GTP binds to its domains, Mfn undergoes a conformational change that allows for mitochondria docking and an increase of membrane contact sites. The mitofusins contain GTP-binding domains that anchor onto the OMM by a C-terminal transmembrane domain. The OMM of the opposing mitochondria gets tethered by the interaction of the GTPase domains of Mfns. Fusion of the OMM is driven by GTP hydrolysis and GTP-dependent oligomerization, which is responsible for inducing Mfn's conformational changes, bringing the two membranes in contact with one another leading to mitochondria docking. This change also increases the membrane contact sites. Following OMM fusion, OPA1 drives IMM fusion with the help of a mitochondria-specific lipid, cardiolipin (CL) (Liu et al., 2020). The interaction between OPA1-CL on either side of the membrane tethers the two inner membranes following OPA1-dependent GTP hydrolysis (Liesa et al., 2009). It is important to note that IMM fusion occurs downstream of OMM fusion. Mfn2 is said to be present in the

ER and controls the tethering of the ER onto the mitochondria which is observed in the mitochondrial constriction of the fission process (Liu et al., 2020).

Mitochondrial Transport

Mitochondria depend on proper axon function to be transported to areas of high demand. Axons contain two types of mitochondria: stationary mitochondria and mobile mitochondria. In a healthy neuron, 70% of mitochondria are stationary and are generally found in areas of high ATP consumption (Fabricius et al., 1993). The 30% of mobile mitochondria are thought to move at a speed of 1 μm/s (Kiryu-Seo et al., 2010). In the axon, mitochondria are mostly stationary until they are regulated by intracellular signals (Hollenbeck and Saxton, 2005). Mitochondria are then delivered to regions of high demand by moving along microtubule and actin tracts with the assistance of kinesin and dynein proteins (Hollenbeck and Saxton, 2005). Anterograde axonal transport is largely mediated by kinesin superfamily motor proteins which hydrolyze ATP to generate motile forces to shift cargos along the axon via microtubule tracks (Brady, 1985). This type of transport is pertinent to axonal health, as this transport is required for organelles, lipids, and proteins (Barnett et al., 2016). Retrograde transport is largely mediated by dynein superfamily motor proteins and is important for degradation products that need to travel back towards the soma (Barnett et al., 2016). Once mitochondria are transported where they need to be, they are immobilized with syntaphilin (snph), a static anchor specific for axonal mitochondria, to keep mitochondria stationary in the axon. Without snph

mitochondria become mobile and move along microtubule tracts within the axon (Ohno et al., 2014). In addition, snph appears to be required for the increase in axonal mitochondrial volume in snph-deficient myelinated axons (Ohno et al., 2014).

Mitochondria dynamics in MS postmortem tissue

Currently, alterations in mitochondria dynamics in humans can only be observed in postmortem tissue. Mitochondrial proteins, mitochondrial enzyme activity, and mtDNA mutations have been measured using immunohistochemical and biochemical techniques. While MS postmortem tissue has been reviewed extensively, MS patients display heterogeneity in their symptoms, lesions, and disease-modifying treatments, meaning conclusions from these studies can be vague and oversimplified (Campbell and Mahad, 2011; Barcelos et al., 2019). In addition, the postmortem delay can range from a few hours up to 24 hours, thus making analyses with postmortem tissue very convoluted. However, mitochondria dynamics in MS postmortem tissue appear consistent, depending on the type of lesions and MS the patients presented with. We summarized the mitochondria findings from human MS postmortem tissue in **Table 1**.

Immunohistochemistry (IHC) is used for most postmortem studies to indicate mitochondrial involvement during multiple sclerosis. In chronic active MS lesions, one study observed increased mitochondria content (measured by porin) compared with

myelinated axons. However, there was no difference in axonal mitochondrial content between remyelinated and demyelinated axons in remyelinated regions close to demyelinated areas in chronic MS lesions (Zambonin et al., 2011). In addition, a reduction in mitochondrial content was observed in shadow plaques compared with chronically demyelinated axons in MS lesions (Zambonin et al., 2011). Another study found respiratory deficient neurons that were prevalent within the dorsal root ganglia in progressive MS, termed as mitochondria that lacked COXIV but contained COXII (Licht-Mayer et al., 2020). These respiratory deficient neurons also had increased mitochondria content, size, and number (Licht-Mayer et al., 2020). While several studies have demonstrated changes in mitochondrial pathology in postmortem tissue, IHC only shows a snapshot at one timepoint. In addition, tissue integrity is highly dependent on the time of death, because a brain not extracted right away will show more pathological cell and mitochondrial stress.

In postmortem tissue, co-staining with immunohistochemistry showed a decreased COXIV expression in pattern III MS lesions in axons, astrocytes, and oligodendrocytes (Mahad et al., 2008). In addition, decreased COXIV activity was observed in axons in the rim of chronic active lesions, while axons within inactive lesions displayed increased activity of COXIV (Mahad et al., 2009). However, another study found the opposite result. Mitochondrial protein expression and enzyme activity were investigated in active and inactive chronic MS lesions with adjacent normal appearing white matter (NAWM)

using immunohistochemistry (IHC) (Witte et al., 2009). COXIV activity was upregulated in MS lesions compared to control white matter and NAWM with an additional increase in mtHSP70, a mitochondrial stress protein (Witte et al., 2009). In addition, mitochondrial density in axons and astrocytes was increased in areas with active lesions compared to NAWM with a trend in inactive lesions. The variation in COXIV expression between the groups may be due to the type of lesions in both studies. Pattern III lesions are characterized by extensive oligodendrocyte apoptosis and hypoxia-like tissue injury (Lucchinetti et al., 2000). The MS postmortem tissue used in the study by Witte and colleagues did not have hypoxia-like damage or oligodendrocyte apoptosis. In addition, while Mahad and colleagues demonstrated an increase in COXIV activity in active lesions, they measured this particularly in axons, while Witte and colleagues measured COXIV activity in the entirety of the active lesion. Axonal COXIV activity may be overall decreased, but total COXIV activity in MS lesions may be increased. In addition to ETC changes, an upregulation of SNPH was observed in tissues from progressive MS patients compared to healthy patients (Mahad et al., 2009). While all of these studies clearly show mitochondrial involvement during MS, the extent and timeline of all of these studies is also dependent on the type of MS and the course of disease the patient had during their lifetime.

Mitochondria DNA (mtDNA) mutations and expression have been implicated in MS postmortem tissue and has been discussed in (Campbell and Mahad, 2018). The

importance of mtDNA for maintaining a healthy CNS is highlighted by a number of primary mtDNA disorders, where the entire nuclear DNA-encoded complex of mitochondrial respiratory chain, complex II, is spared (DiMauro and Schon, 2003; Zeviani and Di Donato, 2004). Neurons in postmortem secondary progressive (SP)MS tissue have also demonstrated mtDNA deletions and are respiratory deficient with decreased COXIV, which could be a major contributor to neurodegeneration. These changes were extensive in the gray matter (Campbell et al., 2011). In addition, specific mtDNA variants and changes in mtDNA copy numbers have been demonstrated in patients with MS (Blokhin et al., 2008; Vyshkina et al., 2008; Yu et al., 2008; Kenney et al., 2014a; Kenney et al., 2014b; Tranah et al., 2015). Furthermore, a subset of nuclear-encoded mitochondria ETC genes were decreased in the SPMS cortex compared to controls, including components for COXI, COXIII, COXIV, and ATP Synthase in upper motor neurons (Dutta et al., 2006). Using quantitative PCR and western blot, reduced levels of PGC-1α, a transcriptional coactivator and master regulator of mitochondrial function, were observed with neuronal loss in the cingulate gyrus and frontal cortex of normal appearing gray matter MS patients, indicating that mitochondria dysfunction could be due partly to PGC-1α (Witte et al., 2013). One group was able to assess the mitochondria proteome in the MS prefrontal cortex using Surface-Enhanced Laser Desorption Ionization Time of Flight Mass Spectrometry (SELDI-TOF-MS) (Broadwater et al., 2011). In addition to differentially expressed COX5B expression with SELDI-TOF-MS, this study demonstrated decreased COX5B expression in its mitochondrial fractions isolated from the cortex with western blot (Broadwater et al., 2011). However,

since this study was from the entire cortex, the COX5B changes could be due to mitochondria in neurons, oligodendrocytes, astrocytes, microglia, and immune cells. Whole-genome sequencing (WGS) from PPMS and healthy subjects of European ancestry detected pathogenic variants exclusively found in PPMS patients that cause hereditary spastic paraplegias that share features with MS (Jia et al., 2018) and are involved with mitochondrial function (Atorino et al., 2003; Zheng et al., 2018).

Altered mitochondrial dynamics in animal models of MS

Due to the complexity of mitochondrial dysfunction in MS, mouse models that demonstrate inflammation, demyelination, and neurodegeneration are important to utilize in order to gain a better understanding of the pathophysiology. Different mouse models of MS such as Experimental Autoimmune Encephalomyelitis (EAE), cuprizone, lysolecithin, and ethidium bromide have been used to discuss mitochondrial dynamics in MS. Each model has caveats because of differences in inflammation and levels of demyelination.

EAE is the best model of MS because it incorporates demyelination, peripheral inflammation and neurodegeneration (Craner et al., 2003; Hasselmann et al., 2017c). This model uses a myelin peptide to induce an autoimmune reaction. This model can cause paralysis in mice and more closely relates to MS; however, the mice can develop lesions

anywhere in the CNS, causing variation between mice in the same cohort. An additional demyelinating model includes the cuprizone (CPZ) diet-induced demyelination. While CPZ does not have peripheral inflammation, this mouse model has consistent demyelination in the corpus callosum and in other regions of the brain after varying amounts of length on the diet (Matsushima and Morell, 2001; Kipp et al., 2009). In addition, when CPZ diet is replaced by a normal diet after a few weeks of demyelination, spontaneous endogenous remyelination occurs, allowing for the study of remyelination. While it is known CPZ is a copper chelator, the true mechanism of CPZ is unknown. However, studies have shown the formation of megamitochondria in the liver tissue of mice. In addition, megamitochondria was observed in oligodendrocytes after 3 weeks (Acs and Komoly, 2012). Mitochondria have also been shown to be enlarged after 6 weeks of cuprizone and in several mouse models of demyelination (Ineichen et al., 2020). Because copper is known to have important roles in the mitochondria ETC (Xu et al., 2013), using CPZ as a method to understand mitochondrial dynamics in the complex of MS disease may be too convoluted. Both of these models, in addition to other models of demyelination such as lysolecithin and ethidium bromide, have been used to understand mitochondrial dynamics in MS. Lysolecithin and ethidium bromide are injected stereotaxically in the CNS and reproducibility of the location and the size of the lesion can also vary. There have been several mitochondrial studies with these mouse models that will be briefly discussed below and are also summarized in **Table 2**.

Demyelination can directly affect mitochondria dynamics due to changes in fission and fusion (Ohno et al., 2014). Fission and fusion are critical to mitochondria because they not only affect mitochondria morphology, but also affect mitochondria distribution within the cell. Drp1 has been effectively studied in both the EAE and CPZ mouse models. Luo et al. observed increased Drp1 expression in the lesioned spinal cord at peak EAE disease and corpus callosum after 6 weeks on the CPZ diet (Luo et al., 2017b; Luo et al., 2017a). Hyper-activation of Drp1 in culture contributed to an increase in mitochondrial fission, however, inhibiting Drp1 activation had a neuroprotective effect in both EAE and CPZ (Luo et al., 2017b). Direct manipulation of mitochondrial proteins by deleting SLC25A46, an OMM protein, showed degenerating dendrites, enlarged mitochondria in Purkinje cells, and decreased ATP production compared to controls (Li et al., 2017). In addition, there was an increase of Mfn2 expression in PLP4e mice, a demyelinating mouse model containing extra copies of myelin genes (Thai et al., 2019). While these studies show direct changes of mitochondria, these changes are only observed after a protein was knocked out or after extra copies of genes are added. Due to the genetic alterations, these studies are unable to translate to human disease and postmortem tissue. Studies also showed decreased mitochondrial complex expression in EAE after depletion of LKB1 from astrocytes (Kalinin et al., 2020).

Mitochondrial transport is altered in demyelinating mouse models (Andrews et al., 2006; Joshi et al., 2015; Ohno et al., 2014). Enhancing axonal mitochondrial transport in snph

knockout (KO) mice was shown to facilitate axon regenerative capacity (Zhou et al., 2016). This was also observed in the dysmyelinating shiverer (*Shi*) mouse model that was crossed with a mouse lacking syntaphilin. *Shi* is often used as a mouse model for progressive MS and also provides metabolic matching by increasing the axonal mitochondrial mass (Andrews et al., 2006). Deletion of snph in the *Shi* mouse model significantly prolonged survival and reduced cerebellar degeneration (Joshi et al., 2015). Interestingly, another study using the cuprizone (CPZ) demyelinating mouse model demonstrated mitochondria immobilization mediated by syntaphilin facilitates the survival of demyelinated axons (Ohno et al., 2014). Demyelinated axons that are also deficient in syntaphilin degenerated at a greater rate than wildtype axons (Ohno et al., 2014). However, deletion of snph did not have an effect in EAE (Joshi et al., 2015). All of these studies show indirect evidence that snph is involved in facilitating the survival of axons and preventing neurodegeneration.

Mitochondria dynamics in other neurodegenerative diseases

As expected, modifications and aberrations of fission and fusion are associated with neurodegenerative diseases such as Autosomal Optic Nerve Atrophy, Parkinson's Disease (PD), Alzheimer's Disease (AD), and Huntington's Disease (HD) (Delettre et al., 2002; Dodson and Guo, 2007; Bossy-Wetzel et al., 2008; Chen and Chan, 2009). Since mitochondrial dysfunction is observed in other neurodegenerative diseases this could be a universal mechanism of neurodegeneration.

Autosomal Optic Nerve Atrophy and PD have demonstrated abnormalities in mitochondrial fission and fusion. Opa1 mutations are reported to be responsible for Autosomal Optic Nerve Atrophy and have been reported to be associated with MS-like disorders in patients (Yu-Wai-Man et al., 2016) based on the McDonald criteria for MS diagnosis. In addition, mutations in Mfn2 caused segmental axonal degeneration without cell body death (Misko et al., 2012). Two genes involved in hereditary PD are Pink1 and Parkin, which are both important in mitochondria integrity (Dodson and Guo, 2007). Mutation or loss of Parkin and PINK1 in human SH-SY5Y cells resulted in exacerbated mitochondrial fragmentation that is mediated by Drp1 (Filichia et al., 2016; Liu et al., 2020). AD and HD have demonstrated morphological and pathological changes with mitochondria. AD patients are known to have abnormalities in mitochondria structure (Baloyannis, 2006). In addition, sporadic AD patients display elongated mitochondria which form collapsed perinuclear networks (Wang et al., 2008; Wang et al., 2009). HD is an autosomal dominant disease caused by a trinucleotide expansion (cytosine, adenine, and guanine [CAG]) within the huntingtin (Htt) gene. There is evidence that the expression of mutant Htt is associated with mitochondrial dysfunction (Chen and Chan, 2009). Specifically, Htt expression correlated with decreased MMP, decreased COXII, reduced mitochondrial mobility and mitochondrial ultrastructural changes (Bossy-Wetzel et al., 2008).

The difficulty in assessing mitochondria with the available and published techniques

Most studies of mitochondrial dynamics rely on cultured cells, where mitochondria can be imaged at a high resolution. This poses a problem, as *in vitro* studies do not thoroughly represent what occurs in disease. The main difficulty in studying mitochondria in MS is the lack of animal models and techniques available to fully understand mitochondrial dynamics during disease progression. The use of animal models to study mitochondria could address these issues, however, there are still limitations to studying mitochondrial pathology. Here is a summary of several techniques used in order to probe the understanding of mitochondrial dynamics within the context of MS disease. **Table 3** lists techniques used to measure mitochondria activity *in vitro* and *in vivo.*

To visualize mitochondria density, morphology, shape, and cristae complexity in a specific region of the CNS, transmission electron microscopy (TEM) is often used. The demyelination model and timepoint after inducing demyelination contributes to a variety of results that have been previously published. In an ethidium bromide demyelination model in the caudal cerebellar peduncle in rats, there was an increase in mitochondria density in remyelinated axons compared to demyelinated axons with EM, indicating a modulation of energy dynamics after remyelination (Zambonin et al., 2011). Using a proteolipid protein (PLP1)-overexpressing mouse model, there was an increase in axonal mitochondrial density in the PLP1-overexpressing mice compared to the normal mice

(Hogan et al., 2009). An increased density of mitochondria was also observed in Purkinje cell soma in the dysmyelinated *Shi* model (Joshi et al., 2015). One EAE study demonstrated vacuolization and dissolution of mitochondrial cristae evident in optic nerve mitochondria 10 days post induction (dpi) (Qi et al., 2006). Using a focal axon demyelinating model of MS, mitochondria appeared swollen with TEM 6 dpi (Nikic et al., 2011). Furthermore, with an acute oxidative stress model, axonal mitochondria were more round with more complex cristae after acute oxidative stress 24 hours after exposure (Errea et al., 2015). This study used extensive quantification to calculate mitochondrial circularity and roundness. Three dimensional (3D) EM can be utilized as well to determine mitochondria morphology and size 3D. Using 3D EM, there was an increase in mitochondria numbers in the P_0 CNS juxtaparanodal axon with the mitochondria also shorter and thicker, calculated in microns (Yin et al., 2016). Another study used 3D EM and demonstrated larger and longer mitochondria in demyelinated axons, but snph-KO mice had shorter and thicker mitochondria compared to controls (Ohno et al., 2014). While TEM and 3D EM are advantageous to understand mitochondrial morphology, we can only infer how the morphology relates to mitochondria dynamics and function.

One of the best ways to observe mitochondria in distinct cell types is IHC. IHC is widely utilized to understanding mitochondria expression and function. This allows visualization of mitochondria, but on much lower magnification compared with TEM and 3D EM. IHC

allows for understanding of mitochondria content in specific cell types using colocalization with other antibodies in addition to understanding expression of proteins specific to mitochondria function and dynamics regionally. Both TOM20 and Porin/VDAC are used as a marker of mitochondria content and are quantified using ImageJ and puncta analysis (Zambonin et al., 2011; Honorat et al., 2017; Thai et al., 2019). These proteins can also be used to determine whether other proteins are localized to the mitochondria or the soma in culture (Honorat et al., 2017). Mitochondria IHC is also used to determine function of the ETC by measuring specific OXPHOS subunits. COXI oxidizes NADH and is often used as a marker to determine overall ETC function (Joshi et al., 2015). Using IHC to measure Cytochrome C oxidase activity, or Complex IV (COXIV) can be used a measure of mitochondria activity (Hogan et al., 2009). There have also been studies that assessed mitochondria fusion using IHC in demyelinated optic nerves and saw an increase in Mfn2 expression in a chronic progressive demyelinating mouse model (Thai et al., 2019).

Western blots are also often used to measure specific protein expression of mitochondria content. This technique has its caveats however, due to the fact that the homogenized tissue is typically an assortment of cell types in a region, so the protein expression is not due to a specific cell type. Studies have used Western blots using whole cell lysate, or by further isolating the mitochondria and performing a Western blot on a cleaner sample. One study used spinal cord lysates to measure ETC levels in mouse models of MS and

found an increase in COX I and III levels early in EAE disease (Ng et al., 2019). However, it is important to note that these spinal cord lysates do not just contain neurons and oligodendrocytes, but also astrocytes and immune cells. Assessing COX activity can also be done with isolated mitochondria content instead of the cellular lysates. However, there should not be a difference in results with either method because COX activity is only expressed by mitochondria (Mancini et al., 2018; Singh et al., 2018), but we still do not know which cell types the COX is coming from within the homogenate. All of the complexes have often been measured using western blot using an OXPHOS antibody cocktail, which contains subunits of each complex, COXI through ATP Synthase (Ferro et al., 2017; Djordjevic et al., 2020). This cocktail allows for visualization of COX expression levels individually on one blot to compare between groups. Mitochondria dynamics are often measured with western blot, using Drp1 for measurements of mitochondria fission and Mfn2 for mitochondria fusion. There was an increase in Drp1 expression in the mitochondria rich fraction in a Parkinson's mouse model (Filichia et al., 2016). Drp1 hyperactivation has been evident in both EAE and cuprizone-induced demyelination models (Luo et al., 2017a). An increase in Mfn2 expression in optic nerve lysates was also observed in mice with extra copies of the PLP gene (PLP4e) (Thai et al., 2019). Snph has also been used in Western Blot to understand mitochondria transport in the dysmyelinated *shi* mouse model (Joshi et al., 2015).

The use of dyes and lentiviruses to permeate mitochondria are being routinely used to assess their location and movement. These can be used in both primary cell cultures and brain slices to observe live movement and transport of mitochondria (Errea et al., 2015; Licht-Mayer et al., 2020). Depending on the dye or the lentivirus used, it is possible to study mitochondria function and location on the animal model of MS. One study used a lentivirus to tag mitochondria with in the Purkinje cell layer of the cerebellum (Licht-Mayer et al., 2020). A lentivirus containing mitochondrial-targeted DsRed2 has also been injected into slice cultures (Ohno et al., 2014; Errea et al., 2015) allowing for mitochondria to be visualized after stimulation. This could help understand mitochondria transport and movement after a period of time. To use DsRed2 as a method to understand mitochondria transport, this technique is also used concurrently with kymographs (Kiryu-Seo et al., 2010; Zambonin et al., 2011; Misko et al., 2012).

Another method to quantify mitochondria function is by measuring mitochondrial membrane potential (MMP). Tetramethylrhodamine methyl ester (TMRM) is a cationic, potentiometric dye that measures MMP (Sadeghian et al., 2016). When mitochondria are depolarized, the TMRM dye no longer remains in the mitochondria. Instead of using slice cultures with the DsRed2 lentivirus, this method allows for *in vivo* imaging in mice and understanding depolarization of mitochondria in a live organism. This dye is also used *in vitro* to estimate the MMP (Misko et al., 2012). In addition to this dye, there are also near-infrared mitochondria probes for measuring the MMP (Ren et al., 2016). While live

mitochondrial imaging demonstratae what is occurring in cells in real time, fixed mitochondrial imaging can also be performed. Mitotracker Red has been used to measure MMP in fixed tissues throughout the CNS (Qi et al., 2006). The advantage is that it stains mitochondria in live cells and the dye is well-retained after aldehyde fixation.

One relatively new assay used to measure mitochondria function that is the Agilent Seahorse analyzer. The Agilent Seahorse XF HS Mini Analyzer measures mitochondrial respiration and glycolysis in addition to ATP production rate of live cells in a miniplate format. This analyzer allows for the measurement of oxygen consumption rate, or OCR, by the mitochondria which can be utilized as a measure of mitochondria function. Most of the studies have been in cultured dorsal root ganglion cells, oligodendrocytes, astrocytes, and neurons (Licht-Mayer et al., 2020; Apicco et al., 2021; Demaré et al., 2021). In addition to measuring basal respiration, the sensor cartridge contains ports to inject modulators into the cell wells during the assay for a variety of different tests to understand more aspects of mitochondria function. The Mitochondria Stress test is a specific test can performed by the Seahorse analyzer to determine dysfunction in specific ETC complexes based off of the compounds injected into the assay. This test was used after 6 weeks of 0.3% cuprizone isolated from the cortex to measure changes in maximal respiration (Singhal et al., 2020). This study is one of the first that has been performed in a cuprizone demyelinating cortex model. However, this data does not show a complete response of oligomycin which inhibits ATP Synthase, showing that the amount of

compound they used may not be adequate to get true responses. Djordjevic et al. used this test in a mouse model of Parkinson's (Djordjevic et al., 2020). This test can be applied to mouse models of MS as well to determine what kind of mitochondria dysfunction might occur in these models at specific timepoints. This assay can be utilized using isolated mitochondria after induction of MS to regionally determine mitochondria dynamics at a specific timepoint after disease induction.

Another method to measure mitochondrial function is with an ATP assay to measure ATP output from cells. This has been performed in several cell types including isolated optic nerves (Yin et al., 2016). Another group designed an *in vivo* approach to understanding mitochondria function using an H_2O_2-sensitive GFP (roGFP-Orp1) and a fluorescent ATP sensor (ATeam) that targets mitochondria. These were used to image and measure the dynamics of ATP and H2O2 production in mitochondria of myelinated axons in the PNS (Imamura et al., 2009; van Hameren et al., 2019). While this technique was utilized in the PNS, this method could be adapted to understand mitochondria dynamics in the CNS.

Cell-specific tagging of mitochondria

There is a pressing need to extend mitochondrial studies to tissues, particularly where cell culture-based models are inadequate in recapitulating complex cellular

interactions, such as in MS. Currently, there are several mouse lines available through Jackson Laboratory that allow for studying mitochondria in Cre- specific CNS tissues.

One group developed a set of tools to visualize the dynamics of neuronal mitochondria by using mitochondrially targeted cyan (mitoCFP) and yellow (mitoYFP) fluorescent proteins selectively expressed in neurons under the control of Thy1 or *nse* (*Eno2)* regulatory elements, to make Thy1-mitoCFP and nse-mitoYFP mice (Misgeld et al., 2007). These MitoMouse lines contain high levels of fluorescent proteins consistent with specific labeling of mitochondria in neurons (Mar et al., 2014; Hayes et al., 2019). The group that designed this line was able to perform time-lapse recordings to assess mitochondria transport in peripheral nerves and measure mitochondria transport after axonal injury.

One available strain is MITO-TAG (Jackson #032290). This mouse line was developed from a group at Caltech and contains a hemagglutinin (HA)-tagged EGFP that localizes to the mitochondria outer membrane (Bayraktar et al., 2019). These mice have Rosa26 knocked-in that express the MITO-Tag only in cells that express Cre recombinase as a result of the loxP-STOP-loxP (LSL) cassette. While this line has not been utilized yet in CNS tissues, this strain may allow for neuroscientists to elucidate mitochondria dynamics and function that occur in specific cell types during disease progression and treatment.

A recent development to study mitochondria dynamics *in vivo* is with the use of photo-activatable mitochondria (phAM mice) (Pham et al., 2012). This mouse line has the photo convertible protein Dendra2 targeted to the *Rosa26* locus with an upstream *loxP*-flanked termination signal (Chudakov et al., 2007). The group used a 405nm laser to photoconvert a subpopulation of mitochondria from green to red fluorescence (Pham et al., 2012). This allows mitochondria to be studied in fixed and live tissues. In addition, the photo switchable properties of Dendra2 allow subsets of mitochondria to be precisely monitored within a dense mitochondria network. This line can be crossed with Cre drivers to measure expression in specific cell types, which will allow researchers to determine whether mitochondria are being trafficked locally to meet a specific demand, or whether mitochondria are undergoing fission or fusion (Pham et al., 2012). When the phAM mice were crossed to *Meox2-Cre* mice, allowing for ubiquitous expression, all organs exhibited mito-Dendra2 fluorescence (Pham et al., 2012). Specifically, in the CNS, they saw expression in Purkinje cells. This study also specifically used PCP2-Cre to observe mitochondria expression only in Purkinje cells and in Purkinje cells with mutant Mfn2 (Pham et al., 2012).

To study mitochondria morphology *in vivo*, another group developed a reporter mouse with cell type-specific expression of YFP targeted to the mitochondrial matrix (Sterky et al., 2011). A *lox*-flanked stop cassette was placed upstream of the mito-YFP transgene to restrict expression to cells in which the stop cassette has been removed by *cre*-mediated excision and the construct was integrated by homologous recombination into the

Gt(ROSA)26Sor locus. This allows for ubiquitous expression of mito-YFP with healthy mice and normal function of the respiratory chain (Sterky et al., 2011). These mice also can be crossed to visualize mitochondria expression in Cre- specific CNS tissues.

Additionally, the mito-QC (quality control) mouse line allows for studying mitophagy and mitochondrial architecture in vivo. This transgenic line contains an mCherry-GFP tag fused to the mitochondrial targeting sequence of the outer mitochondrial membrane (OMM) protein, FIS1. This GFP tag has a pH-sensitive fluorescent mitochondrial signature which allows for the assessment of mitophagy and mitochondrial architecture (McWilliams et al., 2016). Under steady-state conditions, the mitochondrial network fluoresces both red and green; however, upon mitophagy, mitochondria are delivered to lysosomes where mCherry fluorescence remains stable, but GFP fluorescence becomes quenched by the acidic microenvironment, resulting in punctate mCherry-only foci (McWilliams et al., 2018); (McWilliams et al., 2019). While mitophagy was only briefly described in this review, changes in mitophagy and how mitochondria are degraded could explain an additional aspect of mitochondria dysfunction in the context of neurobiology and disease.

For the last few decades, mitochondrial studies were initiated in postmortem MS tissue or regions of tissue which lack the full picture of mitochondrial involvement in homeostatic

conditions or neurodegenerations. Recently, progress has been made with improved IHC antibodies, Western Blot, and mitochondrial dyes. In addition, functional studies such as the Seahorse Analyzer allow for assessment of mitochondrial function. Using a variety of techniques discussed paired with genetically engineered mitochondria mouse strains will allow researchers to further understand pathology in MS and hopefully improve the quality of life for patients with MS.

Remyelination and neuroprotection with estrogen beta ligands

Current MS treatments are immunomodulatory and do not increase myelination nor are neuroprotective (Lopez-Diego and Weiner, 2008). Treatment options that confer myelination and neuroprotection are needed due to the fact that MS is a neurodegenerative disease. To test drug efficacy in MS, new treatments are often tested in the experimental autoimmune encephalomyelitis (EAE) mouse model of MS, which incorporates demyelination, inflammation, and neurodegeneration (Lucchinetti et al., 2000; Baxter, 2007; Mangiardi et al., 2011b). Estrogens that act on either estrogen receptor (ER)α or ERβ have been evaluated as a treatment for MS due to their ability to stimulate myelination while also being neuroprotective (Offner et al., 2000; Sicotte et al., 2002; Tiwari-Woodruff et al., 2007; Moore et al., 2014; Karim et al., 2018; Atkinson et al., 2019; Karim et al., 2019). Although ERα ligands have been shown to cause feminization as well as increase risks of breast and uterine cancer, ERβ ligands have been considered more desirable therapeutic candidates (Lindberg et al., 2003). Indazole chloride (IndCl) and its analogues are unique, highly selective ERβ ligands that have

been shown to increase myelination and neuroprotection in both EAE and cuprizone (CPZ) mouse models of MS (Moore et al., 2014; Khalaj et al., 2016; Karim et al., 2018; Karim et al., 2019). These ligands not only improves clinical disease scores and rotarod performance, but also has been shown to improve corpus callosal (CC) axon conduction (Moore et al., 2014; Karim et al., 2019), however its effects on mitochondria remain to be elucidated. These analogues were used in this dissertation to determine whether ERβ ligands improve neuroprotection by modulating mitochondrial dynamics. As a control, we also used resveratrol (3,4'5-trihydroxystilbene; $C_{14}H_{12}O_3$; RSV), which is a polyphenolic phytoalexin found in grapes, berries, peanuts, and wines (Jardim et al., 2018). This compound has been shown to exert antioxidant, anti-inflammatory, anti-apoptotic, and anti-cancer capacities (Jardim et al., 2018). Due to these properties, RSV is known to participate in the "French paradox," which is the inverse correlation of red wine and the incidence of cardiovascular disease (Alarcon De La Lastra and Villegas, 2005; Borra et al., 2005). RSV modulates mitochondrial biogenesis through an indirect way through the induction of the expression of mitochondria-located antioxidant enzymes (Bowers et al., 2000; Jardim et al., 2018). By using both ERβ analogues and RSV, we can determine whether ERβ ligands are able to exert their neuroprotective effects by modulating mitochondria, or if the mitochondria is a result of the remyelination.

Hypothesis

The goal of these studies was to determine mitochondrial dynamics during the course of demyelinating disease and whether ERβ ligand treatment will slow neurodegeneration by alleviating mitochondrial dysfunction. I hypothesize that mitochondrial dysfunction, consisting of altered morphology, increased fission, decreased fusion, and altered ATP production, is an early event in demyelination and contributes to neurodegeneration.

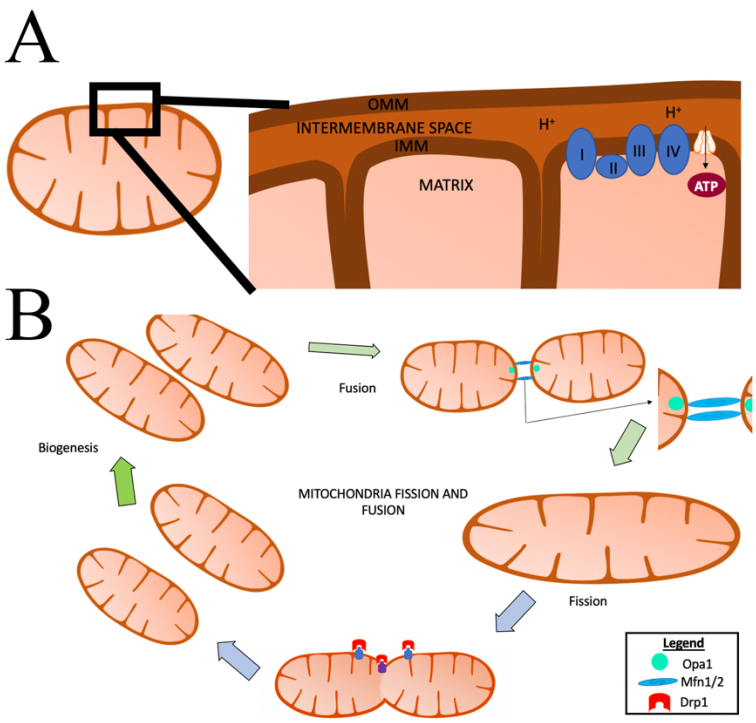

Figure 1. Overview of mitochondria and mitochondrial fission and fusion. (**A**) Mitochondria have an outer mitochondrial membrane (OMM), inner mitochondrial membrane (IMM), and the matrix **(Figure 1A).** The IMM is where the electron transport chain (ETC) is located and where adenosine triphosphate (ATP) production occurs. The ETC pumps protons from the mitochondrial matrix into the intermembrane space. This creates an electrochemical proton gradient across the IMM, providing ATP in addition to helping maintain the mitochondria membrane potential (MMP; $\Delta\Psi_m$). (**B**)Mitochondria are highly dynamic organelles that divide and fuse with fission and fusion, respectively. Mitochondrial fission is defined as the division of one mitochondrion into two daughter mitochondria, while fusion is the union of two mitochondria resulting in one mitochondrion. These two factors allow for this organelle to adapt to cell need at any given time and are regulated by a variety of cellular pathways including proteolytic processing, ubiquitylation, SUMOylation, phosphorylation and dephosphorylation. When fusion or fission occur, the proteins are catalyzed by guanosine triphosphate (GTP)ase enzymes. In mammals, mitochondrial fission is mediated and controlled by dynamin-related protein 1 (Drp1) and dynamin 2 (Dnm2). Fusion has two GTPases: mitofusins 1 and 2 (Mfn1, Mfn2) which control the OMM, while the IMM is controlled by optic atropy 1 (OPA1) in mammals. Created with Motifolio Biology Bundle.

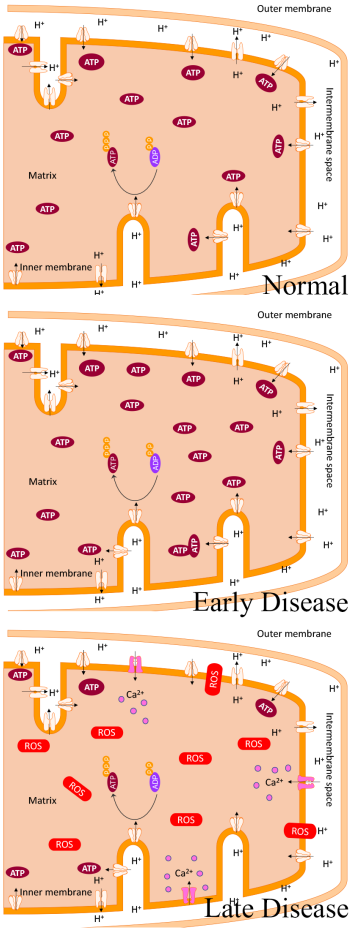

Figure 2. Mitochondrial changes in early MS and progressive MS. In homeostatic conditions, mitochondria produce ATP through ATP Synthase and with the help of the proton motive force of the electron transport chain. ATP is produced due to the negative potential in the mitochondrial matrix, when protons are pumped from the matrix into the intermembrane space. Early in demyelinating disease, the loss of myelination causes a decrease of saltatory conduction in the neuronal axon contributing to an increase in energetic demand. This causes an increase in ATP production in order to meet the new demands of the cell. However, the energetic demands will not be able to be met long term by the mitochondria. This, paired with an increase in reactive oxygen species (ROS), will cause ATP depletion. The Na^{+}/Ca^{2+} exchanger will reverse in an attempt to restore the polarization, but this calcium influx will continue to be detrimental to the mitochondria and to the cells, and cause cell death. Created with Motifolio Biology Bundle.

Chronic active MS lesions	Progressive MS	Pattern III MS lesions	Inactive lesions
• Increased porin in chronic active MS lesions compared with myelinated axons (Zambonin et al., 2011) • No difference in axonal mitochondria content between RM and DM axons in RM regions close to DM areas in chronic MS lesions (Zambonin et al., 2011) • Reduction in mitochondria content in shadow plaques compared with chronically DM axons in MS lesions (Zambonin et al., 2011) • Decreased COXIV in axons in the rim of chronic active lesions (Mahad et al., 2009) • Increased COXIV in MS lesions compared to control white matter and NAWM (Witte et al., 2009) • Increased in mtHSP70 compared to control white matter and NAWM (Witte et al., 2009)	• Respiratory deficient neurons (lacked COXIV but contained COXII) in DRG (Licht-Mayer et al., 2020) • Respiratory deficient neurons also had increased mitochondria content, size, and number (Licht-Mayer et al., 2020) • SPMS: individual neurons demonstrated decreased COXIV and mtDNA deletions throughout the gray matter (Campbell et al., 2011) • SPMS: Decreased nuclear-encoded mitochondria ETC genes (COXI, COXIII, COXIV, COXV) (Dutta et al., 2006) • PPMS/SPMS: Normal appearing gray matter showed reduced PGC-1α accompanied with neuronal loss in the cingulate gyrus (Witte et al., 2013).	• Decreased COXIV in axons, astrocytes, and oligodendrocytes (Mahad et al., 2008)	• Axons in inactive lesions had increased COXIV (Mahad et al., 2009)

Table 1. Mitochondrial changes in human MS postmortem tissue summary. Mitochondrial changes are observed in different subtypes of MS, including chronic active MS lesions, progressive MS, pattern III MS lesions, and inactive lesions. However, all of these types of lesions in MS have observed changes with COXIV.

	Experimental Autoimmune Encephalomyelitis	Cuprizone diet; 0.2% unless stated otherwise	Genetic models
• Morphology	• EAE D10: vacuolization and dissolution of mitochondrial cristae (Qi et al., 2006) • EAE D16: fragmented and swollen mitochondria (Holman et al., 2020)	• 3 weeks: Megamitochondria in oligodendrocytes (Acs and Komoly, 2012) • 5 weeks: Mitochondria swelling (Faizi et al., 2016) • 6 weeks: Increased mitochondria size correlates with increased g-ratio (Luo et al., 2017)	• PLP1-overexpressing model shows increased mitochondrial density (Hogan et al., 2009) • Increased mitochondrial density in *Shi* model (Joshi et al., 2015) • Snph knockout mice had shorter and thicker mitochondria compared to controls (Ohno et al., 2014)
• Fission and fusion	• Increased Drp1 in lesioned spinal cord at peak EAE disease (Luo et al., 2017) • Drp1 peptide inhibitor was neuroprotective (Luo et al., 2017)	• 6 weeks: Increased Drp1 in the corpus callosum (Luo et al., 2017), inhibiting Drp1 was neuroprotective	• SLC25A46 knockout (OMM protein) demonstrated degenerating dendrites, enlarged mitochondria in Purkinje cells, decreased ATP production (Li et al., 2017) • PLP4e mice have increased Mfn2 (Thai et al., 2019) • Opa1,PLP mutants have increased mitochondrial size with genetically induced mitochondria function (Ineichen et al., 2020)
• Transport	• Syntaphilin deletion does not benefit clinical symptoms in EAE (Joshi et al., 2015)	• 6 weeks 0.3% cuprizone with rapamycin (10mg/kg): Syntaphilin immobilization facilitates the survival of demyelinated axons (Ohno et al., 2014) • Demyelinated axons deficient in syntaphilin degenerated at a greater rate than wildtype axons (Ohno et al., 2014)	• Snph knockout mice facilitated axon regenerative capacity (Zhou et al., 2016) • Deletion of Snph in dysmyelinating *Shi* mice prolonged survival and reduced cerebellar degeneration (Joshi et al., 2015)
• Mitochondrial polarization	• Depolarized mitochondria in a RRMS EAE model (Sadeghian et al., 2016)	• 5 weeks: Depolarized MMP, Mitochondria swelling, Cytochrome c release (Faizi et al., 2016)	• No studies found
• Mitochondrial function (Seahorse)	• No studies found	• 6 weeks 0.3% cuprizone: Decrease in maximal respiration (Singhal et al., 2020)	• No studies found
• Mitochondria transcription factors	• No studies found	• 12 weeks: Decreased PGC-1α, NRM-1, TFAM, and increased Drp-1 mRNA levels (Shiri et al., 2020)	• No studies found

Table 2. Summary of altered mitochondrial dynamics in animal models or genetic models of demyelination. While there is extensive research on mitochondrial fission, fusion and transport in genetic knockout models, there is not many studies on mitochondrial dynamics with experimental autoimmune encephalomyelitis or cuprizone.

In Vitro	*Ex Vivo*	*In Vivo*
• Transmission electron microscopy: mitochondria density, morphology, shape, and cristae complexity (Qi et al., 2006) • Mitochondria membrane potential TMRM: Mitochondria function (Misko et al., 2012; Benardais et al., 2013; Ren et al., 2016) • Seahorse Analyzer: Mitochondria function (Licht-Mayer et al., 2020) • Kymographs: Mitochondria transport (Kiryu-Seo et al., 2010; Zambonin et al., 2011; Misko et al., 2012) • ATP probe: measures ATP and H_2O_2 production (Imamura et al., 2009)	• Transmission electron microscopy: mitochondria density, morphology, shape, and cristae complexity (Errea et al., 2015) • Three-dimensional electron microscopy: mitochondria morphology, size (Ohno et al., 2014) • Mitochondria photoconversion lentivirus: Mitochondria trafficking and movement (Licht-Mayer et al., 2020) • DsRed2 Lentivirus: Mitochondria visualization and movement (Ohno et al., 2014; Errea et al., 2015) • Kymographs: Mitochondria transport (Ohno et al., 2014; Yin et al., 2016)	• Transmission electron microscopy: mitochondria density, morphology, shape, and cristae complexity (Hogan et al., 2009; Nikic et al., 2011; Zambonin et al., 2011; Joshi et al., 2015; Ineichen et al., 2020) • 3D electron microscopy: mitochondria morphology, size ((Ohno et al., 2014; Yin et al., 2016) • Immunohistochemistry: Regional visualization of mitochondria (Hogan et al., 2009; Zambonin et al., 2011; Joshi et al., 2015; Honorat et al., 2017; Thai et al., 2019) • Western Blot: Mitochondria protein expression (Joshi et al., 2015; Ferro et al., 2017; Filichia et al., 2017; Luo et al., 2017; Mancini et al., 2018; Singh et al., 2018; Ng et al., 2019; Thai et al., 2019; Djordjevic et al., 2020) • DsRed2 Lentivirus: Mitochondria visualization and movement (Ohno et al., 2014; Errea et al., 2015) • Mitochondria membrane potential: Mitochondria function (Sadeghian et al., 2016) • Mitochondria membrane potential Mitotracker Red: Mitochondria function (Qi et al., 2006) • ATP Assay (Yin et al., 2016) • ATP probe: measures ATP and H_2O_2 production (Imamura et al., 2009; van Hameren et al., 2019) • Seahorse Analyzer: Mitochondria function (Djordjevic et al., 2020; Singhal et al., 2020)

Table 3. Techniques used to study mitochondria. Most studies that are used to study mitochondrial dynamics are assessed *in vitro* because it is less difficult and also easier to draw conclusions by studying mitochondria in one cell type. The studies that have been performed *in vivo* and *ex vivo* are geared towards specific areas of the brain that are largely affected, like the spinal cord, while also using genetic knockout models to determine drastic effects of mitochondrial dynamics with the loss of a major protein in a specific cell.

Chapter 2: General Methodology

A version of this chapter is published in Journal of Neurobiology of Disease.

Atkinson, K.C. *et al.* Diffusion tensor imaging identifies aspects of therapeutic estrogen receptor B ligand-induced remyelination in a mouse model of multiple sclerosis. *Neurobiology of Disease.* **130**, 104501 (2019).

Animals

All procedures followed the protocols established by the American Veterinary Medical Association in accordance with the National Institutes of Health (NIH) and were approved by the Institutional Animal Care and Use Committee (IACUC) at UCLA, Los Angeles and UCR, Riverside. Eight- to twelve- week-old C57BL/6J, Thy1-YFP (JAX #003709, Bar Harbor ME), and PLP-eGFP male and female mice were obtained from Jackson Laboratories and maintained in-house at the animal facility. PLP-eGFP mice were a kind gift provided by Dr. Wendy Macklin (University of Colorado, Denver CO, USA). The generation, characterization, and genotyping of these mice has previously been reported (Mallon et al., 2002). Mice were all kept on a 12 hr light/dark cycle with unrestricted access to food and water.

Experimental Autoimmune Encephalomyelitis

EAE was induced as previously described (Mangiardi et al., 2011a; Hasselmann et al., 2017b). In brief, one-part lyophilized myelin oligodendrocyte protein peptide 35-55 (MOG_{35-55}) (Mimotopes, San Diego, CA) was dissolved in Dulbecco's phosphate buffered saline without calcium or magnesium (DPBS) and 1.3 parts heat killed *Mycobacterium tuberculosis* H37 Ra (Beckton Dickinson, Franklin Lakes NJ) in complete Freund's adjuvant (CFA; Becton Dickinson, Franklin Lakes NJ) were emulsified, resulting in a final concentration for both MOG_{35-55} peptide and *M. tuberculosis* of 2 mg/mL. The EAE induction protocol involved initial MOG+CFA immunization and PTX injection on day 0,

second PTX injection on day 2, and second MOG+CFA immunization on day 7. On the first day of induction (Day 0), 0.05 mL of the emulsion was injected subcutaneously into the backs of the animals between the cervical vertebrae and left shoulder and another 0.05 mL between the lumbar vertebrae and left thigh. Injections were placed as such to maximize proximity to axillary and inguinal lymph nodes. Each mouse was then injected intraperitoneally (IP) with 0.3 mL of Pertussis toxin (PTx; List Biological Laboratories, Campbell CA) in DPBS at 1.667 µg/mL, returned to its home cage with free access to water and food and monitored until recovered. Two days after induction (day 2), the mice were given booster IP injections of PTx at the same concentration. Five days later (day 7), motor function was assessed using clinical scores, then mice were injected with a freshly made MOG_{35-55} /*M. tuberculosis* emulsion at the same ratios and concentrations used on Day 0. Day 7 MOG_{35-55} injections at 0.05 mL each were placed between the cervical vertebrae and right shoulder, and the lumbar vertebrae and right thigh. Starting 7 days post induction (dpi), mice were scored daily for clinical disease severity. The clinical scoring protocol was defined as: 0, unaffected; 1, complete tail limpness; 2 failure to right upon attempt to roll over; 3, partial hind limb paralysis; 4, complete hind limb paralysis; and 5, moribund (Hasselmann et al., 2017a). Mice reaching clinical scores of 4.5 or higher were euthanized humanely with isoflurane anesthesia followed by cervical dislocation.

Cuprizone Diet

For Chapter 4, mice were assigned to two groups: normal diet (normals) and 0.2% CPZ diet for either 3, 6, 9, or 12 weeks as previously described (Crawford et al., 2009; Moore et al., 2014; Lapato et al., 2017; Atkinson et al., 2019). For Chapter 6, mice were assigned to two groups: normal diet (control; n=13) and 0.2% CPZ diet for nine weeks (9wkDM; n=41) as previously described. Twenty-seven of the 9wkDM mice were then switched to two weeks of a normal diet and injected subcutaneously (s.c.) with either vehicle (RM+Veh; n=13) or IndCl (RM+IndCl; n=14). Unless otherwise noted, all animals were included in all methods and subsequent analysis.

Treatment

At peak EAE disease, a subgroup of mice were treated and injected subcutaneously (s.c.) with either vehicle, IndCl, IndCl-*o*-Methyl, or IndCl-*o*-Chloro. IndCl and all IndCl analogues (synthesized in the J.A.K. laboratories) were dissolved in 10% ethanol + 90% (vol/vol) Miglyol 912N (vehicle; Sasol) and administered at 5mg/kg body weight in a volume of 0.1mL/injection (De Angelis et al., 2005). Vehicle/control groups received s.c. vehicle injections. Resveratrol was also used in some experiments as a positive control for mitochondria. Resveratrol was dissolved in DPBS and administered to mice intraperitoneally (i.p.) at 50mg/kg with DPBS used as vehicle.

Rotarod Behavioral Test

Motor behavior was tested up at each timepoint for each mouse using a rotarod apparatus (Med Associates, Inc., St. Albans, VT). Briefly, animals were placed on a rotating horizontal cylinder for a maximum of 200 seconds. The amount of time the mouse remained walking on the cylinder without falling was recorded. Each mouse was tested on an either an accelerating speed of 4-40 rotations per minute (rpm) or a fixed speed of 16 rpm and were given three trials for any given day. The three trials were averaged to report a single value for an individual mouse, and averages were then calculated for all animals. The first two trial days served as practice trials.

Walking Gait Test Behavioral Test

The walking gait test protocol was adapted from Carter et al., 1999 (Carter et al., 1999). The walking gait test was used to compare the gate of EAE and normal mice. To obtain footprints, the hind and front feet of the mice were coated with blue and red nontoxic paints, respectively. The animals were then allowed to walk along a 50-cm-long, 10-cm-wide runway (with 30-cm-high walls) in a plexiglass box. All mice had three training runs and were then given one run per week. A fresh sheet of white paper was placed on the floor of the runway for each run. The footprints were analyzed for four step parameters (all measured in centimeters). (1) Stride length was measured as the average distance of forward movement between each stride. (2) Hind-base width and (3) front-base width were measured as the average distance between left and right hind footprints and left and right

front footprints, respectively. These values were determined by measuring the perpendicular distance of a given step to a line connecting its opposite preceding and proceeding steps. (4) Distance from left or right front footprint/hind footprint overlap was used to measure uniformity of step alternation. When the center of the hind footprint fell on top of the center of the preceding front footprint, a value of zero was recorded. When the footprints did not overlap, the distance between the center of the footprints was recorded. For each step parameter, three values were measured from each run, excluding footprints made at the beginning and end of the run where the animal was initiating and finishing movement, respectively. The mean value of each set of three values was used in subsequent analysis.

In vivo Diffusion Tensor Imaging (DTI)

MRI Acquisition

Mice were anesthetized with 4% isoflurane in oxygen flowing at 0.6L/min (control: n=7; 9wkDM: n=7; RM+Veh: n=5, RM+IndCl: n=6). Individual mice were transferred to a purpose-built cradle and secured using three-point immobilization of the head with two ear bars and a tooth bar. The mouse cradle was placed in the center of a 7 Tesla (T) spectrometer (Oxford Instr, Carteret, NJ, USA) driven by a Bruker console running Paravision 5.1 (Billerica, MA USA). Respiration was monitored remotely, and the temperature was homeothermically controlled by forced air (SA11 Instr, Inc., USA). The S116 Bruker gradients (400 mT/m) were used in combination with a birdcage

transmit and an actively decoupled, receive-only, single-channel surface coil to acquire the data. Following a multi-slice, gradient-echo pilot scan to optimize positioning within the magnet, localized shimming was performed on the head to improve B0 homogenicity. A standard, 4-shot, spin echo, echo planar imaging sequence (38,000/23.3 ms repetition and echo time, respectively) was used to acquire diffusion-weighted images with directionally-encoded gradients applied along thirty different, even-spaced directions and with a b value of 1000 s/mm^2, using Δ = 10 ms and δ = 4 ms and one additional image volume with a b value of 0 s/mm^2. All images were acquired with a 128-read and 128-phase-encoding-matrix (X,Y direction respectively) within a 20mm^2 field-of-view and 20x14 1 mm contiguous, coronal slices, resulting in an in-plan resolution of 156x156 μm and a 1000 μm slice thickness. The number of averages (NEX) was 1.

In vivo DTI Data Analysis

Data were fitted for parametric images of fractional anisotropy (FA), radial diffusivity (RD), and axial diffusivity (AD) using FSL tools, (University of Oxford, UK). Spatial co-registration of the FA data to a single common mouse brain was accomplished using affine transformations and then applied to the other diffusivity indices.

Ex vivo DTI Imaging

For *ex vivo* imaging, mice were deeply anesthetized by isoflurane (Piramal Healthcare) inhalation and perfused transcardially with 1XPBS followed by 10% formalin (Thermo Fisher Scientific) with 10mM Prohance (a Gadolinium, Gd agent) (control: n=6; 9wkDM: n=8; RM+Veh: n=8; RM+IndCl: n=8). While Gd is typically used to enhance T1 imaging, here, it was used to increase brain structural contrast using T2 weighted imaging. The perfused brains were preserved in PBS until they underwent DTI. High-resolution DTI imaging was acquired *ex vivo* using a 9.4 T Bruker Advance Imager with gradient amplitude of 720 mT/m (Experimental Imaging Centre, University of Calgary, Calgary, Canada; Paravision 5.1; Bruker Biospin, Billerica, MA). This higher field strength compared the 7T used for *in vivo* maging allows for improved SNR. The data were collected using 128 x 128 matrix zero-filled to a final reconstruction of 256 x 256 matrix, with 15 mm x 15 mm field of view with 30 x 0.5 mm slices, 30 gradient directions, and 2 b-values (b = 0 and b = 3000 s/mm^2) with 5 b_0 images. Reptition time (TR)/echo time (TE) was 8000 ms/35.66 ms and number of averages (NEX) was 4. The larger b-value was used in the current experiments as it provides enhanced contrast particularly when using increased number of sampling directions.

Ex vivo DTI Data Analysis

All data were fitted for parametric images of FA, RD, and AD using FSL tools, (University of Oxford, UK). Spatial co-registration of the FA data to a single common

mouse brain was accomplished using affine transformations and then applied to the other diffusivity indices. Tract-based spatial statistical analysis was conducted as before (Harris et al., 2016) with the exception that analysis was constrained to the CC, an area that has been shown to be significantly affected in this model (Matsushima and Morell, 2001; Crawford et al., 2009). All four experimental groups were entered into the general linear model for statistical interference of any effect between all groups, followed by posthoc testing with multiple contracts for difference to control at the cluster-corrected level of $p < 0.05$ and $z = 1.7$ with a variance smoothing of 0.5 mm. A region-of-interest approach was also used by placing regions within the genu of the CC and the adjacent cingulum area. Regions were interrogated for mean diffusivity values. Images at the antero-posterior level from Bregma of 0.14/0.26mm (anterior) and -2.82/3.08mm (posterior) were utilized for tissue-level region analysis, chosen based on TBSS data. In addition, the regional analysis was performed using DTI-parametric maps generated in the DSI studio in native space (http://dsi-studio.labsolver.org). CC regions of interest (ROIs) were manually segmented by blinded experimenters.

Histological Preparation of Tissues

Mice were deeply anesthetized with isoflurane and intracardially perfused with ice cold phosphate buffered saline (PBS) then 10% formalin in PBS (Fisher Scientific, Waltham MA). The cerebellum was dissected and post-fixed in 10% formalin for immunohistochemistry (IHC). After 2 hours, the brain was transferred to 30% sucrose with

0.2% sodium azide for 2 days (Fisher Scientific, Waltham MA) for cryoprotection. Tissue was embedded in a gelatin/sucrose solution (7.5% w/v gelatin (Becton Dickinson, Franklin Lakes NJ) +15% w/v sucrose (Fisher Scientific, Waltham MA) in Milli-Q water). Gelatin tissue blocks were placed in 10% formalin for 2 hours, followed by 30% sucrose+0.2% sodium azide solution until ready for sectioning. Embedded cerebellar gelatin blocks were cut to 10µm thick sagittal sections using a cryostat and affixed directly to warm slides. Brain gelatin blocks were flash frozen on dry ice, and cut to 40µm thick coronal sections, then placed in PBS with 0.2% sodium azide.

Immunohistochemistry

Prior to antibody application, tissue sections were thoroughly washed with PBS to remove residual sodium azide, permeabilized with 0.3% Triton-X (Electron Microscopy Sciences, Hatfield PA) and blocked in 15% normal goat serum (NGS) (Sigma-Aldrich, St. Louis MO). Sections were incubated in 1:500 dilutions of primary antibodies (**Table 5**) for 2 hours at room temperature followed by overnight at 4^{o}C. The following day, the sections were washed with PBS and then tris buffered saline (TBS). The sections were incubated with the corresponding secondary antibodies in TBS: Goat anti-chicken Cy5 (Invitrogen, Carlsbad, CA), Goat anti-rabbit IgG Cy5 (Invitrogen Carlsbad, CA), Goat anti-rabbit IgG Cy3 (EMD Millipore, Burlington MA), Goat anti-Rat IgG Cy3 (Invitrogen, Carlsbad CA), Goat anti-mouse Cy5 IgG (Invitrogen Carlsbad, CA), Goat anti-mouse Cy3 IgG (Invitrogen Carlsbad, CA). Sections were co-stained with 4',6-Diamidino-2-

Phenylindole (DAPI; EMD Millipore, Burlington MA). Lastly, the sections were washed again with TBS, mounted, and cover-slipped.

Cerebellar mitochondria isolation

Mitochondria isolation was adapted from (Djordjevic et al., 2020). All procedures were performed on ice. Mice were euthanized by isoflurane overdose, decapitated and the cerebellum quickly excised onto a cold petri dish. Whole tissue homogenates of cerebellar tissue was prepared in a glass homogenizer containing 1mL of mitochondrial isolation buffer (70mM sucrose, 210mM mannitol, 5mM HEPES, 1mM EGTA, 0.5% fatty acid free BSA). The tissue was homogenized with ten strokes each from pestle A, then pestle B, and the resultant homogenate was centrifuged at 800 x g for 10 minutes at 4^{o}C. The resulting supernatants were collected and centrifuged at 8000 x g for 15 min at 4^{o}C. The new supernatants were discarded, and the pellets were saved. The pellets were washed in mitochondria isolation buffer and centrifuged at 8000 x g for 15 min one more time at 4^{o}C. The final supernatant was discarded, and the final pellet (isolated mitochondria fraction) was resuspended in 150µL of mitochondrial isolation buffer. A small volume of the suspension was collected for use in a Bradford to determine the concentration of total protein, and then protease and phosphatase inhibitors were added to the isolated mitochondria for the western blot. Protein concentrations of the samples were measured using the Bradford assay with a light absorbance at 595 nm in a microplate reader.

Western Blot

Samples were boiled for 10 min at 55ºC and subjected to electrophoresis on a 10% sodium dodecyl sulfate-polyacrylamide gel (SDS-PAGE). A Trans-blot Turbo Transfer System (Bio-Rad) was used to transfer proteins to PDVF membrane. Following transfer, total protein was detected by the ChemiDoc™ MP Imager. Membranes were blocked for 1 h at room temperature in TBS with 0.1% Tween-20 (TBST) containing 5% milk. Thereafter, membranes were incubated overnight, with selected primary antibodies in TBST with 5% milk at 4◦C. The following day, the membranes were washed in TBST (three ten-minute washes) and incubated with selected secondary antibody, also prepared in 5% milk in TBST, for 2 hours at 4ºC. Antibody binding was detected with enhanced chemiluminescence (ECL) solution (Bio-Rad Clarity™ Western ECL Substrate Kit) and the membrane was imaged using a Bio-Rad UV transilluminator (ChemiDoc™ MP Imaging System). PageRuler™ Plus Protein Ladder was used to determine the molecular weights of the protein bands. The following primary antibodies were used: Total OXPHOS Rodent WB Antibody Cocktail (ab110413, Abcam), VDAC1/Porin (ab14734, Abcam), Anti-Drp1 antibody (OTI4F6) (ab156951, Abcam), Anti-Mitofusin 2 antibody (ab56889, Abcam), and syntaphilin (sc-33824, Santa Cruz). The secondary antibodies Goat anti-mouse IgG_{2a} horseradish peroxidase (HRP) (ThermoFisher Scientific), goat anti-mouse IgG_{2b} HRP (ThermoFisher Scientific), goat anti-mouse IgG (H+L) HRP (Millipore Sigma), and anti-rabbit IgG HRP (Cell Signaling Technology) were used. The antibodies and concentrations are displayed in Table 6.

Seahorse XFp Analyzer Mito Stress Test

Complex-I-dependent mitochondrial respiration was assessed by measuring oxygen consumption rate (OCR) in real time, in freshly isolated mitochondria from the cerebellum, using the Seahorse XFp Analyzer (Agilent Technologies, CA). Two micrograms of freshly isolated mitochondrial protein were diluted in mitochondrial assay solution (MAS, volume of 25 µL) containing 70 mM sucrose, 220 mM mannitol, 10 mM KH_2PO_4, 5 mM $MgCl_2$, 5 mM HEPES, 1 mM EGTA, and 0.2% BSA (pH 7.2), and plated in each well of the plate. The plate was then centrifuged for 20 min at 2000 g, at 4 ◦C. After centrifugation, 155 µL of MAS with pyruvate (10 mM) and malate (2 mM) was added to each well, and the plate was incubated at 37 ◦C for 8–10 min. Basal level of oxygen consumption was measured in the presence of Complex I substrates, pyruvate and malate. Adenosine diphosphate (ADP, 2 mM), oligomycin (1.5 µM), carbonylcyanide p-trifluoromethoxyphenylhydrazone (FCCP, 4 µM) and rotenone (1 µM) + antimycin A (1 µM) were injected consecutively through ports A, B, C and D in the Seahorse Flux Pak cartridges, to determine coupled respiration, uncoupled respiration, and non-mitochondrial oxygen consumption [35]. Coupled respiration that drives oxidative phosphorylation of ADP to ATP was measured after the addition of ADP. Oligomycin was then added to terminate coupled respiration through inhibition of ATP synthase. The protonophore FCCP was added to stimulate uncoupling of the respiratory chain and allow for the measurement of uncoupled respiration. Finally, injection of rotenone (Complex I inhibitor) and antimycin (Complex III inhibitor) blocked the flux of electrons through these complexes so that no oxygen was further consumed at cytochrome c oxidase (non-mitochondrial

respiration rates). OCR data were calculated with subtraction of non-mitochondrial respiration rates.

Quantification and Microscopy

Sections were imaged at similar light exposures using an Olympus BX61 spinning disc confocal microscope equipped with 10x and 40x Super Apochromat objectives (Olympus America Inc., Cypress CA) connected to a camera (Hamamatsu Photonics Orca-R^2, Hamamatsu Japan). Z-stack images were acquired, and projection images compiled using Slidebook 6 software (Intelligent Imaging Innovations Inc, Denver CO). Immunofluorescence intensity and cell numbers was assessed with NIH ImageJ software (v1.50i http://rsb.info.nih.gov/ij/) and quantified for MBP, Iba-1, COXIV, and TSPO immunofluorescence, or cell counts for PLP-EGFP$^+$ cells. Histograms were adjusted evenly to match those of control images and saved. Files were then converted to RGB tagged image format (.tif) files and transferred to ImageJ where individual color channels were converted to gray scale. Brightness and contrast were automatically adjusted to limit experimenter bias and a region of interest was traced around an area encompassing the retina, optic nerve, optic tract, LGN, or visual cortex. The threshold of staining for each image and thus the percentage of fluorescent pixels in each area of interest was computed by the software and reported in a table, which was transferred to Prism® (Graphpad, La Jolla CA) for statistical analysis. Results from all counts were analyzed in GraphPad Prism as well. Puncta analysis in the COXIV images was adapted from (Horzum et al., 2014).

The background was subtracted, and the CLAHE and Laplacian of Gaussian Plugins were used.

Electron Microscopy

Cerebellums dissected from paraformaldehyde perfused mice were post-fixed in 2% glutaraldehyde (Electron Microscopy Sciences, Hatfield PA) and 5% formalin (Fisher Scientific, Waltham MA). Cerebellums were Epon embedded and stained with uranyl acetate-lead citrate. Number of myelinated and unmyelinated axons and the g- ratio (the ratio of the axon diameter to the total myelinated fiber diameter), was quantified as in previous studies (Crawford et al., 2009). For each axon, two measurements for axon diameter were made.

Statistical Analysis

For IHC, two sections per mouse were taken for the cerebellum. There were 4-10 mice per treatment group. Statistics were performed using Prism® (GraphPad, La Jolla) program for Windows. Graph values are expressed as mean $\pm$ standard error of the mean. For histology, and *in vivo* studies statistical analysis of mean values was carried out using one-way ANOVA if mean values passed a normality test, or Kruskal Wallis multiple comparison test if they did not. For EAE clinical scores, statistics were performed using an ordinary two-way ANOVA with Bonferroni post-hoc test as previously described

(Hasselmann et al., 2017a). For chapter 6, DTI and immunohistochemistry data were analyzed by 2-tailed unpaired t-tests with Welch's correction comparing Control vs. 9wkDM and RM+Veh vs. RM+IndCl. Differences were considered significant at the *$p<0.05$, **$p<0.01$, ***$p<0.001$, and ****$p<0.0001$ level.

Table 4. Immunohistochemistry Primary Antibodies Utilized with Manufacturer Information and Concentration Used.

Antibody	Manufacturer	Catalogue #	RRID	Dilution
Myelin Basic Protein	EMD Millipore	AB9348	AB_2140366	1:500
SMI-32	EMD Millipore	NE1023	AB_10682557	1:500
Myelin Oligodendrocyte Glycoprotein	EMD Millipore	MAB5680	AB_1587278	1:500
Olig2	Thermofisher Scientific	P21954	AB_2539836	1:500
Iba1	Waco	019-19741	AB_839504	1:500
NF-200	Sigma-Aldrich	N4142	AB_477272	1:500
NF-M	EMD Millipore	MAB1621	AB_2074321	1:500
Translocator Protein (TSPO)	Abcam	ab37884	AB_777118	1:500
VDAC/Porin	Abcam	ab14734	AB_443084	1:500
Adenomatous Polyposis Coli (CC1)	Genetex	GTX16794	AB_422404	1:50
Glial Fibrillary Acidic Protein (GFAP)	EMD Millipore	AB5541	AB_177521	1:500
Calbindin	Sigma-Aldrich	C2724	AB_258818	1:500
COXIV	Novus	NB110-39115	AB_2085715	1:500
CD45	BD Pharmingen	550539	AB_2174426	1:500
Syntaphilin	Santa Cruz	sc-33824	AB_2193559	1:500

Table 4. Antibodies used for immunohistochemistry.

Table 5. Western Blot Primary and Detection Antibodies Utilized with Manufacturer Information and Concentration Used.

Antibody	Manufacturer	Catalogue #	RRID	Dilution
VDAC1/Porin	Abcam	ab14734	AB_443084	1:2000
Total OXPHOS Rodent WB Antibody Cocktail	Abcam	ab110413	AB_2629281	1:250
Anti-Drp1 [OTI4F6]	Abcam	ab156951	AB_2868469	1:2000
Anti-Mitofusin 2	Abcam	ab56889	AB_2142629	1:2000
Syntaphilin (H-250)	Santa Cruz	sc-33824	AB_2193559	1:200
Goat anti-mouse IgG_{2a}, horseradish peroxidase	ThermoFisher Scientific	M32207	AB_1500830	1:2000
Goat anti-mouse IgG_{2b}, horseradish peroxidase	ThermoFisher Scientific	M32407	AB_2536647	1:2000
Goat anti-mouse IgG (H+L), horseradish peroxidase	Millipore Sigma	AP308P	AB_92635	1:2000
Anti-rabbit IgG, HRP-linked antibody	Cell Signaling Technology	7074P2	AB_2099233	1:2000

Table 5. Antibodies used for Western Blot. All antibodies and dilutions used for Western Blots. Protocol was adapted from (Djordjevic et al., 2020) and all antibodies were diluted with 5% milk in tris-buffered saline with Tween 20 (TBST).

Chapter 3: Mitochondrial dynamics are altered longitudinally in experimental autoimmune encephalomyelitis

Abstract

Postmortem studies of multiple sclerosis (MS) patients demonstrate decreased mitochondrial activity in addition to inflammation throughout the central nervous system. Gait abnormalities in MS patients have been linked to Purkinje cell (PC) demyelination, blebbing axons, and atrophy of dendrites in the cerebellum. Similar cerebellar changes are also observed in experimental autoimmune encephalomyelitis (EAE). In addition, axonal degeneration is linked to loss of metabolic support and demyelination. We hypothesize that mitochondrial dysfunction causes axonal degeneration in the context of inflammatory degeneration. To test this hypothesis, cerebellar pathology was investigated longitudinally in EAE disease course from peak disease (day 21) to late disease (day 60). Behavior (walking gait test and rotarod), pathology (immunohistochemistry and Western blot), and mitochondrial function (Seahorse XFp Mito Stress Test) were assessed. From peak disease to late disease, the average EAE clinical score was 2.5. Behavioral tests showed that EAE mice had decreased time on the rotarod and decreased stride length compared to normal. Similarly, increased inflammation and decreased myelination were observed at all timepoints. Mitochondria electron transport chain levels showed no change at peak disease, but chronic EAE showed decreased COXIV, ATP Synthase, mitochondria fusion (Mfn2), and increased mitochondrial fission (Drp1). Mitochondria dysfunction was evident with decreased basal respiration beginning at peak disease and lasting through chronic disease. These data demonstrate that mitochondria dysfunction is evident by peak disease following irreversible axon damage. Future studies will determine whether early treatment with an estrogen receptor β ligand before axon

damage occurs can alleviate mitochondria dysfunction and slow neurodegeneration in EAE.

Introduction

The goal of this study was to determine when mitochondrial dynamics are altered in the EAE model of MS. This MOG_{35-55} peptide model of MS recapitulates inflammation, demyelination, and neurodegeneration (Craner et al., 2003; MacKenzie-Graham et al., 2009; Shields et al., 2012; Shields et al., 2015; Hasselmann et al., 2017a; Hasselmann et al., 2017c; Kipp et al., 2017). We hypothesize that mitochondrial dynamics are altered early in experimental autoimmune encephalomyelitis and contributes to further neurodegeneration. To address our hypothesis, female mice were induced with EAE and mitochondria function and pathology were measured at peak EAE (EAE D21) and chronic EAE (EAE D40 and EAE D60) to determine when mitochondrial dynamics are changing longitudinally in disease. Mitochondria morphology, pathology, and function were measured using electron microscopy (EM), Western blot, and the Seahorse XFp Analyzer. Understanding the pathophysiology of MS symptoms will allow us to improve treatments and the quality of life of patients with MS.

Results

Demyelination, axon blebbing, and mitochondria dysfunction has been demonstrated in postmortem tissue from MS patients (Dutta et al., 2006; Mahad et al., 2009; Witte et al., 2009; Campbell et al., 2011; Zambonin et al., 2011). To determine Purkinje cell counts are altered in the cerebellum, IHC was performed on MS and control postmortem cerebellar tissue (**Figure 3A**). Representative chromogen IHC for Calbindin, expressed in Purkinje cells, is shown in (**Figure 3B**). There was a significant decrease in Calbindin+ cells in the MS postmortem tissue compared to the control postmortem tissue.

To show a similarity between human and mouse tissue, eight-week-old female Thy1-YFP mice were induced with MOG_{35-55} to assess mitochondrial dynamics longitudinally in disease and to determine when mitochondria dysfunction occurs in the context of demyelination, inflammation, and axon damage (Hasselmann et al., 2017c). After EAE induction, mice began to show clinical disease severity around Day 10 post-EAE and reached a peak score of about 2.5 by Day 19 (**Figure 4A**). This average score persisted throughout EAE D60. A subgroup of these mice were either perfused for immunohistochemistry or their mitochondria were isolated from the cerebellum for functional studies and Western blot at peak EAE disease (EAE D21) or chronic EAE disease (EAE D40, EAE D60).

EAE mice show alterations in gait early and decreased motor strength in EAE

The walking gait test (WGT) was performed to determine if there are alterations with gait in the EAE mice that could be attributed to cerebellar dysfunction. For these behavioral tests, we wanted to utilize mice that were not too sick on the clinical disease severity score to allow us to measure strides without compensating for mice that have their hind limbs paralyzed. This way, we used mice with a clinical disease severity score of 3 or less before the mice exhibited any type of hind limb paralysis. Mice front feet were painted with red paint and the hind feet were painted with blue paint, and the mice were placed at the edge of a runway and walked at least three consecutive strides. Stride length, frontpaw width, hindpaw width, and frontpaw/hindpaw overlap were measured (**Figure 4B**). EAE mice had a significant decrease in stride length early in EAE (EAE Day 13) compared to normal mice that persisted throughout EAE to EAE D64 (**Figure 4C**). However, there was no significant difference in frontpaw width, hindpaw width, or frontpaw/hindpaw overlap between EAE mice and normal mice (**Figure 4D-F**). We also attempted to perform the WGT on mice that exhibited a clinical disease severity score of 4, but these strides, especially the hindlimbs, were difficult to measure. While the WGT is not a behavioral test purely representative of cerebellar dysfunction, the alterations in the EAE mice demonstrate that their decreased stride length could be indicative of dysfunction within the cerebellar circuitry. Next, we performed the rotarod test to address whether EAE mice had alterations in motor strength. The rotarod test is a motor test where the mice balance on a rod rotating at 16 rotations per minute. EAE mice remained

on the rotarod for significantly less time compared to normal mice beginning at early EAE D13 (**Figure 4G**).

EAE mice have demyelination and inflammation in the granule cell layer and white matter of the cerebellum

Due to their contributions to neurodegeneration in EAE and disability in MS, both myelin and inflammation were characterized in the granule cell layer (GCL) and white matter (WM) of the cerebellum. The GCL is where Purkinje cell and climbing axons are located, and the WM is where all of the axons of the cerebellar cortex exit towards the cerebellar peduncles (**Figure 5B**). Mice were perfused at each timepoint longitudinally and sagittal slices of the cerebellum were processed for immunohistochemistry. When assessing the cerebellum as a whole, there was a visual decrease in myelin basic protein (MBP) expression throughout the white matter and cerebellar peduncles in the EAE mice compared to the normal mice, especially in the chronic EAE mice (**Figure 5A**). 20x images were then taken at lobule IV specifically at the GCL and WM layers. There was a decrease in MBP expression in both of these layers in the EAE mice compared to the normal mice, beginning at peak EAE disease (EAE D21) and persisting through chronic EAE (EAE D40 and EAE D60) (**Figure 5C,D**). These results are similar to our previously published study assessing changes in the cerebellum at EAE D70 (MacKenzie-Graham et al., 2009).

To assess inflammation in the cerebellum after EAE induction, we used ionized calcium binding adaptor molecule 1 (Iba1) which is a marker for microglia and macrophages. There was an increase in Iba1 expression in both the GCL and WM in the EAE mice compared to the normal mice at EAE D40 and EAE D60 (**Figure 5E, F**). We also saw demyelination in the white matter with electron microscopy (EM) (**Figure 5G**). Within the axons, we also saw mitochondria morphology change between the normal and EAE mice. Specifically, the EAE mice had more swollen and round mitochondria compared to the normal mice.

EAE mice have a decrease in coupled respiration at peak disease

To characterize mitochondrial dynamics within the cerebellum, mitochondria were isolated from the cerebellum and the Seahorse XFp Analyzer Mito Stress test was performed (Agilent, San Diego, CA) (**Figure 6A**). The Mito Stress test allows us to evaluate the functionality of the respiratory chain in the mitochondria by real-time monitoring of the oxygen consumption rate (OCR), which is primarily consumed by glucose metabolism through the citric acid cycle. Specific inhibitors are used to target components of the electron transport chain to determine what components are affecting overall oxidative phosphorylation. First, basal respiration rate is measured with the added substrates pyruvate and malate, called state 2 respiration. Then, Complex 1-dependent respiration in state 3 is measured, which measures the capacity of the mitochondria to metabolize oxygen in the presence of ADP, a substrate for ATP synthase (Complex V),

called coupled respiration. After, oligomycin is added to terminate coupled respiration through inhibition of ATP synthase. Oligomycin decreases proton flux through ATP Synthase which causes the accumulation of protons within the cristae. This results in a reduction of electron transport and oxygen consumption, demonstrating state 4 respiration. Afterward, maximal respiration is measured by adding the protonophore Carbonyl cyanide-4 (trifluoromethoxy) phenylhydrazone (FCCP), an uncoupler agent of the respiratory chain that collapses the proton gradient and disrupts the mitochondrial membrane potential. This allows us to also measure spare respiratory capacity, or uninhibited electron flow through the electron transport chain and maximal oxygen consumption by complex IV. The difference between the uncoupled and basal OCR is calculated as the spare respiratory capacity (SRC). Lastly, injection of rotenone (Complex I inhibitor) and antimycin (Complex III inhibitor, specifically cytochrome C reductase) concurrently blocks the flux of electrons through the electron transport chain so that no oxygen was further consumed at cytochrome c oxidase (non-mitochondrial respiration rates). The averaged traces between the EAE mice and normal mice are demonstrated in **Figure 6B**. There was a significant decrease in coupled respiration (State 3) between the EAE mice and normal mice at EAE D21 (**Figure 6**). However, there was no differences in basal respiration, uncoupled respiration, and SRC between the EAE mice and normal mice (**Figure 6C,E,F**). Furthermore, there were no significant changes in basal respiration, coupled respiration, uncoupled respiration, and spare respiratory capacity at chronic EAE compared to normal (**Figure 7**).

EAE mice have alterations in the electron transport chain

Western blot (WB) was also performed to determine whether there were pathological changes with oxidative phosphorylation even though there were no aberrant changes functionally with the XFp Mito Stress test (**Figure 8A**). Interestingly, WB results showed decreased protein levels of the MTC01 subunit of COXIV in cerebellar mitochondria of EAE mice compared to normal mice at EAE D40 and EAE D60 (**Figure 8E**), appearing at the same time as when no functional changes are apparent with the Seahorse XFp Analyzer. There was no significant differences in any of the other complexes between the EAE mice and normal mice (**Figure 8B-D,F**) or between EAE D21 mice and normal mice**.**

EAE mice have no changes in mitochondrial fission or fusion in the cerebellum

Mitochondria alter their shape to meet energy demand, which is regulated by fission and fusion. Fission is utilized when mitochondria need to divide to reach more places to meet energy demand, while fusion is used when mitochondria are damaged or when energy demand decreases. Dynamin-related protein 1 (Drp1) is one of the main proteins that regulates mitochondrial fission (**Figure 9A**), while Mitofusin2 (Mfn2) is one component that regulates mitochondrial fusion (**Figure 9C**). EAE mice had no difference in fission or fusion from the isolated cerebellum compared to the normal at any timepoint (**Figure 9B,D**).

EAE mice have decreased mitochondrial anchoring

To determine whether mitochondria transport is altered in EAE longitudinally, we measured syntaphilin (Snph), which is a protein located in axons and is often used as a measure of anchored mitochondria (**Figure 10A**). EAE mice had decreased Snph expression at EAE D40 and EAE D60, indicating that there is decreased mitochondrial anchoring likely for mitochondria to be transported to places of higher energy demand.

Discussion

The purpose of this study was to determine when mitochondria dysfunction occurs in the cerebellum during EAE, a mouse model that consists of demyelination, inflammation, and neurodegeneration. To do this, female Thy1-YFP mice were induced with EAE and assessed for changes in mitochondria morphology, mitochondria function, and mitochondria pathology longitudinally in disease. These changes were assessed at peak disease at EAE D21 and at chronic disease at EAE D40 and EAE D60. Our lab has previously demonstrated a loss of the cerebellar cortex layer, Purkinje cell loss, and demyelination in the cerebellum at EAE D70 (MacKenzie-Graham et al., 2009), however, the mitochondrial changes have not yet been elucidated.

The rotarod test was used as a measure of motor function to demonstrate that the EAE mice had motor disability in addition to using the daily clinical disease score. This has been demonstrated in previous studies with our lab (Moore et al., 2014; Karim et al., 2018). In this study, we also determined whether there were abnormalities with gait using the walking gait test. The EAE mice demonstrated abnormalities of gait with decreased stride length compared to the normal mice. Our study only used EAE mice with a clinical disease severity score of 3 or below, due to the fact that mice with a score of 4 had both hindlimbs paralyzed and were difficult to measure. While the walking gait test is not a pure cerebellar test, dysfunction with gait can still be attributed to cerebellar dysfunction (Louis, 2018), in addition to dysfunction in the spinal cord or motor cortex (Baker, 2018).

Other studies measuring alterations in mouse gait have used the MotoRater gait analysis or kinematic gait analyses, which are more specific in assessing subtle gait pateterns. The MotoRater gait analysis test is a test that has been previously used in the SJL model of EAE that measures additional aspects including the distance between the floor and the tail (de Bruin et al., 2016), and the kinematic gait analysis is used to assess changes in joint movement change in mice, which has been used in MS patients (Fiander et al., 2017).

Via immunofluorescence we demonstrated demyelination, inflammation, and axon damage at EAE D21 that persisted throughout EAE D60. This is consistent with our previous results in addition to other sources ((Karim et al., 2019; Sekyi et al., 2021). Demyelination has been observed in the cerebellum as early as EAE D14 (Yan et al., 2019) through EAE D66 (MacKenzie-Graham et al., 2009; MacKenzie-Graham et al., 2012; Hamilton et al., 2019). Regarding inflammation, microglia comprise of about 10% of total cells in the CNS and are the resident immune cells (Nimmerjahn et al., 2005; Salter and Stevens, 2017). Studies have shown that microglia and macrophages contribute to the pathogenesis of disease progression (Rawji and Yong, 2013; Chu et al., 2018). Under normal physiological conditions there are few infiltrating macrophages into the CNS. However, when coupled with a compromised blood brain barrier (BBB), macrophages enter the CNS and release a combination of proinflammatory cytokines that further contribute to the inflammatory and degenerating milieu. The acute phase of MS and EAE is thought to have classically activated M1 macrophages that release

proinflammatory cytokines and induce tissue damage, demyelination, and neurodegeneration (Almolda et al., 2011; Jiang et al., 2012). The M2 macrophages seem to undergo a gradual increase until peak disease, when the amount of M1 cells decreases (Shin et al., 2012). The thought is that during chronic EAE, M2 microglia and macrophages become the dominant type in the CNS where anti-inflammatory cytokines are released to mediate EAE suppression and to contribute to tissue repair (Jiang et al., 2012).

To determine changes in mitochondrial dynamics throughout EAE longitudinally, cerebellums were dissected and were used for the Seahorse XFp analyzer to determine if there were alterations in mitochondria function. In order to evaluate the functionality of the respiratory chain, we measured Complex I-dependent respiration in state 3 (using the substrates pyruvate and malate) and maximal respiration (Djordjevic et al., 2020) by adding the uncoupler FCCP. State 3 respiration measures the capacity of the mitochondria to metabolize oxygen in the presence of ADP, which is a substrate for the ATP synthase (Complex V).

There was no difference in basal respiration, uncoupled respiration, and spare respiratory capacity at EAE D21 (peak EAE) compared to normal mice. While this lack of changes was not expected, we suspect that this may be due to the various cell types in the cerebellum. Peak EAE presents demyelination alongside a decrease in MBP and an

increase in Iba1 expression. We would expect that the oligodendrocytes are dying at peak EAE disease, causing an increase in metabolic demand in the neuron. While neuronal mitochondria may have increased activity in addition to astrocytes and microglia (**Figure 3B**), these changes are confounded with oligodendrocytes death and some neurons beginning the degenerating process. All of this activity happening simultaneously may be partly why there are very few changes were observed utilizing the Seahorse. There was a significant decrease in coupled respiration observed at the Peak EAE timepoint. Adding ADP converts the state 2 respiration to state 3 and results in rapid oxygen consumption and ATP formation (Salabei et al., 2014). The significant decrease in coupled respiration in the EAE mice could be due to less functional ATP Synthase, although there was no significant difference in ATP5A between the normal mice and EAE mice at peak EAE (**Figure 6A**). While alterations in ATP production and ATP Synthase have not been demonstrated in EAE or postmortem MS tissue, a decrease in nuclear encoded genes for ATP Synthase has been observed in SPMS postmortem tissue (Dutta et al., 2006). However, after peak EAE disease we no longer see functional differences with the mitochondria between EAE mice and normal mice (**Figure 6**). At the chronic EAE timepoint, more neurodegeneration is occurring in the presence of activated microglia and astrocytes. While there is likely less mitochondria present in neurons overall due to the neurodegeneration, the increased mitochondrial content in microglia and astrocytes compensate for any functional or pathological changes.

Mitochondria respiratory chain western blot studies have shown changes in complex I, II, and III in the spinal cord with no change with complex IV (COXIV) expression (Ng et al., 2019). The differences in our results and theirs may be due to different parts of the CNS observed and differing amounts of EAE severity. Studies that compared severely sick EAE mice with moderately sick EAE mice found significant variations in Tom20 expression, which is a mitochondria protein (Hira et al., 2019). However, our studies are consistent with postmortem studies that demonstrated a decrease in COXIV expression in postmortem MS patients (Dutta et al., 2006; Mahad et al., 2008; Mahad et al., 2009; Campbell and Mahad, 2011; Licht-Mayer et al., 2020).

The subtle changes that we are seeing in the context of EAE may also be due to the complexity of the disease model itself. Astrocytes, microglia, oligodendrocytes, and neurons all make up the cellular milieu of the cerebellum. In disease states such as in EAE, the combination of astrogliosis, microgliosis, oligodendrocyte death, and lymphocyte infiltration all contribute to mitochondrial changes in a cell specific way. In addition, the average EAE score of the mice in this experiment was a 2.5, which may correspond with a score of 4 with MS patients on the expanded disability status scale (EDSS). Postmortem studies show drastic differences in mitochondria content and activity, however that may be due to the accumulated disability and degeneration that occurred with these patients over their lifetime. Additional EAE studies using mice with hindlimb paralysis (a score of 4) that may correspond with MS patients with higher disability may be warranted to determine whether major degeneration needs to be present

to observe whole cerebellar changes in mitochondria pathology. Future studies can also assess mitochondria changes that are occurring in specific brain regions using brain slices punches with the Seahorse XFp analyzer (Underwood et al., 2020). Overall, we observed a decrease in coupled respiration at peak EAE, later resulting in decreased MTC01, a subunit of COXIV, at chronic EAE. Cell-specific studies assessing mitochondria function in specific cell types in animal models of MS are necessary to elucidate mitochondrial dynamics in the context of demyelinating disease.

A

Disease	n	MS phenotype	Age at death (yrs±SD)	Autolysis time (hrs±SD)	Average EDSS Score
Normal	4 (1 male, 3 females)	N/A	62.75±11.9	17.74±9.9	N/A
MS	11(5 males, 6 females)	RRMS, SPMS, PPMS	58.5±8.4	8.03±1.8	7.48

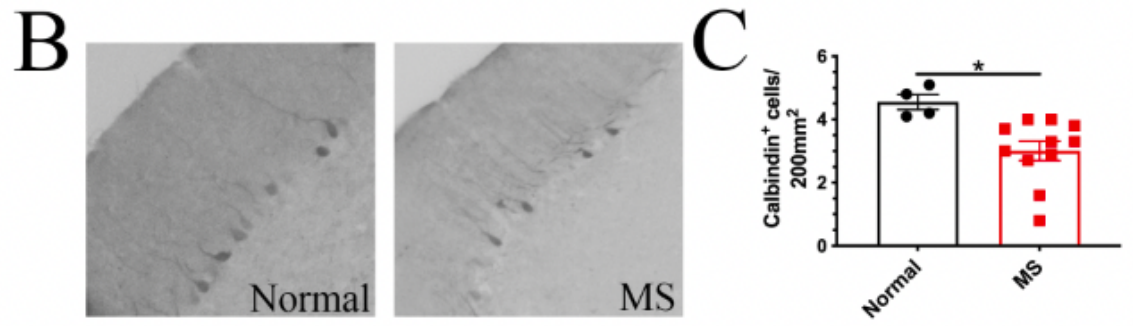

Figure 3: MS Postmortem tissue show decreased Purkinje cells compared to control tissue. (A) Table demonstrating the characteristics of the normal and MS tissue **(B)** Representative chromogen images of Calbindin, a marker for Purkinje cells. **(C)** There was a decrease in Calbindin+ cells in the MS tissue compared to the normal tissue. Normal: n=4, MS: n=11. Data are represented as mean ± SEM. Statistical differences between groups were determined using two-tailed, unpaired *t* test. *p < .05.

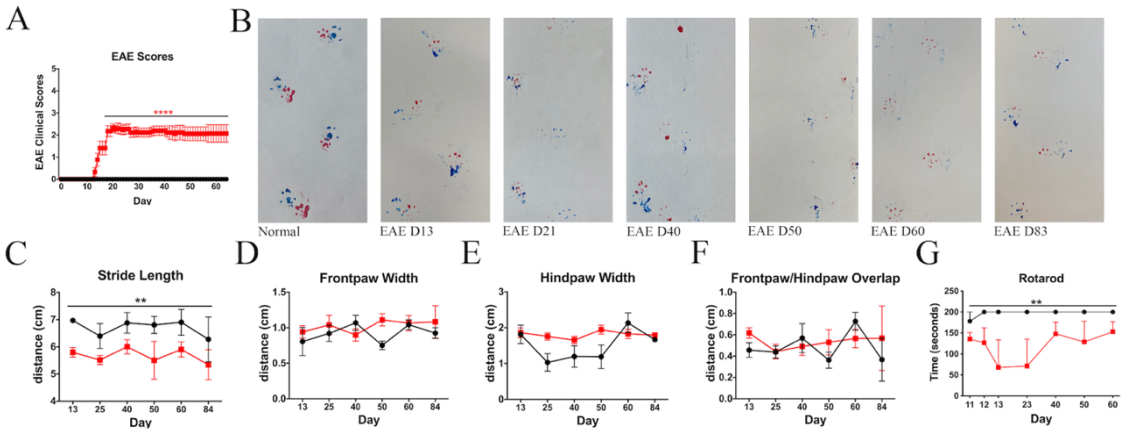

Figure 4: EAE mice show decreased motor strength and alterations in gait early in EAE. (A) Eight week old Thy1-YFP female mice were induced with MOG_{35-55} experimental autoimmune encephalomyelitis (EAE) as previously described. Mice began displaying clinical disease severity around EAE Day14 and reached peak EAE at EAE Day19 where severity persisted throughout the experiment. **(B)** Mice underwent the Walking Gait Test (WGT) throughout EAE to determine whether there are alterations in their gait that could be due to cerebellar dysfunction. Their front and hind feet were painted with red and blue paint, respectively. (B) shows representative footprint patterns of mice at various timepoints longitudinally throughout EAE. **(C)** EAE mice showed decreased stride length compared to the normal mice throughout EAE disease. **(D-F)** EAE mice did not show changes in frontpaw width, hindpaw width, or frontpaw/hindpaw overlap compared to normal mice throughout disease. (**G)** EAE mice remained on the rotarod for less time compared to the normal mice beginning at peak EAE disease and lasting through chronic EAE disease. Normal: n=13, EAE D21: n=20, EAE D40: n=15, EAE D60: n=9. Data are represented as mean $\pm$ SEM. Statistical differences between groups were determined using two-way unbalanced ANOVA with Dunnett's multiple comparisons test. *p < .05, ** p <.01.

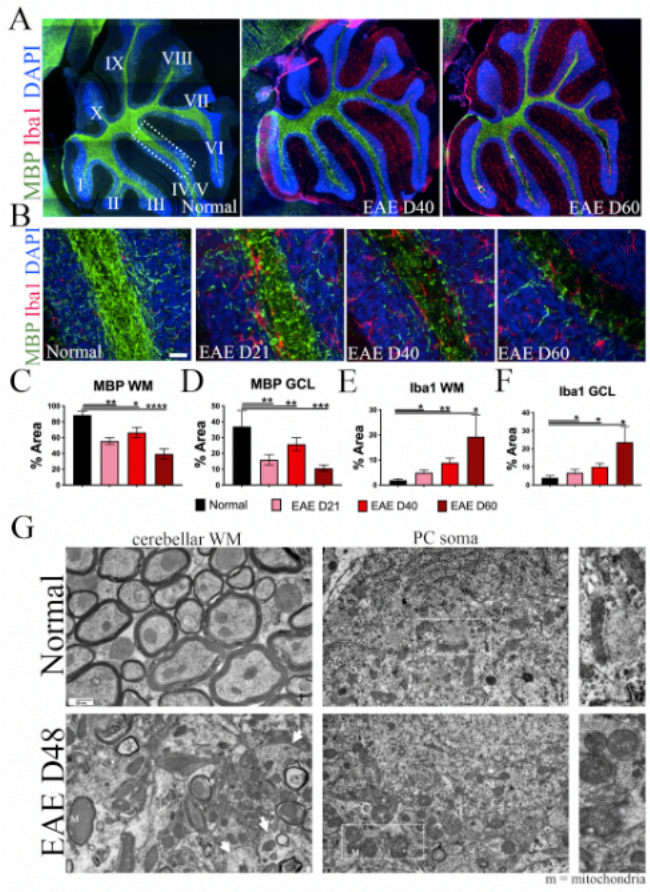

Figure 5: EAE mice have demyelination and inflammation in the granule cell layer and white matter of the cerebellum. (A) 10X montages displaying sagittal sections of myelin basic protein (MBP; green) + ionized calcium binding adaptor molecule 1 (Iba1; Red) + 4',6-diamidino-2-phenylindole (DAPI; blue). Representative montage of EAE D40 and EAE D60 show a decrease in MBP staining intensity with an increase in Iba1 staining intensity as compared to Normal. **(B)** Representative 20X images from lobule IV/V immunostained with MBP and Iba1 show a similar result as in (A) and were used to quantify staining intensity in the white matter (WM) and granule cell layers (GCL). **(C)** MBP WM analysis showed a decrease in MBP expression at EAE D21, EAE D40, and EAE D60 compared to normal, **(D)** which is also shown in the GCL. **(E)** There is an increase in Iba1 expression in the WM **(F)** and GCL at EAE D21, EAE D40, and EAE D60 compared to normal. Normal: n=7, EAE D21: n=8, EAE D40: n=8, EAE D60: n=6. Data are represented as mean ± SEM. Statistical differences between groups were determined using two-tailed, unpaired *t* test. *p < .05, **** p <.0001. Scale bar: 100µm.

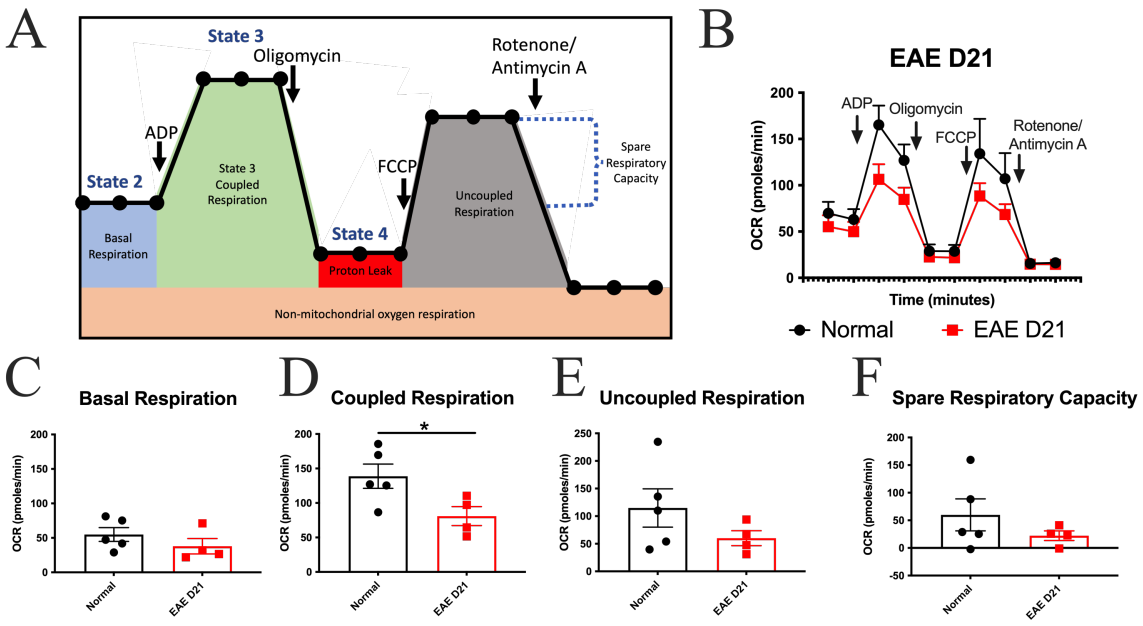

Figure 6: EAE mice have decreased coupled respiration at peak disease. (A) Seahorse XFp Cell Mito Stress Test Profile with isolated mitochondria. Initial oxygen consumption rate (OCR) is State 2 basal respiration. When ADP is added, this allows for State 3 Coupled Respiration. After the Oligomycin addition, this blocks ATP Synthase and allows us to determine ATP production and proton leak. FCCP is a proton uncoupler that allows for free proton movement along the mitochondrial inner membrane and allows for the measurement of uncoupled respiration. Lastly, Rotenone and Antimycin A block Complexes I and III of the electron transport chain and allows for the calculation of spare respiratory capacity. **(B)** Averaged traces from Seahorse XFp Mito Stress test representing Normal (black) and EAE D21 (red). **(C,E-F)** There was no difference in Basal Respiration, Uncoupled Respiration, and Spare Respiratory Capacity between normal and EAE D21. **(D)** There was a decrease in coupled respiration in the EAE D21 mice compared to the normal. Normal: n=5, EAE D21: n=4. Data are represented as mean $\pm$ SEM. Statistical differences between groups were determined using two-tailed, unpaired *t* test. *p < .05.

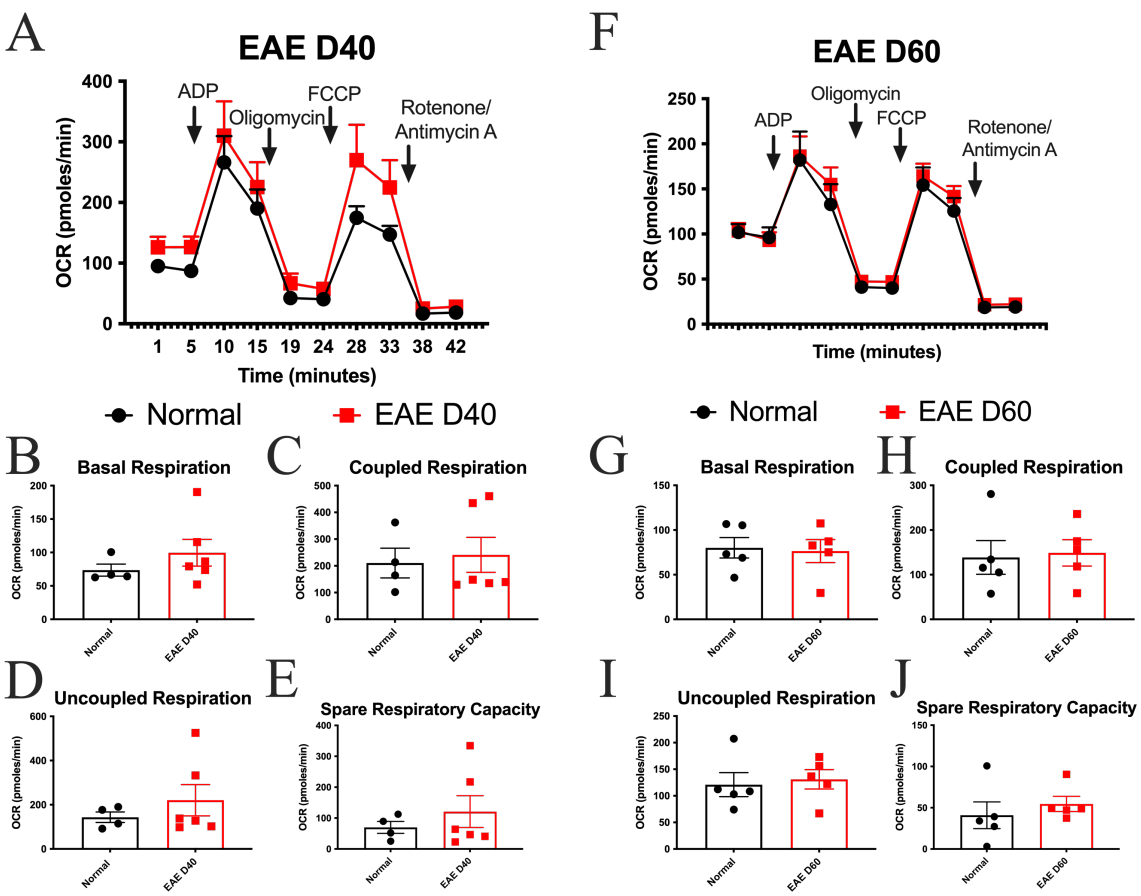

Figure 7: EAE mice do not show alterations in cerebellar mitochondria function at chronic disease. (A) Averaged traces from Seahorse XFp Mito Stress test EAE D40 representing Normal (black) and EAE D40 (red). **(B-E)** There was no difference in basal respiration, coupled respiration, uncoupled respiration, and spare respiratory capacity between EAE D40 and normal mice. **(F)** Averaged traces from Seahorse XFp Mito Stress EAE D60 representing Normal (black) and EAE D60 (red). Data are represented as mean ± SEM. **(G-J)** There was no difference in basal respiration, coupled respiration, uncoupled respiration, and spare respiratory capacity between EAE D60 and normal mice. Normal: n=9, EAE D40: n=6, EAE D60: n=5. Statistical differences between groups were determined using two-tailed, unpaired *t* test.

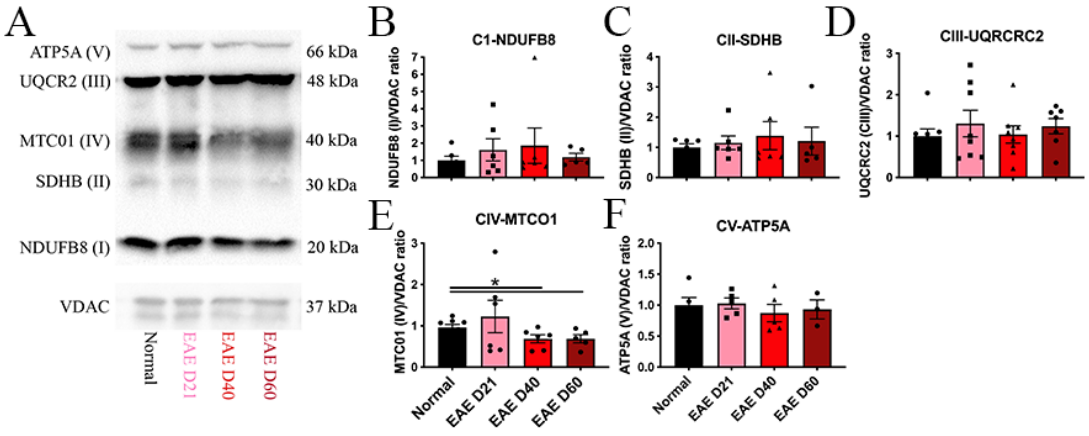

Figure 8: EAE mice have alterations in the electron transport chain. (A) Representative blot of OXPHOS subunits including COXI (NDUFB8; 20 kDa), COXII (SDHB 30 kDa), COXIII (UQCR2, 48 kDa), COXIV (MTC01, 40 kDa), and ATP Synthase (ATP5A, 66 kDa) with VDAC used as a loading control. **(B-D)** There is no significant difference in COXI, COXII, or COXIII expression between EAE and normal mice in the cerebellum. **(E)** There was a significant decrease in COXIV expression at EAE D40 and EAE D60 in the EAE mice compared to the normal mice. **(F)** There was no significant difference in ATP5A expression between normal mice and EAE mice. Normal: n=8, EAE D21: n=8, EAE D40: n=8, EAE D60: n=6. Data are represented as mean $\pm$ SEM. Statistical differences between groups were determined using two-tailed, unpaired *t* test. *p < .05.

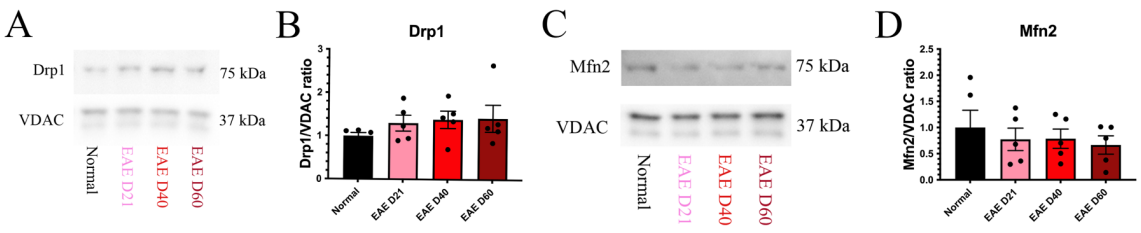

Figure 9: EAE mice have no difference in mitochondria fission or fusion. (A) Representative blot of dynamin-related protein 1 (Drp1) with Normal, EAE D21, EAE D40, and EAE D60. **(B)** There was no difference in Drp1 expression between EAE and normal mice. **(C)** Representative blot of mitofusin 2 (Mfn2) with Normal, EAE D21, EAE D40, and EAE D60. **(D)** There was no difference in Mfn2 expression between EAE and normal mice. Normal: n=5, EAE D21: n=5, EAE D40: n=5, EAE D60: n=5. Data are represented as mean $\pm$ SEM. Statistical differences between groups were determined using two-tailed, unpaired *t* test.

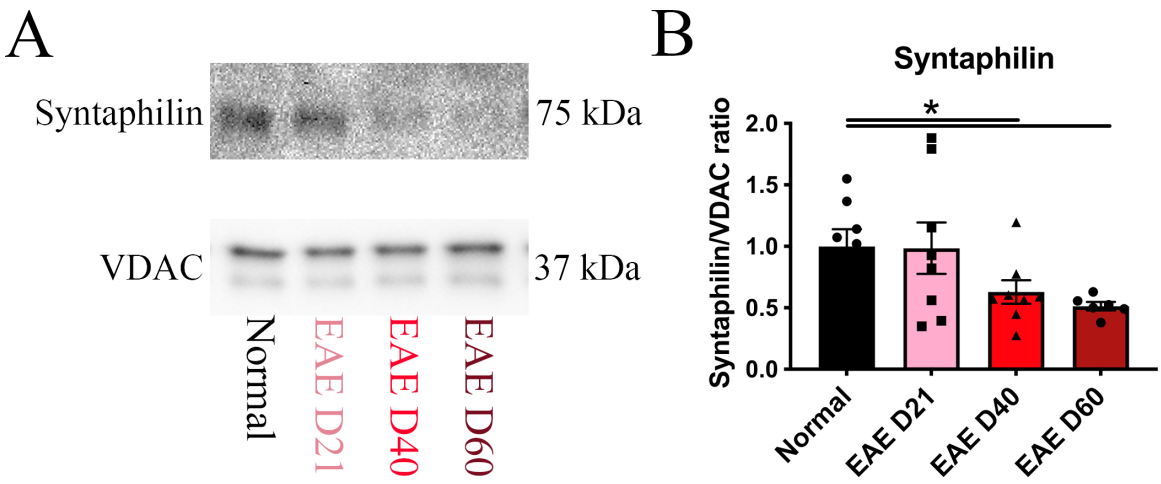

Figure 10: EAE mice have decreased mitochondrial anchoring. (A) Representative blot of syntaphilin with Normal, EAE D21, EAE D40, and EAE D60. **(B)** There was a decrease in Syntaphilin expression at EAE D60 and EAE D40 compared to normal mice. Normal: n=8, EAE D21: n=8, EAE D40: n=8, EAE D60: n=6. Data are represented as mean $\pm$ SEM. Statistical differences between groups were determined using two-tailed, unpaired *t* test. **p < .01.

Chapter 4: Mitochondrial dynamics are altered longitudinally independent of leukocyte infiltration in the cuprizone demyelinating mouse model

Abstract

Progressive MS patients exhibit tremors and impaired motor control due to pathology in cerebellar related circuits. In addition, alteration of Purkinje cells (PCs) in the cerebellum has been linked to cerebellar dysfunction and gait abnormalities in MS patients. Mitochondria are recruited to demyelinated axons to meet the increased energy requirements necessary to maintain conduction. However, if the demyelination continues, other factors including free radical accumulation can cause further mitochondrial dysfunction that contributes to axon damage. We hypothesize that chronic cuprizone (CPZ) diet-induced demyelination contributes to mitochondrial dysfunction. Cerebellar pathology mimicking progressive MS was investigated in the chronic demyelinating CPZ diet mouse model. CPZ is a copper chelator which is known to be toxic to mature oligodendrocytes that contributes to axon demyelination. 3, 6, 9, and 12 week CPZ (12wkCPZ) mice were compared to normal mice in the white and gray matter of the cerebellum using immunohistochemistry (IHC) with markers for myelin (myelin basic protein; MBP) and microglia (allograft inflammatory factor 1; Iba1). In addition, a subset of mice at weeks 6, 9, and 12 were sacrificed and their cerebellums were dissected for the Seahorse XFp Mito Stress test, a mitochondrial function test, and paired with Western blot for changes in mitochondrial pathology. CPZ mice demonstrated decreased MBP and increased Iba1 expression beginning at 6wkCPZ compared to normal mice. While alterations in mitochondria function was not visible with the Seahorse Mito Stress test, there was a significant decrease in mitochondria fusion at 12wkCPZ compared to normal.

Further cell-specific studies are needed to determine cell-specific mitochondria changes occurring in the context of demyelination.

Introduction

MS patients with tremors during their lifetime demonstrated cerebellar demyelination after death, emphasizing the importance of understanding cerebellar pathology in the context of MS (Kurtzke et al., 1977; Weinshenker et al., 1991; Koch et al., 2007). MS is characterized by the loss of oligodendrocytes, altered axonal transport and signaling resulting in neurodegeneration and disability (Gelfand, 2014). Before neurodegeneration, axons show adaptive mechanisms when they are demyelinated, such as increased mitochondria density and increased size (Mutsaers and Carroll, 1998). These changes have also been observed outside of the CNS (Suzuki, 1969; Jürgensmeier et al., 1998; Pfanner et al., 2019).

There is still no direct conclusion regarding the cause of MS, but it is known that mitochondrial dynamics are altered. While there are genetic and environmental risk factors that increase the likelihood of developing MS, there are also other theories, such as the "inside-out" model (Stys et al., 2012; Caprariello et al., 2018; Titus et al., 2020). The "inside-out" hypothesis is a theory stating primary pathogenesis of oligodendrocyte injury results in degeneration due to activation of a reactive inflammatory response. The "outside-in" hypothesis is a primary pathogenesis of autoimmune inflammation followed by myelin degradation and neurodegeneration (Stys et al., 2012). Due to this, there is a need to understand the contribution of mitochondrial dysfunction and pathology to MS to determine the role of this organelle in neurodegeneration.

One animal model used to study demyelination and neurodegeneration is the cuprizone (bis-cyclohexanone-oxalyldihydrazone, CPZ) model. CPZ is a copper chelator that allows for reproducible induction of acute or chronic demyelination with astrogliosis and microgliosis (Matsushima and Morell, 2001; Kipp et al., 2009; Moore et al., 2014; Lapato et al., 2017; Atkinson et al., 2019)). This allows the CPZ model to be beneficial when using therapeutics to assess changes in myelination and neurodegeneration. 6 weeks of the CPZ diet has been shown to demonstrate substantial demyelination (Matsushima and Morell, 2001; Kipp et al., 2017). While the mechanism is unknown, it is thought that mature oligodendrocytes are selectively vulnerable to CPZ . When oligodendrocyte death occurs, the demyelinated axons become more susceptible to attacks by brain intrinsic and inflammatory mediators. Specifically, copper chelation is thought to inhibit complex IV (COXIV) of the mitochondrial respiratory chain (Xu et al., 2013). However, its effect on other cell types with oxidative phosphorylation is less understood.

The purpose of this study was to determine mitochondrial changes during the course of longitudinal cuprizone diet. Female mice were placed on a cuprizone diet and a subset was assessed at 3, 6, 9, or 12 weeks of CPZ diet to determine when mitochondrial functional and pathological changes are present in the cerebellum. Demyelination was evident in the cerebellar white matter and granule cell layers beginning at 6wkCPZ compared to normals, in addition to microgliosis. Cerebellar mitochondrial dysfunction was not evident with the Seahorse XFp Mito Stress at any point longitudinally with CPZ, but a decrease in mitochondrial fusion was observed at 12wkCPZ compared to normal.

Results

Cuprizone mice exhibit no differences in motor activity or gait longitudinally

Eight-week-old PLP-eGFP female mice were placed on the 0.2% cuprizone diet for either 3, 6, 9, or 12 weeks to assess demyelination and mitochondrial dynamics longitudinally in the cerebellum (3wkCPZ, 6wkCPZ, 9wkCPZ, 12wkCPZ). At each timepoint, a subgroup of mice were either perfused for immunohistochemistry (IHC), or their cerebellums were dissected to assess mitochondrial function and pathology. A subgroup of mice remained on a normal diet and were considered normal.

To determine whether CPZ caused alterations in gait, which could be indicative of cerebellar dysfunction, we performed the walking gait test (WGT) and the rotarod. The WGT was used to determine whether the CPZ mice had changes in gait compared to the normal mice. Mice front and hind feet were painted with red and blue paint respectively and walked along a white sheet of paper. Stride length, frontpaw width, hindpaw width, and frontpaw/hindpaw overlap were measured after each mouse walked three consecutive strides (**Figure 11A**). There was no significant difference in any parameter of the WGT between the CPZ mice and the normal mice (**Figure 11C-F**). The rotarod test is a motor test where the mice balance on an accelerating rotating rod for up to 200 seconds. There was no difference in latency on the rotarod between the CPZ mice and normal mice at any time point (**Figure 11B**). Overall, CPZ mice do not show alterations in rotarod or gait compared to the normal mice, even after 12 weeks on the CPZ diet.

Cuprizone mice exhibit demyelination, microgliosis, and morphological mitochondrial changes longitudinally in the granule cell layers and white matter of the cerebellum

To determine the longitudinal effects of the CPZ diet on myelination and inflammation in the cerebellum, mice were perfused at each timepoint and sagittal slices of the cerebellum were processed for IHC (**Figure 12**). 10X montages demonstrate a decreased overall expression of myelin basic protein (MBP), a protein component of myelin, with an increased overall expression of ionized calcium binding adaptor molecule 1 (Iba1), a marker for microglia and macrophages (**Figure 12A**). 20X images of lobules IV/V indicated by the dashed white rectangle were assessed in the granule cell layers (GCL) and the white matter (WM) for analysis (**Figure 12B**). The GCL was assessed because this is where Purkinje cell (PC) axons are located, which are heavily myelinated axons. The WM was assessed because this is the bundle of fibers leaving the cerebellar cortex which includes PC axons. There was a significant decrease in MBP expression and an increase in Iba1 expression in both of these layers beginning at 6wkCPZ and persisting through 12wkCPZ compared to the normals (**Figure 12C-F**).

We also assessed myelination in the WM using transmission electron microscopy (EM). There was a decrease in myelinated axons in the 9wkCPZ mice compared to the normal mice (**Figure 12G**). We also assessed mitochondrial visually in the myelinated axons with EM. Compared to the mitochondria in the normal myelinated axons, the mitochondria in the 9wkCPZ axons appeared bigger and rounder.

Cuprizone mice do not show functional mitochondria changes with the Seahorse XFp Analyzer

The next step was to determine whether there were alterations in mitochondria within the cerebellum and to determine whether these changes correlated with changes in myelination and microgliosis. Mitochondria were isolated from the whole cerebellum at 6wkCPZ, 9wkCPZ, and 12wkCPZ and the Seahorse XFp Analyzer Mito Stress test was performed (Agilent, San Diego, CA). Initially, basal respiration rate is measured in the presence of pyruvate and malate, indicative of state 2 respiration. Then, Complex 1-dependent respiration in state 3 was measured, which measures the capacity of the mitochondria to metabolize oxygen in the presence of ADP, a substrate for ATP synthase (Complex V), called coupled respiration. Next, oligomycin is added to terminate coupled respiration by inhibition of ATP synthase. Oligomycin decreases proton flux through complex V which causes the accumulation of protons within the cristae. This results in a reduction of electron transport and oxygen consumption, demonstrating state 4 respiration. Maximal respiration is then measured by injecting the protonophore Carbonyl cyanide-4 (trifluoromethoxy) phenylhydrazone (FCCP), an uncoupler agent of the respiratory chain that collapses the proton gradient and disrupts the mitochondrial membrane potential. This allows us to also measure spare respiratory capacity, or uninhibited electron flow through the electron transport chain and maximal oxygen consumption by Complex IV. The difference between the uncoupled and basal OCR is considered to be the spare respiration capacity. Finally, injection of rotenone (Complex I inhibitor) and antimycin (Complex III inhibitor, specifically cytochrome C reductase)

concurrently blocks the flux of electrons through the electron transport chain so that no oxygen was further consumed at cytochrome c oxidase (non-mitochondrial respiration rates). The Seahorse XFp Mito Stress test was performed at 6wkCPZ, 9wkCPZ, and 12wkCPZ. There was no difference in basal respiration, coupled respiration, uncoupled respiration, or spare respiratory capacity in the 6wkCPZ mice compared to the normal (**Figure 13**). We also performed this test at chronic CPZ (9wkCPZ and 12wkCPZ) to determine if there were functional changes after a longer time on the CPZ diet, but there were still no changes between any parameter between the 9wkCPZ mice and normal mice (**Figure 14,15**).

12wkCPZ mice have decreased mitochondrial fusion

To determine whether the CPZ diet altered mitochondria pathology in the cerebellum, isolated mitochondria were also measured by Western blot for OXPHOS subunit expression, mitochondria fission and fusion, and mitochondrial anchoring. First, an OXPHOS cocktail was used to determine whether there were pathological changes to subunits dedicated to oxidative phosphorylation (**Figure 16**). When assessing subunits for COXI, COXII, COXIII, COXIV, and ATP Synthase, there was no difference in any subunit expression between the 3wkCPZ, 6wkCPZ, 9wkCPZ, or 12wkCPZ mice compared to the normal mice, similar to the functional studies shown from the Seahorse XFp Analyzer. Next, mitochondrial fission and fusion were assessed with Dynamin related protein 1 (Drp1) and Mitofusin 2 (Mfn2), respectively (**Figure 17**). Mitochondria

are dynamic and are thought to undergo fission when there is a greater energy demand and mitochondria need to be located in more places throughout the cell (Chen and Chan, 2009). Similarly, mitochondria undergo fusion when there is no longer a greater energy demand. In addition, they can undergo fusion when there is some damage, because two mitochondria fusing allows for an undamaged genome to replace the damaged mitochondria genome. There was no difference in Drp1 expression between 3wkCPZ, 6wkCPZ, 9wkCPZ, or 12wkCPZ mice and normal mice (**Figure 17A,B**). However, there was a significant decrease in Mfn2 expression between the 12wkCPZ mice and normal mice, indicating that there is decreased mitochondria fusion occurring at chronic CPZ (**Figure 17C,D**).

Discussion

The purpose of this study was to determine the mitochondrial changes that occur in a mouse model of MS that lacks blood brain barrier permeability and leukocytic infiltration into the CNS. MS patients have demonstrated abnormalities in the cerebellum during their lifetime and in postmortem tissue. MS patients display T2 hypointensity in their subcortical gray matter with magnetic resonance imaging (MRI) with ambulatory impairment (Tjoa et al., 2005). MS patients with tremors have cerebellar demyelination after death (Kurtzke et al., 1977; Weinshenker et al., 1991; Koch et al., 2007). PCs in postmortem MS patients showed changes in phosphorylation states, Purkinje axonal spheroids, and PC loss (Redondo et al., 2015). In addition, lesion burden in MS patients can vary throughout the CNS and is also dependent on the type of MS (Kis et al., 2008). For example, late-onset MS patients have more frequent spinal cord lesions, but less frequent cerebellar lesions (Kis et al., 2008). Interestingly, one study also demonstrated less cerebellar activation with MS compared with controls in function MRI studies, suggesting that the cerebellum may contribute to working memory impairment in MS (Li et al., 2004).

The CPZ model is a reproducible model that allows for consist demyelination (Matsushima and Morell, 2001; Kipp et al., 2009; Steelman et al., 2012). The demyelinating occurs early and has only been shown to disrupt mature oligodendrocytes while sparring other CNS cell types (Kipp et al., 2017). Substantial demyelination is

observed by 3 weeks, but specifically in the corpus callosum (Matsushima and Morell, 2001; Kipp et al., 2009). By 4-5 weeks of age, it's been shown that most axons in the brain are demyelinated. In addition, the cerebellum has also demonstrated demyelination after the CPZ diet (Groebe et al., 2009; Skripuletz et al., 2010). It has also been shown that removal of CPZ from the diet can allow for remyelination (Matsushima and Morell, 2001; Kipp et al., 2009). We hypothesized that mitochondrial changes are an early trigger for a cascade of events leading to demyelination, inflammation, and neurodegeneration.

We did not observe differences at any timepoint with the rotarod and the walking gait test in the cuprizone mice compared to the normal mice (**Figure 11**). The lack of differences between the groups using the WGT is likely due to the lack of subtlety in the behavioral test used. While we attempted to measure obvious changes in gait by measuring distances in stride parameters, one study found that CPZ-fed mice fed for 37 days of 0.2% cuprizone exhibited more foot slips in walking ladder and beam tests compared to controls (Sen et al., 2020). Another study used a DigiGait analysis to measure the swing time of the mice feet as they walked and found differences in a recovered cuprizone group compared to a control group (Zhan et al., 2021). These tests are more sensitive and are also computerized, allowing for a more defined analysis of gait patterns in the mice.

We also assessed myelination and microgliosis in the cerebellum to determine when these changes occur regionally (**Figure 12**). Demyelination is known to occur in the CPZ

model with the presence of microgliosis (Blakemore, 1972; Ludwin, 1978; Matsushima and Morell, 2001). Previous studies assessing myelination in the cerebellum after CPZ diet showed decreased PLP and MBP mRNA levels in the entire cerebellum beginning at 1 and 2 weeks after the CPZ diet, respectively (Groebe et al., 2009). Groebe et al. did not show any changes in the WM or GCL in the cerebellum, however they only assessed the changes up to five weeks (Groebe et al., 2009). While there was no significant difference in PLP expression with immunohistochemistry, this study did observe more swollen axons with electron microscopy in the WM after 5 weeks of CPZ (Groebe et al., 2009) Another study demonstrated weak demyelination in the WM and GCL areas after 4 weeks of the CPZ diet (Skripuletz et al., 2010). However, this demyelination was very apparent by 12 weeks (Skripuletz et al., 2010). It is thought that microglia activation occurs within the first two weeks the mice are on the CPZ, where it reaches its peak of activation around 4-6 weeks on the CPZ diet (Morell and Wiesmann, 1984; Hiremath et al., 1998; Matsushima and Morell, 2001). This is consistent with what we see with immunofluorescence. It is assumed that the role of microglia and macrophages is to clear myelin debris. However, these cells are also located near the lesions, so these cell types could be attempting to aid in remyelination (Blakemore, 1972; Ludwin, 1978; Matsushima and Morell, 2001).

Our EM comparing myelinated axons and mitochondria morphology between normal and 9wkCPZ mice showed changes we expected (**Figure 13G**). One previous study demonstrated megamitochondria in oligodendrocytes by 3 weeks of cuprizone in the

corpus callosum and superior cerebellar peduncle, which could be due to the copper chelation within the mitochondrial respiratory chain (Acs and Komoly, 2012). We see enlarged mitochondria in our myelinated and demyelinated axons in the 9wkCPZ mice. While the enlarged mitochondria in the demyelinated axons could be due to increased energy demand after demyelination, the enlarged mitochondria in the myelinated axons could indicate increased energy demand and stress in the axon before demyelination occurs. This study also demonstrates that mitochondria in neurons are affected by the CPZ diet, not just oligodendrocytes.

The overall mechanism of cuprizone is not completely understood, but it is known that it is a copper chelator that kills mature oligodendrocytes causing demyelination. Copper is an essential trace element for metalloenzymes, including copper-zinc superoxide dismutase and ceruloplasmin (Walshe and Munro, 1995; Zlotkin et al., 1995). It is important to note that cytochrome c oxidase, a major enzyme of the electron transport chain, may be affected with the CPZ diet due to the fact that it has copper centers (Suzuki, 1969). However, if CPZ binds copper in the electron transport chain, all cell types that contain mitochondria should be affected with the CPZ diet and not just mature oligodendrocytes. A decrease COXIV in PCs with immunohistochemistry was shown in the CPZ model, one of the first studies that demonstrates the effect of the CPZ diet on other cell types (Varhaug et al, 2020).

However, when we assessed functional mitochondria changes with the Seahorse XFp Analyzer, no significant differences were observed between the cuprizone mice and normal mice with basal respiration, coupled respiration, uncoupled respiration, and spare respiratory capacity (**Figures 13-15**). While this was not expected, this could be due to several factors. One reason could be that at the 6wkCPZ timepoint, there is demyelination occurring causing an increase in metabolic demand in the neuronal axons. However, this change is coupled with mature oligodendrocytes dying from the CPZ diet, causing a loss of mitochondria activity. These two major changes, in addition to an increase in microgliosis likely causing more activated mitochondria in these cell types as well, may display as no functional change when these mitochondria are pooled together for the analyzer. This concept may also translate to the very few pathological changes we observed in this CPZ model (**Figures 16,17**). There was no significant difference in any subunit of OXPHOS between cuprizone and normal mice at any time point. In addition, there was no difference in mitochondria fission.

We did observe a significant decrease in mitochondria fusion in the 12wkCPZ mice compared to the normal mice. Mitochondria are dynamic organelles that have a balance of fission and fusion to regulate their size and morphology. Mitochondrial fission is the division of one mitochondrion into two daughter mitochondria, while fusion is the fusion of two mitochondria resulting in one mitochondrion (Detmer and Chan, 2007; Chen et al., 2009). Defects in mitochondrial fission or fusion can contribute to mitochondrial fragmentation and eventually cell death (Jahani-Asl et al., 2010). Mfn2 regulates

mitochondrial fusion with mitofusin 1 and optic atrophy 1 (OPA1) (Chan, 2006). One study demonstrated that inhibition of Drp1, a component of mitochondrial fission, was protective in the experimental autoimmune encephalomyelitis (EAE) model of MS (Luo et al., 2017a). In addition, an increase in Mfn2 expression was shown in PLP4e mice, a demyelinating mouse model that contains extra copies of myelin genes (Thai et al., 2019). Typically, mitochondria may fuse either due to a decrease in energetic demand, or to increase mtDNA stability (Chen et al., 2010). The decrease in mitochondrial fusion that we observed at 12wkCPZ may be due to axon damage occurring within the neurons, preventing mitochondria from being transported along microtubules and fusing together. Future studies assessing axon damage longitudinally in the CPZ model in the cerebellum may allow us to further understand mitochondrial dynamics.

Overall, the functional and pathological mitochondria studies were performed on the entire cerebellum. Cell-specific studies may be necessary when assessing mitochondrial changes using the CPZ model to determine how mitochondria are affected in neurons after mature oligodendrocytes die. Understanding the pathophysiology of mitochondrial changes in animal models of MS is crucial to finding better therapeutics and improving the quality of life of patients with MS.

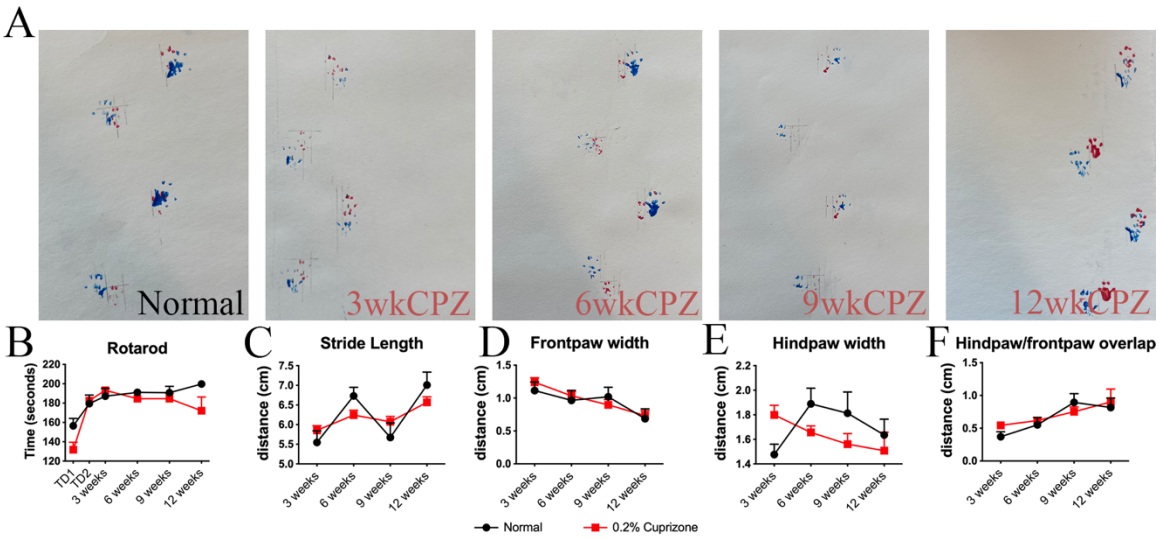

Figure 11: Cuprizone mice exhibit no differences in motor activity or gait longitudinally. (A) Eight week-old Thy1-YFP female mice ate a 0.2% Cuprizone (CPZ) diet for either 3, 6, 9, or 12 weeks. At each timepoint, mice were assessed with the walking gait test (WGT) to determine if there were alterations with their gait. Their front feet were painted red and their hind feet were painted blue and mice walked along a 60cm white sheet of paper. Example footprint patterns at each timepoint are shown in (A).**(B)** The rotarod test (used at an accelerating rate of 40-400rpm) was used to determine if mice had changes in motor function after the CPZ diet. There was no difference in time on the rotarod between the cuprizone mice and normal mice at any timepoint. **(C-F)** Cuprizone mice had no differences in stride length, frontpaw width, hindpaw width, and hindpaw/frontpaw overlap compared to the normal mice at any timepoint. Normal: n=8-24, 3wkCPZ: n=41-50, 6wkCPZ: n=16-34, 9wkCPZ: n=11-28, 12wkCPZ: n=5-11. Data are represented as mean ± SEM. Statistical differences between groups were determined using two-way unbalanced ANOVA with Dunnett's multiple comparisons test.

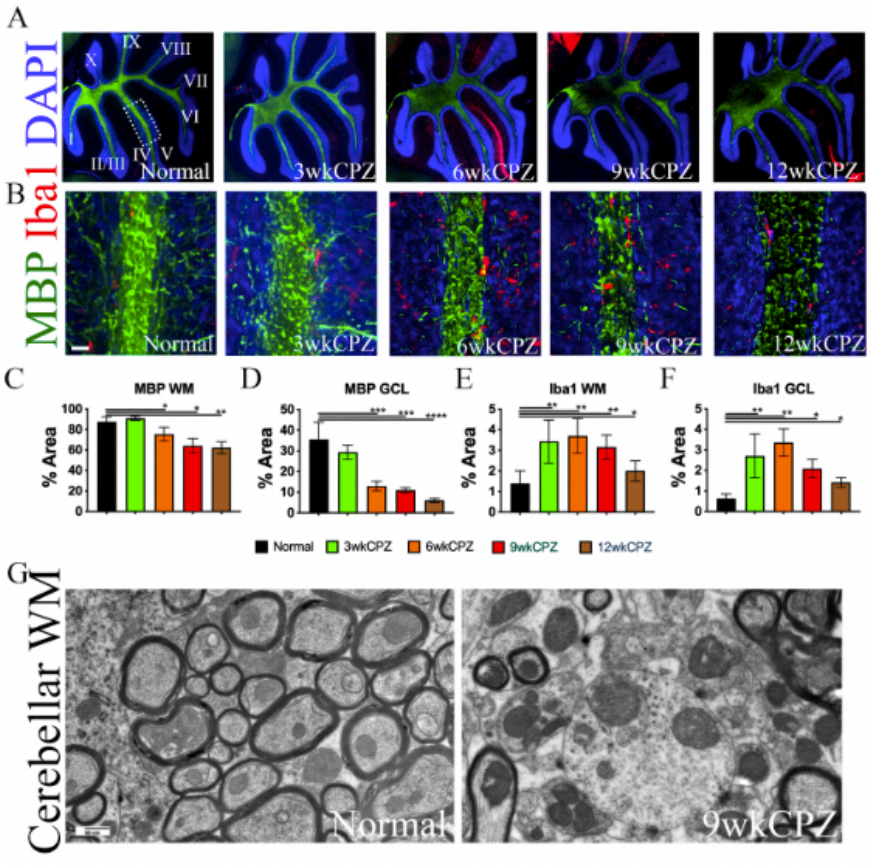

Figure 12: Cuprizone mice exhibit demyelination, microgliosis, and mitochondrial morphological changes longitudinally in the granule cell layers and white matter of the cerebellum.

(A) 10X montages showing myelin basic protein (MBP; green), ionized calcium binding protein (Iba1; red) with DAPI. Visually there is a decrease in MBP expression with an increase in Iba1 expression in the 6, 9, and 12wkCPZ mice compared to the normal mice. **(B)** 20X imaging representative images of cerebellar lobule IV/V. **(C)** MBP analysis in the white matter (WM) demonstrates a decrease in MBP expression in the 6wkCPZ, 9wkCPZ, and 12wkCPZ mice compared to the normal mice. **(D)** There is a significant decrease in MBP expression in the granule cell layer (GCL) in the 6wkCPZ, 9wkCPZ, and 12wkCPZ mice compared to the normal mice. (**E**) There is a significant increase in Iba1 expression in the 3wkCPZ, 6wkCPZ, 9wkCPZ, and 12wkCPZ mice compared to the normal mice in the WM **(F)** and the GCL layer. **(G)** Transmission electron microscopy showing cross sections of the cerebellar WM comparing myelinated axons in the normal vs. demyelinated axons in the 9wkCPZ mice. Normal: n=6, 3wkCPZ: n=9, 6wkCPZ: n=9, 9wkCPZ: n=10, 12wkCPZ: n=6. Data are represented as mean ± SEM. *p<0.05, **p<0.01, ***p<0.001, ****p<0.0001. Scale bars: 100µm, 50nm. Statistical differences between groups were determined using two-tailed, unpaired *t* test.

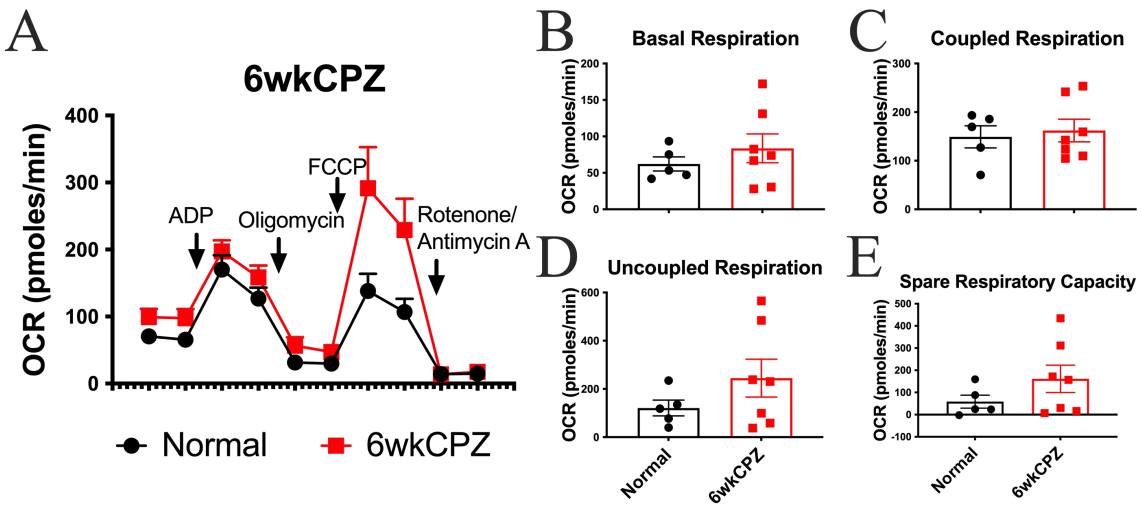

Figure 13: Cuprizone mice may not have differences in mitochondria function at 6wkCPZ. (A) Representative averaged traces for the Seahorse XFp Mito Stress Test showing normal (black) and 6wkCPZ (red). **(B-E)** Oxygen consumption rate (OCR) results from basal respiration, uncoupled respiration, spare respiratory capacity, and coupled respiration. There is no difference in these parameters between normal mice and 6wkCPZ mice. Normal: n=5, 6wkCPZ: n=7. Data are represented as mean ± SEM. Statistical differences between groups were determined using two-tailed, unpaired *t* test.

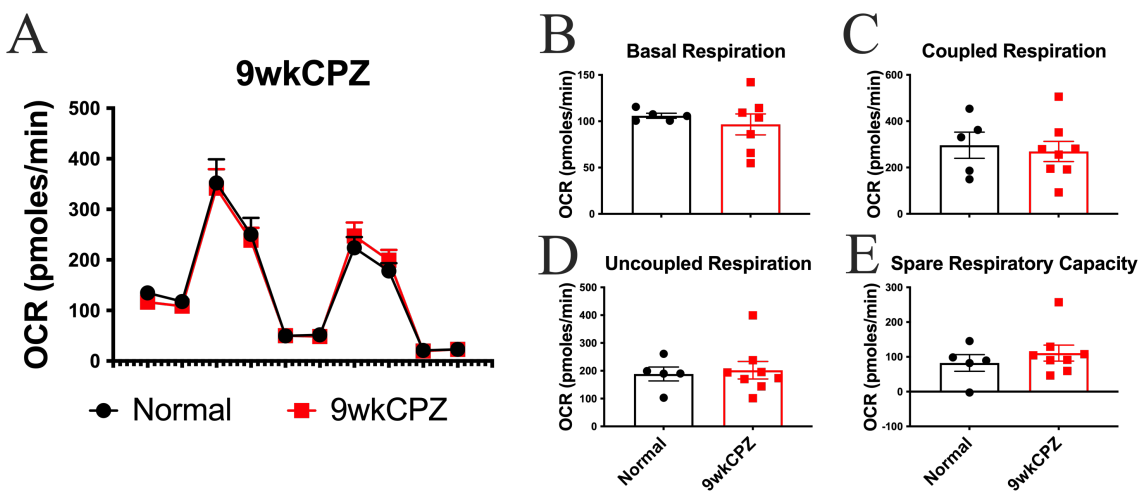

Figure 14: There is no difference in mitochondrial function at 9wkCPZ. (A) Representative averaged traces for the Seahorse XFp Mito Stress Test showing normal (black) and 9wkCPZ (red). **(B-E)** Oxygen consumption rate (OCR) results from basal respiration, uncoupled respiration, spare respiratory capacity, and coupled respiration. There is no difference in these parameters between normal mice and 6wkCPZ mice. Normal: n=5, 9wkCPZ: n=7. Data are represented as mean ± SEM. Statistical differences between groups were determined using two-tailed, unpaired *t* test.

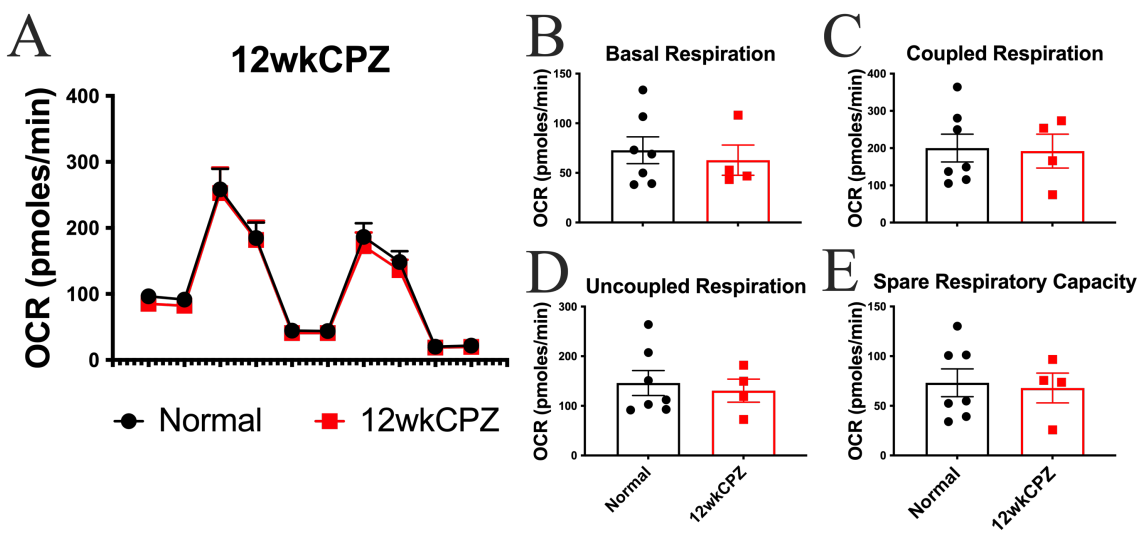

Figure 15: There is no difference in mitochondria function at 12wkCPZ. (A) Representative averaged traces for the Seahorse XFp Mito Stress Test showing normal (black) and 12wkCPZ (red). **(B-E)** Oxygen consumption rate (OCR) results from basal respiration, uncoupled respiration, spare respiratory capacity, and coupled respiration. There is no difference in these parameters between normal mice and 6wkCPZ mice. Normal: n=7, 9wkCPZ: n=4. Data are represented as mean ± SEM. Statistical differences between groups were determined using two-tailed, unpaired *t* test.

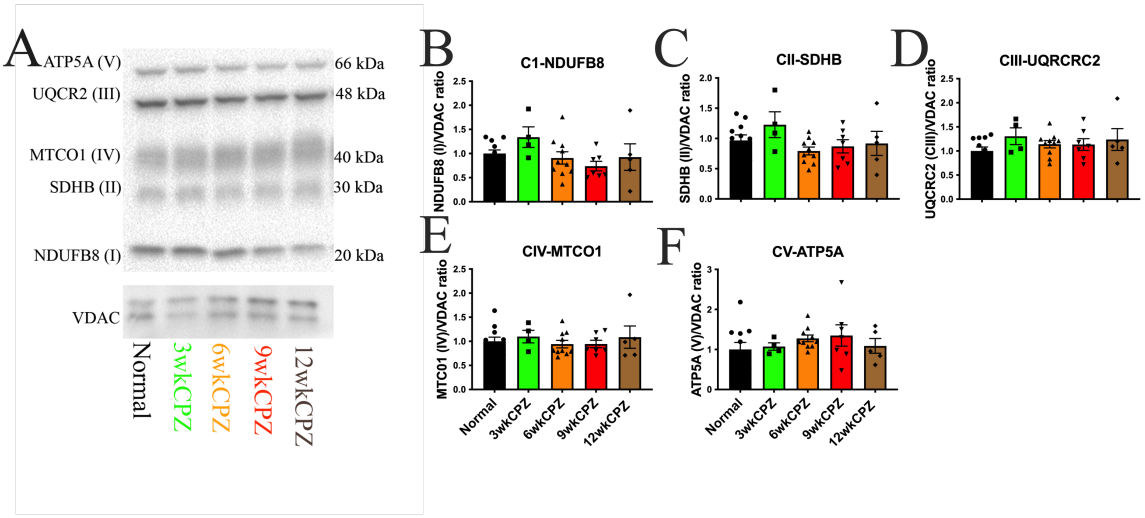

Figure 16: Cuprizone mice have no pathological changes in oxidative phosphorylation. (**A**) Representative blot of OXPHOS subunits including COXI (NDUFB8; 20 kDa), COXII (SDHB 30 kDa), COXIII (UQCR2, 48 kDa), COXIV (MTC01, 40 kDa), and ATP Synthase (ATP5A, 66 kDa) with VDAC used as a loading control. **(B-E)** There is no significant difference in COXI, COXII, or COXIII expression between 3wkCPZ, 6wkCPZ, 9wkCPZ, or 12wkCPZ and normal mice in the cerebellum. Normal: n=11, 3wkCPZ: n=4, 6wkCPZ: n=10, 9wkCPZ: n=7, 12wkCPZ: n=5. Data are represented as mean $\pm$ SEM. Statistical differences between groups were determined using two-tailed, unpaired *t* test.

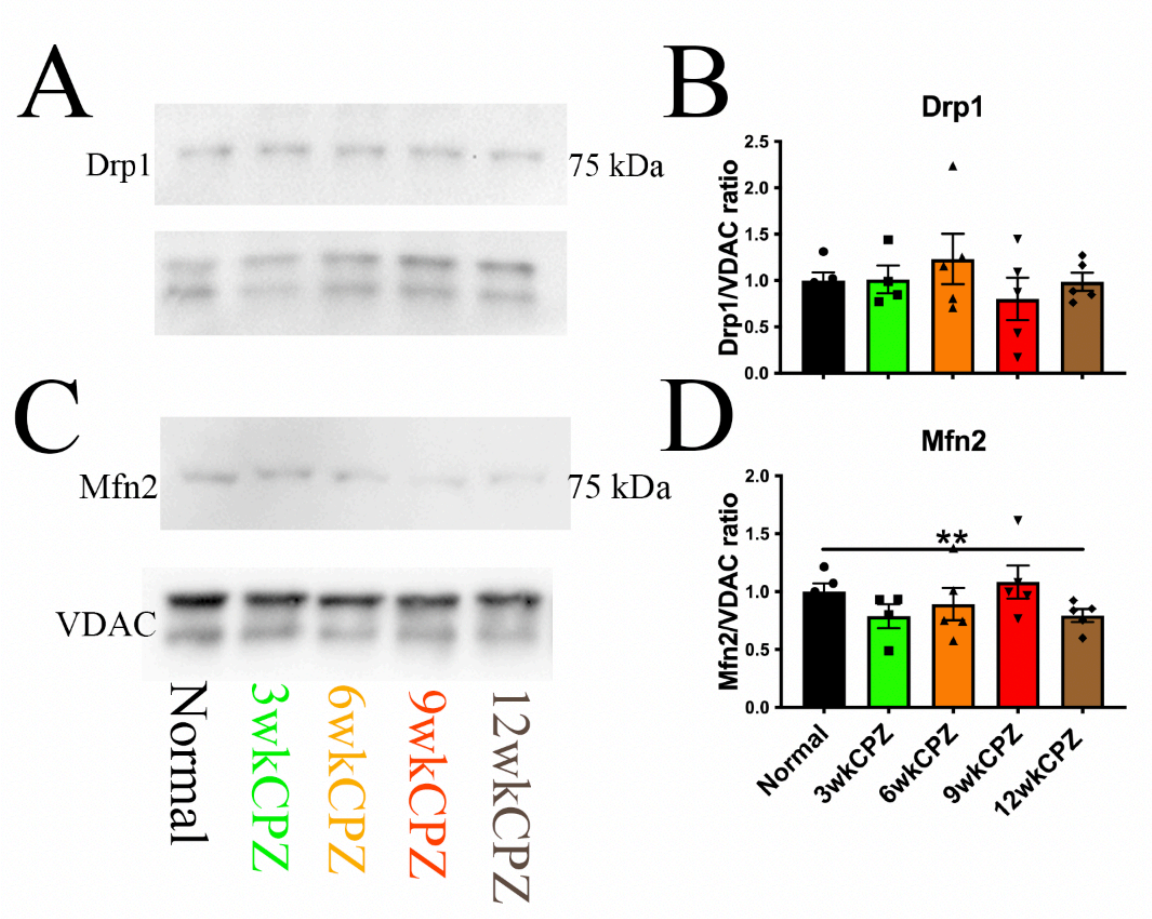

Figure 17: Cuprizone mice have decreased mitochondrial fusion at 12wkCPZ. (A) Representative blot of dynamin-related protein 1 (Drp1) with Normal, 3wkCPZ, 6wkCPZ, 9wkCPZ, and 12wkCPZ. **(B)** There was no difference in Drp1 expression between CPZ and normal mice. **(C)** Representative blot of mitofusin 2 (Mfn2) with Normal, 3wkCPZ, 6wkCPZ, 9wkCPZ, and 12wkCPZ. **(D)** There was a decrease in Mfn2 expression between the 12wkCPZ mice and normal mice. Normal: n=11, 3wkCPZ: n=4, 6wkCPZ: n=10, 9wkCPZ: n=7, 12wkCPZ: n=5. Data are represented as mean $\pm$ SEM. **p<0.01. Statistical differences between groups were determined using two-tailed, unpaired *t* test.

Chapter 5: ERβ ligand treatment alleviates mitochondria dysfunction in experimental autoimmune encephalomyelitis

Abstract

Approximately 80% of multiple sclerosis (MS) patients present with cerebellar symptoms consisting of tremors, impaired motor control and loss of coordination. The pathophysiology of these cerebellar symptoms is complex and remains to be fully elucidated. Therefore, there is a crucial need to understand the mechanism to yield important insights for potential MS treatments. Purkinje cells (PCs) are a class of myelinated neurons that are the sole output of the cerebellar cortex and thus are an essential component of cerebellar circuitry. These specialized cells demand higher metabolic activity due to their extensively branched dendritic arbors in addition to the large number of glutamatergic inputs they receive from climbing and parallel fiber innervation. Aberrant function and loss of PCs has been observed in MS and animal models of MS, including experimental autoimmune encephalomyelitis (EAE). Additionally, oligodendrocyte (OL) loss during demyelination reduces metabolic support of axons, leading to axonal mitochondrial dysfunction and subsequent neurodegeneration. Thus, we propose that EAE-induced OL loss leads to mitochondrial dysfunction in PCs which can be rescued with targeted estrogen receptor (ER) β ligand treatment. This hypothesis evaluated the status of PCs and PC mitochondria during EAE-induced inflammatory demyelination. In addition, the therapeutic effect of an ERβ ligand, IndCl-*o*-Me, previously shown to stimulate myelination and neuroprotection, as well as resveratrol (RSV), a phytoalexin that stimulates mitochondrial biogenesis, were evaluated. Our preliminary results demonstrate extensive cerebellar inflammation, demyelination, reduction of mature OLs, and changes in PC morphology in day 40 EAE-induced C57BL/6 male Thy1-YFP transgenic mice.

IndCl-*o*-Me-treated EAE mice revealed an increase in myelinated axons with decreased inflammation in cerebellar brain sections as compared to vehicle-treated mice. However, RSV-treated mice showed no change in axon myelination or inflammation. To assess mitochondrial status, sections were immunostained with i) translocator protein (TSPO), a component of mitochondrial bioenergetics, and ii) Complex IV, one subunit of the Cytochrome C Oxidase (COX) hetero-oligomeric enzyme located in the inner mitochondrial membrane. An increase in TSPO and COX expression was observed during EAE, consistent with previous studies. Interestingly, IndCl-*o*-Me treatment reduced both proteins, whereas, RSV treatment only decreased TSPO levels. IndCl-*o*-Me treatment appears to affect mitochondria expression and bioenergetics, however whether this occurs directly or indirectly remains to be elucidated. Future experiments will investigate in detail the timing, structural changes, and function of PC mitochondria in the presence of these drugs.

Introduction

Due to the fact that PPMS and SPMS patients exhibit demyelination that correlates with earlier death (Weinshenker et al., 1991; Kutzelnigg et al., 2007), it is essential that the pathophysiology of multiple sclerosis is understood to slow neurodegeneration and to improve the quality of life in MS patients.

The goal of this study was to evaluate mitochondrial dynamics in the EAE mouse model and to determine whether treatment with ERβ ligands or RSV improved mitochondrial dynamics during demyelination, inflammation, and neurodegeneration with the EAE model of MS. Mitochondria are the major organelles involved in the synthesis of ATP in mammalian cells due to the presence of the components responsible for the maintenance of oxidative phosphorylation (Mink et al., 1981). The CNS has a high metabolic rate and consumes about 20% of oxygen at rest while only accounting for 2% of total body weight (Silver and Erecińska, 1998). We hypothesized that treatment with ERβ ligands will improve mitochondrial dynamics compared to the vehicle treatment. Indazole chloride (IndCl) and its analogues are unique, highly selective ERβ ligands that have been shown to increase myelination and neuroprotection in both EAE and cuprizone (CPZ) mouse models of MS (Moore et al., 2014; Khalaj et al., 2016; Karim et al., 2018; Karim et al., 2019). IndCl and its analogues not only improves clinical disease scores and rotarod performance, but also has been shown to improve corpus callosal (CC) axon conduction

(Moore et al., 2014; Karim et al., 2019), however its effects on mitochondria remain to be elucidated.

This study also used resveratrol (3,4'5-trihydroxystilbene; $C_{14}H_{12}O_{3;}$ RSV), a polyphenolic phytoalexin found in grapes, berries, peanuts, and wines (Jardim et al., 2018). Since RSV is known to modulate mitochondrial biogenesis, we wanted to determine if modulating mitochondrial biogenesis and mitochondrial dynamics is enough to increase myelination and be neuroprotective in the EAE model of MS (Bowers et al., 2000; Jardim et al., 2018).

Results

ERβ ligands, but not RSV treatment, decreases EAE severity and improves motor and gait dysfunction.

The purpose of this study was to determine whether ERβ ligand treatment improve mitochondrial dynamics compared to vehicle treatment. After EAE induction, mice were scored each day for clinical disease severity on a range from 0 to 5 (**Figure 18**). Mice demonstrated an onset of symptoms on Day8 and reached peak disease on Day18, when treatment began. The EAE+IndCl-*o*-Me group had decreased clinical disease scores compared to the EAE+Vehicle group. There was no difference in clinical disease severity scores between the EAE+Vehicle group and the EAE+RSV group.

EAE-induced demyelination and a decrease in OLs is alleviated by ERB ligand treatment, but not RSV treatment

To assess myelination in the cerebellum on EAE day40 after treatment with ERβ ligands, mice were perfused and brains were sectioned and immunostained for myelin basic protein (MBP). Representative cerebellar montages for MBP + DAPI comparing normal and EAE+Vehicle groups demonstrate decreased MBP expression in the EAE+Vehicle group compared to the normal group (**Figure 19A**). To analyze MBP expression, we focused on the white matter (WM) in cerebellar lobule IV/V indicated by the white dashed rectangle because this is where the myelinated axons, including PC axons, are leaving the cerebellar cortex (**Figure 19B**). Representative 20x images for

MBP and DAPI indicate decreased MBP expression in the EAE+Vehicle group compared to the normal group. The EAE+IndCl-*o*-Me had increased MBP expression compared to the EAE+Vehicle group, however there was no change in MBP expression in the EAE+RSV group compared to the EAE+Vehicle group (**Figure 19D**).

Next we assessed mature oligodendrocyte counts using adenomatous polyposis coli (CC1) in the WM (**Figure 19C**). There was a decrease in CC1+ cells in the EAE+Vehicle group compared to the normal group (**Figure 19E**). There was an increase in CC1+ cells in the EAE+IndCl-*o*-Me group compared to the EAE+Vehicle group; however, there was no significant difference in CC1+ cells in the EAE+RSV group compared to the EAE+IndCl-*o*-Me group, indicating that RSV has no effect on myelination and mature oligodendrocyte numbers.

ERβ ligand treatment decreases leukocytes

Next, we assessed leukocytes in the cerebellar white matter and granule cell layer using CD45 with 20x images of the WM and granule cell layer to determine the effects of ERβ ligand treatment and RSV treatment on inflammation (**Figure 20A**). At EAE D40, there was a significant increase in CD45 expression in the Vehicle-treated mice compared to the normal mice. ERβ ligand treatment decreased CD45+ expression in the WM and GCL compared to the vehicle treatment (**Figure 20B**). However, there was no significant difference in leukocyte infiltration between RSV and vehicle treatment.

Both ERβ ligand treatment and RSV treatment modulate mitochondrial dynamics

Lastly, we performed immunofluorescence to determine whether mitochondrial dynamics were affected after treatment with ERβ treatment and RSV treatment. To do this, we measured cytochrome C oxidase subunit 4 (COXIV), which is the last component of the electron transport chain that converts molecular oxygen to water. This marker is often used to measure mitochondrial activity. Representative 40X images are shown in **Figure 21A** showing the molecular layer and Purkinje cell layer of the cerebellar cortex. When counting puncta in both of these layers, there was a significant decrease in COXIV expression in the vehicle mice compared to normal mice (**Figure 21B**). ERβ ligand treatment increased the amount of COXIV puncta in this area compared to the vehicle treatment. When we assessed the number of puncta with the RSV treatment, we also observed an increase in puncta compared to the vehicle treatment.

The next step was to determine whether mitochondria movement was altered within the axons with syntaphilin, a mitochondrial anchoring protein (Ohno et al., 2014; Joshi et al., 2015; Zhou et al., 2016). When mitochondria express syntaphilin, the mitochondria are anchored to the microtubules and are unable to move along the axon to get to places of higher energetic need. Compared to the vehicle-treated mice, there was an increase in syntaphilin expression with RSV treatment and IndCl-*o*-Methyl treatment,

indicating that both this ERβ ligand and RSV modulate mitochondrial movement (**Figure 22**).

Discussion

The purpose of this study was to determine whether ERβ ligands would modulate mitochondrial dynamics in EAE: an inflammatory, demyelinating, degenerative animal model of MS. EAE is similar to MS in that it is a T cell-mediated inflammatory disease with lymphocyte infiltration, demyelination, and neurodegeneration (Guo et al., 2013; Eberle et al., 2015).

Our lab has previously found that IndCl and its analogues are selective ERβ ligands that reduce CNS inflammation, promote remyelination, and ameliorate clinical disease severity in both the EAE and cuprizone (CPZ) models of MS (Moore et al., 2014; Karim et al., 2018; Karim et al., 2019). The IndCl-*o*-Me and IndCl-*o*-Cl analogues have single substitutions to the phenol ring while retaining ERβ selectivity over ERα (Karim et al., 2019). We have previously demonstrated that treatment with either analogue improves motor function with the rotarod test, increases myelination and neuroprotection in the spinal cord and corpus callosum, and decreases pro-inflammatory cytokines (Karim et al., 2019). However, the effects of ERβ ligands on mitochondrial dynamics and function are not yet elucidated.

Interestingly, ERβ is expressed directly on mitochondria, indicating that our ERβ ligands could have a direct effect on mitochondrial biogenesis and function (Yang et al., 2004).

Recent studies have illustrated ERα and ERβ in mitochondria of various cell types where they bind mtDNA (Klinge, 2017). Since our ERβ ligands already have properties that we know act directly on astrocytes and oligodendrocytes (Tiwari-Woodruff et al., 2007; Karim et al., 2018), the idea that they may also act directly on mitochondria may partially explain the neuroprotective aspect of the treatment.

RSV is a polyphenol compound found in a variety of foods and beverages including red grapes, peanuts and red wine (Jang et al., 1997; Alarcon De La Lastra and Villegas, 2005; Das and Das, 2007; Csiszar, 2011). These effects are thought to be exerted via activation of sirtuin 1 (SIRT1), which prevents axonal degeneration (Borra et al., 2005). RSV is thought to act as an anti-inflammatory agent through its antioxidant properties and through inhibition of lipoxygenase and cyclo-oxygenase formation (Gautam and Jachak, 2009). This drug has also been discussed as neuroprotective through SIRT1 activation. Studies that have utilized RSV for cardiovascular studies suggested that RSV exerted a vasodilation effect by improving the function of endothelial cells along the inner wall of blood vessels (Nicholson et al., 2010). However, this finding could implicate enhanced tethering, rolling, and adhesion of circulating inflammatory cells across the blood-brain barrier, exacerbating CNS symptoms in MS (Rice et al., 2005). Another study found that mice treated with RSV in their chow had more severe clinical signs than the control group induced with EAE and exacerbated demyelination and inflammation (Sato et al., 2013). In addition, GlaxoSmithKline reported that the safety of a proprietary formulation

of RSV (SRT501) was questioned in a clinical trial for patients with multiple myeloma (GlaxoSmithKline halts all further development of resveratrol drug SRT501 (The Myeloma Beacon 2010 Nov 30 [Internet])). Several patients in this trial experienced kidney failure, although it is unclear whether the kidney failure is due to SRT501 treatment or was a natural consequence of the disease.

However, there are other studies that show implications for RSV slowing disease in animal models of MS (Pallàs et al., 2013). RSV has been shown alter pro-inflammatory cytokine production (Singh et al., 2007). In addition, RSV-treated mice induced with EAE had lower clinical scores compared to control (Singh et al., 2007; Imler Jr and Petro, 2009). Other studies found that a high dose of RSV (250mg/kg/day) delayed the onset of EAE, but a low dose of RSV (100mg/kg/day) had no effect (Fonseca-Kelly et al., 2012). Interestingly, RSV treatment protected from RGC loss (Fonseca-Kelly et al., 2012), protected blood-brain barrier (BBB) integrity in EAE mice (Wang et al., 2016), inhibited neurodegeneration, and promoted neurogenesis and neuronal SIRT1 (Shindler et al., 2007; Shindler et al., 2010). Improved remyelination has also been demonstrated in the cuprizone model with RSV treatment (Ghaiad et al., 2017).

Studies suggest that RSV protects mice from EAE by inducing aryl hydrocarbon (AhR) and ER-mediated apoptosis, primarily in activated T cells (Singh et al., 2007). This finding could mean that treatment with both an ERβ ligand and RSV could be deleterious

to mice. The drug Laquinimod, currently under investigation for treatment of MS and other neuroinflammatory diseases, prevented development of EAE and was dependent on the AhR, as the protective effects were abolished in AhR knockout mice (Berg et al., 2016).

RSV treatment is thought to increase mitochondrial biogenesis, which is a complex process responsible for the synthesis of new mitochondria in mammalian cells (Borra et al., 2005). Both nuclear and mitochondrial genomes are necessary to modulate mitochondrial biogenesis (Pallàs et al., 2013). Peroxisome proliferator-activated receptor gamma coactivator 1-alpha (PGC-1alpha) is the major regulator in mitochondrial biogenesis by acting with the nuclear respiratory factors 1 and 2 (NRF-1 and NRF-2). PGC-1alpha upregulates NRF-1 and NRF-2, as well as the estrogen-related receptor alpha (ERRα), leading to the expression of mitochondrial proteins encoded by nuclear DNA (Lagouge et al., 2006; Witte et al., 2013). One of these proteins encoded by nuclear DNA is mitochondrial transcription factor A (TFAM), which leads to alternations in mitochondrial DNA (mtDNA) and causes synthesis of mitochondrial RNA. TFAM is involved with both transcription and replication of mtDNA.

Overall, our ERβ ligand treatment could demonstrate neuroprotection by modulating mitochondrial activity and transport in neurons. Assessing mitochondrial dynamics in specific cell types through the Cre-loxP system or cell sorting may provide a more

thorough investigation on mitochondrial changes in the context of demyelinating disease and treatment.

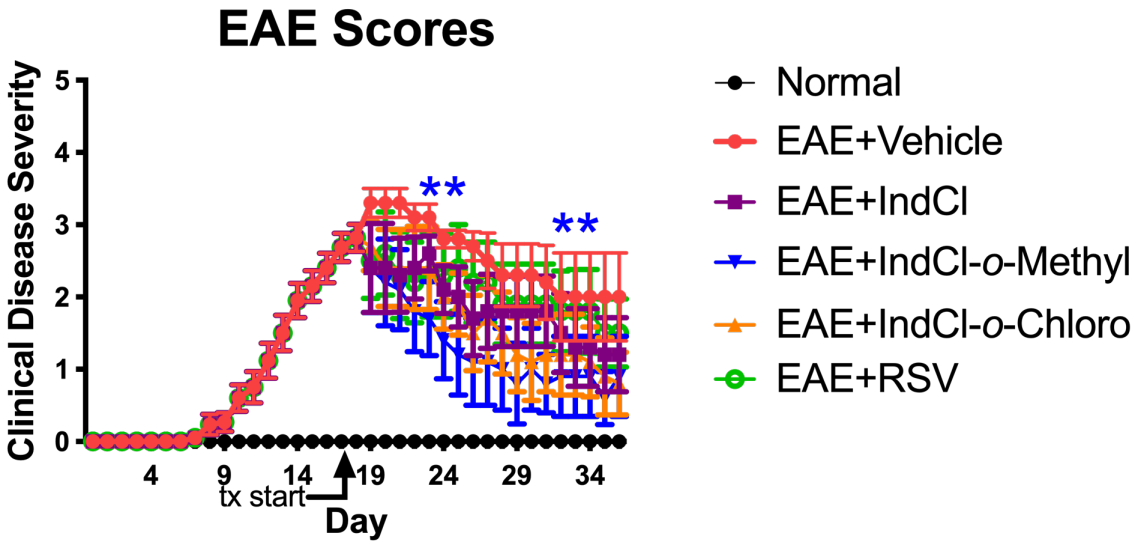

Figure 18: ERβ ligand treatment, but not resveratrol treatment, rescues clinical disease severity. Mice were induced with experimental autoimmune encephalomyelitis (EAE) and began to show clinical disease severity at EAE Day8. Mice reached a peak disease at around EAE D18 when treatment started. There was a significant decrease in clinical disease severity between the IndCl-*o*-Methyl-treated mice and the vehicle-treated mice. However, there was no difference between the RSV-treated mice and the vehicle-treated mice. Normal: n=5, EAE+Vehicle: 5, EAE+IndCl: 5, EAE+IndCl-o-Methyl: 5, EAE+IndCl-o-Chloro: 5, EAE+RSV: 5. Data are represented as mean ± SEM. **p<0.01. Statistical differences between groups were determined using two-way unbalanced ANOVA with Dunnetts multiple comparisons test.

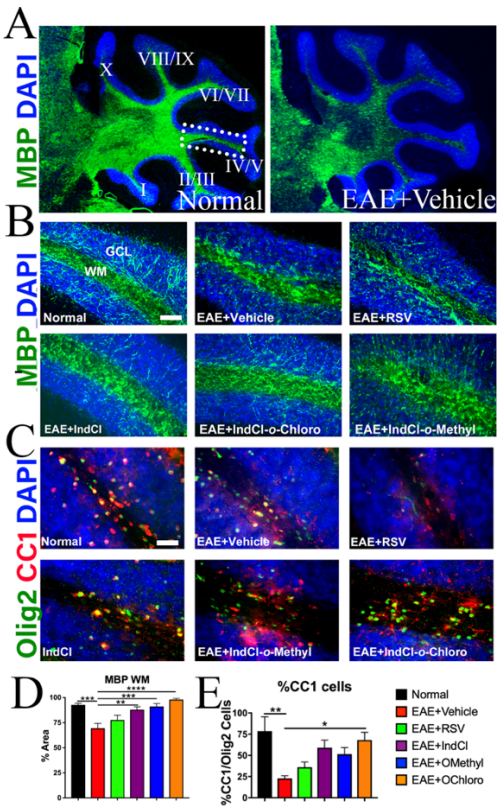

Figure 19: ERβ ligand treatment, but not resveratrol treatment, preserves myelination and mature oligodendrocytes in the white matter of the cerebellum. (A) 10X montages showing myelin basic protein (MBP; green) with DAPI. Visually there is a decrease in MBP expression in the EAE+Vehicle mice compared to the normal mice. **(B)** 20X representative images of cerebellar lobule IV/V showing MBP with DAPI. **(C)** 40X representative images of cerebellar lobule IV/V with Olig2 (green), adematous polyposis coli (CC1; red), and DAPI. **(D)** There is a decrease in MBP expression in the white matter (WM) in the EAE+Vehicle mice compared to the normal mice. In addition, there is an increase in MBP expression with treatment with ERβ ligands compared to vehicle treatment. There was no difference in MBP expression between RSV treatment and vehicle treatment. (**E**) There is a decrease in percentage of CC1 cells with vehicle treatment compared to normal treatment. There was a significant increase in CC1 cells with IndCl-o-Chloro treatment compared to vehicle treatment. There was no difference in percentage of CC1 cells between RSV treatment and vehicle treatment. Normal: n=5, EAE+Vehicle: 5, EAE+IndCl: 5, EAE+IndCl-o-Methyl: 5, EAE+IndCl-o-Chloro: 5, EAE+RSV: 5. Data are represented as mean ± SEM. Statistical differences between groups were determined using ordinary one-way ANOVA using Kruskal-Wallis multiple comparison test. *p<0.05, **p<0.01, ***p<0.001, ****p<0.0001. Scale bars: 100µm, 50µm.

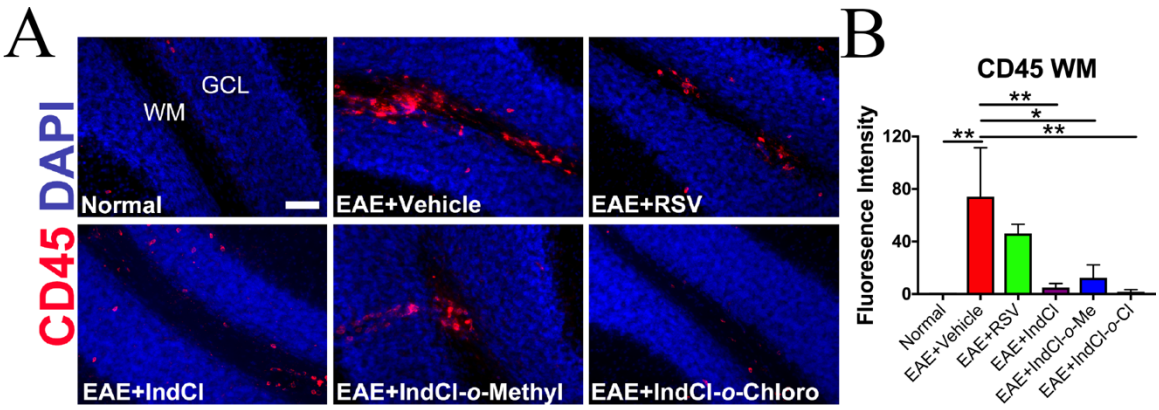

Figure 20: ERβ ligand treatment, but not RSV treatment, decreases leukocytes in the cerebellum. (A) 20X representative images showing CD45 (red) with DAPI (blue). **(B)** There is an increase in CD45 expression in the EAE+Vehicle mice compared to the normal mice. In addition, ERβ ligand treatment decreased CD45 expression compared to vehicle treatment, but not RSV treatment. Normal: n=5, EAE+Vehicle: 5, EAE+IndCl: 5, EAE+IndCl-o-Methyl: 5, EAE+IndCl-o-Chloro: 5, EAE+RSV: 5. Data are represented as mean ± SEM. Statistical differences between groups were determined using ordinary one-way ANOVA using Kruskal-Wallis multiple comparison test. *p<0.05, **p<0.01. Scale bar: 100µm.

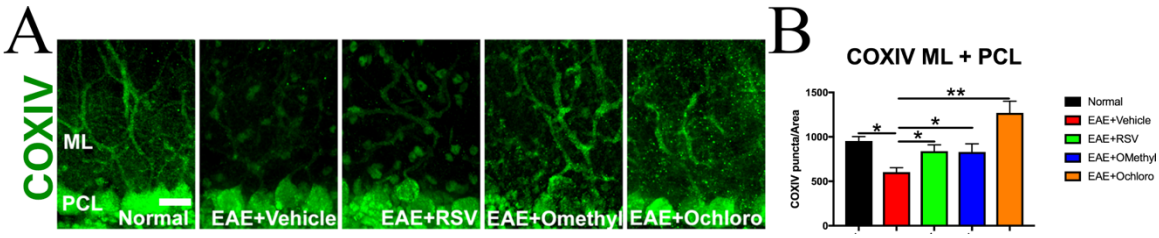

Figure 21: ERβ ligand treatment and resveratrol treatment increase COXIV expression in the molecular layer and Purkinje cell layer in the cerebellum. (A) 40X representative images showing cytochrome c oxidase subunit 4 (COXIV; green). **(B)** There is a decrease in COXIV puncta expression with the EAE+Vehicle mice compared to the normal mice. In addition, there is an increase in COXIV expression with treatment with both ERβ ligands and RSV compared to vehicle treatment. Normal: n=5, EAE+Vehicle: 5, EAE+IndCl: 5, EAE+IndCl-o-Methyl: 5, EAE+IndCl-o-Chloro: 5, EAE+RSV: 5. Data are represented as mean $\pm$ SEM. Statistical differences between groups were determined using ordinary one-way ANOVA using Kruskal-Wallis multiple comparison test. *$p<0.05$, **$p<0.01$. Scale bar: 50µm.

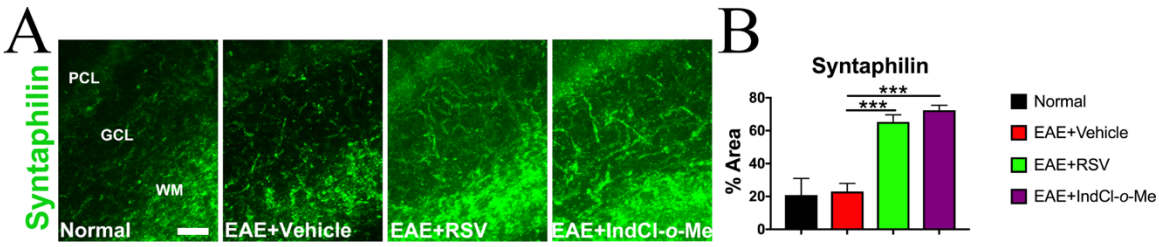

Figure 22: ERβ ligand IndCl-*o*-Methyl modulates mitochondrial movement. (A) 40X representative images syntaphilin (green) in the granule cell layer of the cerebellar cortex. **(B)** There is an increase in syntaphilin expression with both RSV treatment and IndCl-*o*-Methyl treatment compared to vehicle treatment. Normal: n=5, EAE+Vehicle: 5, EAE+IndCl: 5, EAE+IndCl-o-Methyl: 5, EAE+IndCl-o-Chloro: 5, EAE+RSV: 5. Data are represented as mean ± SEM. Statistical differences between groups were determined using ordinary one-way ANOVA using Kruskal-Wallis multiple comparison test. ***$p<0.001$. Scale bar: 50µm.

Chapter 6: Diffusion tensor imaging identifies aspects of therapeutic estrogen receptor β ligand-induced remyelination in a mouse model of multiple sclerosis

A version of this chapter is published in Proceedings of the National Academy of Sciences of the United States of America

Atkinson, K.C. *et al.* Diffusion tensor imaging identifies aspects of therapeutic estrogen receptor β ligand-induced remyelination in a mouse model of multiple sclerosis. *Neurobiology of Disease*. **130:104501**. (2019).

Abstract

Diffusion tensor imaging (DTI) has been shown to detect white matter degeneration in multiple sclerosis (MS), a neurodegenerative autoimmune disease that presents with diffuse demyelination of the central nervous system. However, the utility of DTI in evaluating therapeutic remyelination has not yet been well-established. Here, we assessed the ability of DTI to distinguish between remyelination and neuroprotection following estrogen receptor β ligand (Indazole chloride, IndCl) treatment, which has been previously shown to stimulate functional remyelination, in the cuprizone (CPZ) diet mouse model of MS. Adult C57BL/6J male and female mice received a normal diet (control), demyelination-inducing CPZ diet (9wkDM), or CPZ diet followed by two weeks of a normal diet (i.e., remyelination period) with either IndCl (RM+IndCl) or vehicle (RM+Veh) injections. We evaluated tissue microstructure of the corpus callosum utilizing *in vivo* and *ex vivo* DTI and immunohistochemistry (IHC) for validation. Compared to control mice, the 9wkDM group showed decreased fractional anisotropy (FA), increased radial diffusivity (RD), and no changes in axial diffusivity (AD) both in vivo and ex vivo. Meanwhile, RM+IndCl groups showed increased FA and decreased RD ex vivo compared to the RM+Veh group, in accordance with the evidence of remyelination by IHC. In conclusion, the DTI technology used in the present study can identify some changes in myelination and is a valuable translational tool for evaluating MS pathophysiology and therapeutic efficacy.

Introduction

Multiple sclerosis (MS) is an autoimmune, demyelinating, and neurodegenerative disease of the central nervous system (CNS) that affects about 2.3 million people worldwide(Browne et al., 2014). Due to widespread demyelination and axonal damage, MS patients exhibit a variety of symptoms, including problems with vision due to optic neuritis, motor deficits, and cognitive dysfunction. The gold standard for MS diagnosis is magnetic resonance imaging (MRI). The criterion is based on longitudinal detection of lesions with abnormalities in T1 and T2 hyperintensities over time (McDonald et al., 2001). Although MS-related pathology and MRI change can be seen anywhere in the CNS, conventional MRI cannot differentiate lesions that are due to demyelination and/or axonal damage. Diffusion tensor imaging (DTI), however, has revolutionized clinical neuroimaging by allowing for the detection of demyelination and axonal pathology earlier and with greater specificity than conventional MRI (Song et al., 2003). DTI examines water diffusion within the white matter tissue (i.e., the degree and direction of water diffusion along multiple axes) through tensor-model based reconstruction. This method provides valuable information regarding tissue microstructure, based on several metrics (Basser et al., 1994; Le Bihan et al., 2001; Mori and Zhang, 2006). Fractional anisotropy (FA) represents the asymmetry or directionality of water diffusion (FA=1, anisotropic diffusion; FA = 0, isotropic diffusion), while mean diffusivity (MD) examines the average magnitude of water diffusion within a voxel. Other metrics include axial diffusivity (AD, $\lambda\parallel$), which reflects water diffusion along the axon and measures axon integrity, whereas radial diffusivity (RD, $\lambda\perp$) reflects water diffusion perpendicular to

axons, thereby measuring myelin integrity. With such metrics, DTI has been effectively used to quantify demyelination and axonal loss in MS patients (Hesseltine et al., 2006; Klawiter et al., 2011; Elshafey et al., 2014; Ontaneda et al., 2014).

Current MS drugs, including interferon β, glatiramer acetate, and fingolimod, are immunomodulatory and do not directly stimulate remyelination or confer neuroprotection (Lopez-Diego and Weiner, 2008). Effective treatment options to initiate remyelination and prevent neurodegeneration are needed, as MS displays characteristics of a classical neurodegenerative disorder with damage to axons, synapses, and nerve cell bodies, along with rampant demyelination. The therapeutic efficacy of new MS treatments is usually tested in MS mouse models such as the experimental autoimmune encephalomyelitis (EAE) model, which incorporates key pathological components of MS (Lucchinetti et al., 2000; Baxter, 2007; Mangiardi et al., 2011b). However, the chronic cuprizone diet (CPZ) mouse model has been shown to be better suited for studying the progressive stage of MS with demyelination, axon damage, astrogliosis, and microglial activation(Matsushima and Morell, 2001; Kipp et al., 2009; Moore et al., 2014; Lapato et al., 2017). Further, this model is advantageous when evaluating disease progression and therapies that target such degeneration given its consistent demyelination in structures such as the corpus callosum (CC) and superior cerebellar peduncles (Matsushima and Morell, 2001; Kipp et al., 2009). Cuprizone diet for 6 weeks is sufficient for substantial demyelination. However, this timepoint demonstrates some variability resulting from an extensive attempt to remyelinate the CNS, which starts early, even before cuprizone exposure terminates,

confounding interpretation and drug-induced remyelination (Matsushima and Morell, 2001; Kipp et al., 2009). Thus, while cuprizone intoxication is inducing demyelination, oligodendrocyte progenitor cells (OPCs) are proliferating and differentiating to remyelinate axons during the 4–6 week cuprizone diet. By 9 week of cuprizone diet, there is near complete demyelination in the cortex, hippocampus, and CC and is an appropriate period to switch to normal diet to obtain clear axon remyelination for comparison with and without remyelinating drugs (Moore et al., 2014; Lapato et al., 2017).

Recently, estrogens have been evaluated for MS therapy due to their ability to stimulate myelination with neuroprotective benefits (Offner et al., 2000; Sicotte et al., 2002; Tiwari-Woodruff et al., 2007; Kumar et al., 2013; Moore et al., 2014; Karim et al., 2018; Karim et al., 2019). Due to estrogen receptor (ER) α-mediated feminization as well as increased risks of breast and uterine cancer, ERβ agonists have been considered more desirable therapeutic candidates (Lindberg et al., 2003). IndCl is a unique, highly selective ERβ ligand that induces accelerated, functional remyelination in both EAE and CPZ mouse models of MS (Moore et al., 2014; Khalaj et al., 2016; Karim et al., 2019). IndCl not only improves clinical disease scores and rotarod performance but also stimulates remyelination and neuroprotection in the chronic CPZ model, with improvements in CC axon conduction (Moore et al., 2014; Karim et al., 2019).

While progress has been made in the development of novel therapies for MS, DTI's utility in evaluating therapeutic remyelination has not been well-established yet could prove critical as DTI might serve as a valuable tool for the research and development of novel remyelinating agents like IndCl. For longitudinal monitoring of MS pathophysiology and potential therapeutic efficacy, *in vivo* DTI can be utilized. In turn, *ex vivo* DTI provides improved imaging resolution for the detection of more subtle changes in white matter microstructure due to longer acquisition times and elimination of *in vivo* brain pulsations and movement artifacts.

The goal of this study was to utilize *in vivo* and *ex vivo* DTI in evaluating remyelination and neuroprotection following IndCl treatment in the CPZ diet-induced demyelination/ remyelination model of MS. We hypothesized that DTI could adequately report CPZ-induced demyelination along with axonal damage as well as IndCl-induced therapeutic remyelination. This is the first study to evaluate the diagnostic potential of DTI with a remyelinating drug in an MS model. As such, it will serve as a first step towards longitudinal DTI assessment of white matter integrity in demyelinating MS models, which, combined with molecular and histological techniques, will streamline the screening process of therapeutic candidates and optimize the preclinical evaluation of their therapeutic potentials.

Results

Attempted in vivo quantitative DTI measures do not adequately reflect demyelination and remyelination

The initial goal of this study was to evaluate brain demyelination and remyelination in a mouse model of MS by *in vivo* DTI. Sex- and age- matched C57Bl/6 J mice were placed on a 0.2% CPZ diet for nine weeks to induce chronic demyelination (9wkDM). After nine weeks on a CPZ diet, a subset of these mice was switched to a normal diet for two weeks to induce remyelination and, concurrently, injected with a known functionally remyelinating ERβ ligand IndCl (RM + IndCl) or the vehicle (RM + Veh) (**Figure 23A**) (Moore et al., 2014). Because the CC is a major white matter tract that undergoes extensive demyelination during nine weeks on a CPZ diet, focused analysis of this commissural white matter tract of the left CC, center CC, and right CC was performed (**Figure 23B**).

FA is a coefficient that reflects the magnitude and orientation of anisotropic water diffusion and is highly sensitive to white matter microstructural integrity (Feldman et al., 2010). Representative group average maps for FA in control and 9wkDM groups are shown in Fig. 2A. Changes in vector colour intensity in regions such as the CC and cingulum were observed qualitatively between the groups as indicated by white arrows. ROIs for left CC, center CC and right CC (**Figure 24B**) were drawn manually and analyzed. Two-tailed, unpaired *t*-test with Welch's correction statistics were performed

comparing control (n= 5) with 9wkDM (n=6) and RM+Veh (n=5) with RM+IndCl (n=6). *In vivo* FA was decreased in the center and right CC of the 9wkDM group as compared to the control group (p = .25 left CC; p = .02 center CC; p = .002 right CC). However, no difference was observed between the RM+Veh and RM+IndCl groups (p=.89 left CC; p=.82 center CC; p = .60 right CC) (**Figure 24C**). To further assess differences in demyelination and remyelination between the groups, RD and AD were measured *in vivo*. RD represents the diffusion perpendicular to the main axial direction and is known to be altered in response to experimental demyelination and dysmyelination (Song et al., 2002; Song et al., 2005; Alexander et al., 2007). RD analysis showed an increase in the left and right CC of the 9wkDM group compared to the control group (p = .03 left CC, p = .69 center CC, p = .03 right CC) (**Figure 24D**). However, no difference in RD was observed between the RM+IndCl and RM+Veh groups (p=.83 left CC, p=.52 center CC, p=.51 right CC). AD is defined as the mean diffusion coefficient of water molecules diffusing parallel to the tract within the voxel (Song et al., 2003). Interestingly, *in vivo* AD in the CC did not differ between the control and 9wkDM groups or the RM+Veh and RM+IndCl groups (**Figure 24E**) (control *vs.* 9wkDM: p=.17 left CC, p=.52 center CC, p=.22 right CC; RM+Veh *vs.* RM + IndCl: p = .66, p = .24, p = .44). Overall, *in vivo* DTI showed minimal differences in demyelination between control and 9wkDM and no differences between RM+Veh and RM+IndCl.

Chronically demyelinated CC shows decreased fractional anisotropy (FA) and mean diffusivity (MD) by tract-based spatial statistics (TBSS)

To enhance white matter resolution, *ex vivo* DTI was performed on a separate cohort of animals (control: n = 6; 9wkDM: *n* = 8; RM + Veh: n = 8; RM + IndCl: n = 8) (**Figure 25**). Tract-based spatial statistics (TBSS) of the CC comparing the 9wkDM and control groups revealed that some CC regions in the 9wkDM group had lower FA (blue; **Figure 25A**). This was also apparent in three dimensional (3D) reconstructions of the TBSS (**Figure 25B**). FA revealed a decrease throughout the CC in the 9wkDM compared to the control group ($p = .0001$). However, no difference in FA TBSS was detected between the RM +Veh and RM+IndCl groups ($p = .53$) (**Figure 25B**). TBSS-based MD analysis showed increased MD (red) in the 9wkDM group compared to the control group, indicating fewer barriers and more isotropic diffusion (**Figure 25D**). 3D projection of these data illustrated that in the antero-lateral portion of the CC (red; **Figure 25E**). Indeed, there was an overall increase in MD in the 9wkDM group compared to the control group throughout the CC ($p=.002$). However, no difference was observed between the RM+Veh and RM+IndCl groups ($p = .21$) (**Figure 25F**). Overall, *ex vivo* DTI with TBSS analyses demonstrates changes in FA and MD in the chronically demyelinated CC.

Ex vivo DTI reveals corpus callosal changes in chronically demyelinated and IndCl-treated remyelinating groups

Since CPZ induces demyelination in distinct regions of the CC in a rostral to caudal fashion (Steelman et al., 2012; Schmidt et al., 2013), it is possible that remyelination events are differentially localized or below the detection threshold. Thus, assessment of local CC regions was performed by assigning ROIs (**Figure 26**). Based on the results of Fig. 3, an anterior section (Bregma 0.14/0.26mm) and a posterior section (Bregma −2.92/3.08mm) were analyzed. The CC was analyzed by tracing *ex vivo* ROIs for left CC, center CC, and right CC for anterior sections and for left CC and right CC for posterior sections as shown in **Figure 23B** and Supplementary Fig. S1. In anterior sections, the FA was reduced in the left, center, and right CC in the 9wkDM compared to the control group ($p < .0001$ left CC, $p = .02$ center CC, $p = .004$ right CC). In addition, the right CC FA was increased in the RM+IndCl group compared to the RM+Veh group ($p = .51$ left CC, $p = .30$ center CC, $p = .03$ right CC) (**Figure 26A**). The MD in these sections was not different between the control and 9wkDM groups throughout the CC ($p = .96$ left CC, $p = .33$ center CC, $p = .98$ right CC); however, the MD in the left CC of the RM + IndCl group was reduced compared to the RM+Veh group($p = .005$ left CC; $p = .09$ center CC, $p = .08$ right CC) (**Figure 26B**). No difference in FA ($p = .05$ left CC, $p = .20$ right CC) (**Figure 26C**) or MD (**Figure 26D**) was observed in the posterior section of 9wkDM and control groups ($p = .36$ left CC, $p = .13$ right CC). However, the left CC MD of the RM+IndCl group was decreased relative to the RM+Veh group ($p = .01$ left CC, $p = .22$ right CC). Because further imaging of posterior sections revealed fewer differences

(Supplementary Fig. S1), we chose to focus the remainder of our study on the anterior sections for *ex vivo* DTI.

IndCl treatment during the remyelination phase does not affect radial diffusivity (RD)

To further delineate microstructural myelin changes indicated by the FA, we assessed RD (**Figure 27**). *Ex vivo* TBSS for RD showed an increase in the 9wkDM group compared to the control group (red; **Figure 27A**). Statistical summary of RD TBSS revealed an increase throughout the CC of the 9wkDM group compared to the control group (**Figure 27B**). In contrast, RD quantification in the anterior section showed no difference in any region of the CC between the 9wkDM and control groups (p = .37 left CC, p = .19 center CC, p = .43 right CC) (**Figure 27C**). However, there was a decrease in *ex vivo* RD in the RM+IndCl group in the left and right CC compared to the RM+Veh group (p = .03 left CC, p = .39 center CC, p = .04 right CC).

IndCl treatment during the remyelination phase potentiates remyelination

Based on the anterior and posterior *ex vivo* DTI results, IHC was performed to understand and compare DTI results to CPZ-induced demyelination followed by normal diet-induced remyelination effects. IHC was performed at the level of the dorsal hippocampus between the anterior and posterior DTI Bregmas (**Figure 28**). To visualize changes in myelin, montages displaying myelin basic protein (MBP; green) and DAPI (blue) were imaged

with staining intensity analyzed. MBP intensity was decreased in the 9wkDM group compared to the control group, with a dramatic increase in MBP expression in the RM+IndCl group as compared to the RM+Veh group (**Figure 28A,B**). The center CC of the 9wkDM group showed a significant decrease in MBP intensity as compared to the control group (control *vs.* 9wkDM: $p < .0001$, **Figure 28C**). There was, however, a significant increase in MBP intensity in the RM+IndCl group compared to the RM+Veh group (RM+Veh *vs.* RM+IndCl $p < .0001$, **Figure 28C**). Similar changes were observed when the levels of another myelin protein, myelin oligodendrocyte glycoprotein (MOG) were measured (Supplementary Fig. S2). To further delineate changes in myelin organization, MBP coherency was quantified in the CC of anterior brain sections (**Figure 28D**). There was an increase in MBP coherency (more coherently organized myelin) throughout the CC of the 9wkDM group compared to the control group (control *vs* 9wkDM: $p = .0004$ left CC, $p = .001$ center CC, $p < .0001$ right CC). In addition, an increase in coherency was observed in the RM+IndCl group in the left CC compared to the RM+Veh group (RM+Veh *vs* RM+IndCl: $p = .04$ left CC, $p = .17$ center CC, $p = .14$ right CC). Overall, while IndCl treatment increased myelination by IHC analysis (similar to published results (Moore et al., 2014), DTI analysis demonstrated mixed results.

IndCl treatment during the remyelination phase minimally affects AD

Next, we assessed axonal integrity with AD (**Figure 29**). *Ex vivo* TBSS assessed in the CC showed qualitative increases in AD between the 9wkDM and control groups (the red

representing regions; **Figure 29A**). Quantification of images across the CC showed an increase in AD TBSS in the 9wkDM group compared to the control group (p = .03) (**Figure 29B**). However, there was no difference between the RM+Veh and RM+IndCl groups (p = .20). In contrast to the AD TBSS data, *ex vivo* analysis in the anterior sections displayed no significant differences between the 9wkDM and control groups (p = .27 left CC, p = .76 center CC, p = .41 right CC). There was an overall increase in *ex vivo* AD in the remyelinating groups. However, there was a decrease in AD in the RM+IndCl group compared to the RM+Veh group in the left and center CC (p=.003 left CC, p=.04 center CC, p=.51 right CC) (**Figure 29C**).

IndCl treatment during the remyelination phase decreases NF-M+ intensity

Changes in AD are associated with axonal damage and loss. To assess whether the few changes in AD correlated with pathology, brain sections were immunostained for SMI-32. An increase in non-phosphorylated neurofilament reactivity is seen during demyelination as myelin is stripped, exposing denuded axons. SMI-32 intensity was quantified in the center CC as indicated on a coronal brain section montage immunostained with SMI-32 and DAPI (**Figure 30A**). Representative 20× images for SMI-32 in the center CC are displayed in Fig. 8B. SMI-32 analysis showed increased SMI-32 expression in the 9wkDM group compared to the control group (p < .003) (**Figure 8C**). In addition, the RM+IndCl group showed decreased SMI-32 expression compared to the RM+Veh group (p < .03) (**Figure 8C**). Changes in axon pathology with

demyelination and remyelination were also confirmed by neurofilament M (NF-M) intensity analysis, an additional marker for axon damage (Supplementary Fig. S3).

Astrogliosis (glial fibrillary acidic protein; GFAP) and microglial activation (Iba-1) immunostaining were also performed to assess the extent of inflammation and glia activation. Similar to previous results (Moore et al., 2014), there was an increase in GFAP and Iba-1 immunoreactivity in the CC of the 9wkDM group compared to the control group (Supplementary Fig. S4). Remyelination did not modify GFAP and Iba-1 levels, and these were similar to the 9wkDM group levels. In summary, Table 1 summarizes the DTI and IHC results. Overall, aspects of DTI were representative of demyelination and remyelination pathology; however, DTI may not purely report all aspects of the histologically observed pathology.

Discussion

Mouse models are often used to model human white matter disease; however, rodents possess significantly less white matter than humans, so assessing disease progression in rodents using MR imaging can be difficult in the context of myelination (Zhang and Sejnowski, 2000). Out of the various MS mouse models, the CPZ model provides reliable and reproducible white matter pathology(Matsushima and Morell, 2001; Mangiardi et al., 2011b; Praet et al., 2014). The reproducibility of the CPZ model makes it well suited for studying mechanisms of demyelination and remyelination in the brain(Song et al., 2005; Xie et al., 2010; Yano et al., 2017), and for testing therapeutic treatments focused on improving axonal health and myelination.

In the present study, we included groups of mice that underwent CPZ-diet-induced chronic demyelination, followed by remyelination (initiated by switching to a normal diet) in the absence or presence of a known functionally remyelinating drug, IndCl. IndCl is a small, potent ERβ agonist with a 100:1 affinity for ERβ over ERα(De Angelis et al., 2005). IndCl has been previously shown to stimulate functional remyelination and neuroprotection by elevating neurotrophic factors and promoting oligodendrocyte survival and myelination through the PI3K/ Akt/mTOR pathway(Saijo et al., 2011; Moore et al., 2014). Furthermore, IndCl decreases pro-inflammatory IFNγ levels while enhancing chemokine CXCL1 levels, which can also potentially indirectly increase myelination (Karim et al., 2018; Karim et al., 2019).

The control, demyelinating (9wkCPZ) and remyelinating groups (9wkCPZ + 2wkND with vehicle or IndCl) were assessed by *in vivo* DTI, *ex vivo* DTI, and IHC to monitor changes in axon and myelin pathology (Moore et al., 2014; Karim et al., 2018). Here, for the first time, using DTI image analysis as an outcome, we were able to discriminate drug- induced remyelination changes.

Past published studies have shown conflicting data with *in vivo* DTI during demyelination. An increase in RD and a decrease in FA was observed in one study using 4wk CPZ diet (Yano et al., 2017), whereas a decrease in FA and no apparent change in RD was observed in another study using 6wk CPZ diet (Zhang et al., 2012). In our present study, *in vivo* DTI study showed a significant reduction in callosal FA during CPZ demyelination with no change in RD, which is in congruence with Zhang et al. (Zhang et al., 2012). However, in our hands, *in vivo* DTI analysis failed to detect white matter microstructural alteration following normal diet-induced remyelination in the presence of IndCl treatment. No difference in FA or RD between RM+Veh and RM+IndCl was observed. This lack of difference could be due to incomplete remyelination after chronic CPZ diet, producing thinner myelin that evaded DTI changes(Moore et al., 2014; Duncan et al., 2017).

Since changes were apparent with *in vivo* DTI between control and 9wkDM groups, but not between the RM+Veh and RM+IndCl groups, *ex vivo* DTI was initiated to further assess demyelination and remyelination differences in an additional experiment. Our *ex*

vivo TBSS data detected similar decreases to *in vivo* FA in the CC, as well as significant increases in MD in the 9wkDM group compared to the control group. However, no significant changes in RD were observed even with *ex vivo* DTI. Previous studies exhibited that the rostral CC is less susceptible to pathological changes in chronic CPZ compared to the middle and caudal CC, which is why we analyzed the caudal CC (anterior Bregma) by IHC (Wu et al., 2008; Xie et al., 2010; Steelman et al., 2012). Our 9wkDM group showed demyelination, axon damage, astrogliosis, and microglial activation similar to previous studies (Varga et al., 2018) . In addition, we observed a significant increase in coherency in MBP, indicating that MBP stained myelin was more coherently organized. Such results may reflect the altered organization of myelin due to the initial loss of myelin in the chronic demyelinated white matter. However, we saw no significant changes in SMI-32 coherency, which we interpret as surviving axons maintaining a similar orientation following demyelination.

Examination of specific CC regions in the remyelinating groups chosen based on *ex vivo* DTI TBSS data identified significant changes in FA and MD following RM+IndCl treatment as compared to RM+Veh alone. Such results signify not only that remyelination by IndCl was effective in altering white matter microstructure following experimental MS, but that only *ex vivo* data specific to the anterior regions of CC could detect these remyelination effects. Similar to previous results (Moore et al., 2014; Karim et al., 2019), the RM+IndCl group increased myelination and alleviated axon damage.

In essence, our study is one of the first to use DTI as a biomarker to evaluate CPZ-induced demyelination and remyelination with IndCl, an effective preclinical drug candidate. In the present *ex vivo* study, IndCl-treated mice showed a significant increase in FA compared to vehicle-treated mice. This result is expected due to increased anisotropy within the white matter voxels due to IndCl treatment-related stimulation of both remyelination and neuroprotection. These results also are in congruence with the significant decrease in RD observed *ex vivo* between the RM+IndCl and RM+Veh groups. However, the significant decrease in AD in the RM+IndCl group compared to the RM+Veh group was unexpected, because, as observed by IHC, IndCl decreased axon damage. However, it is important to note that DTI metrics do not match a single, specific physiological component. In fact, changes in axonal diameter, myelin distribution, axonal organization, intracellular compartments, and extracellular space can all contribute to changes in AD and overall DTI results (Zhang et al., 2012; Thiessen et al., 2013; Yano et al., 2017). Chronic demyelination changes are visible by *in vivo* and *ex vivo* DTI, but remyelination (induced with 3 week of normal diet) in the absence or presence of IndCl treatment produces thinner myelin around axons(Moore et al., 2014) as compared to myelinated axons in control mice. Thin myelin sheaths in the adult CNS are recognized as a marker of remyelination (shadow plaques in MS tissue (Popescu et al., 2013) and the mechanism driving the incomplete recovery remains unknown (Duncan et al., 2017). More sophisticated DTI measures using multi-shell sequence, alternative microstructure models beyond diffusion tensor, and diffusion kurtosis-DK) may be useful in teasing apart aspects of demyelination and remyelination. A recent study demonstrated that DKI-derived metrics are indeed sensitive to 6 week CPZ

induced demyelination and 3 week normal diet induced spontaneous remyelination of cortical areas (but not CC), thus high- lighting the potential of kurtosis for the detection of grey matter alterations (Guglielmetti et al., 2016). Recently, a study performed to assess performance of DKI and DTI parameters in detecting microstructural changes and associated pathology in relapsing remitting MS (RRMS) provided some interesting results. DTI-derived diffusion parameters (FA, MD, and RD) detected abnormality in white matter regions with coherent fiber arrangement; however, the kurtosis parameters (mean kurtosis, MK, axial kurtosis, Ka, and radial kurtosis, Kr) were able to discern abnormalities in white matter regions with complex fibers (Li et al., 2018).

Diffusion scalars provide only a weighted mean of the pathology observed by IHC. For example, there is extensive demyelination, inflammation, reactive astrocyte accumulation and axon damage in the CC of 9wkDM mice as compared to controls that are not singularly reflected in either of the AD, RD, and FA values for both *in vivo* and *ex vivo* conditions. Furthermore, many factors can influence DTI outcomes and introduce variability between measurements (*in vivo vs. ex vivo*). *Ex vivo* images were acquired at a higher field strength at 9.4 T as compared to *in vivo* acquisition at only 7 T. The higher b-values used for *ex vivo* have been reported to be more sensitive towards slow-diffusing intra-axonal and myelin bound water and thus more sensitive to microstructural alterations within the white matter (Yoshiura et al., 2003). Several other reasons, such as changes in tissue temperature and increased membrane permeability due to cell death and brain fixation for the *ex vivo* samples, could contribute to variation between *in vivo* and *ex vivo* results (Shepherd et al.,

2009). Finally, the diffusion time (Δ), which was adjusted to report optimal tissue diffusion in each condition, may play a role in producing the differences between *in vivo* and *ex vivo* data.

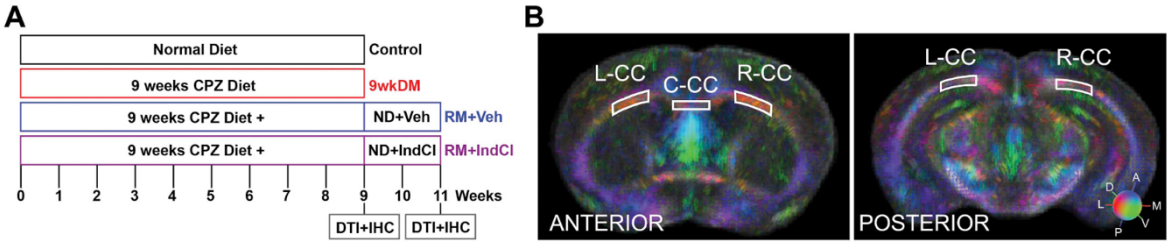

Figure 23. Experimental design. (A) Eight-week-old male and female mice were fed either a normal diet (control; n = 13) or nine weeks of a 0.2% cuprizone (CPZ) diet (9wkDM; n = 41). After nine weeks, 27 9wkDM mice were switched to a normal diet for two weeks and received daily injections of an estrogen receptor β ligand IndCl (RM+IndCl; n = 14) or the vehicle (RM+Veh; n = 13). Brains were collected for immunohistochemistry (IHC) following *in vivo* diffusion tensor imaging (DTI), which was performed at week eleven for the aforementioned groups and week nine for the control and 9wkDM groups. Another cohort of mice underwent *ex vivo* DTI followed by IHC at weeks eleven and nine. (B) Regions were interrogated for fractional anisotropy values. Images at the antero-posterior level from Bregma 0.14/0.26mm (anterior) and Bregma -2.92/3.08mm (posterior) were utilized for tissue-level region analysis, chosen based on tract based spatial statistics (TBSS) data. *Ex vivo* DTI primary diffusion vectors modulated by group average fractional anisotropy (FA) for control and 9wkDM groups are shown (red = medial-lateral [X], green = dorsal=ventral [Y], blue = anterior-posterior [Z]). The following regions of interest (ROI) were analyzed: left CC (L-CC), center CC (C-CC), and right CC (R-CC).

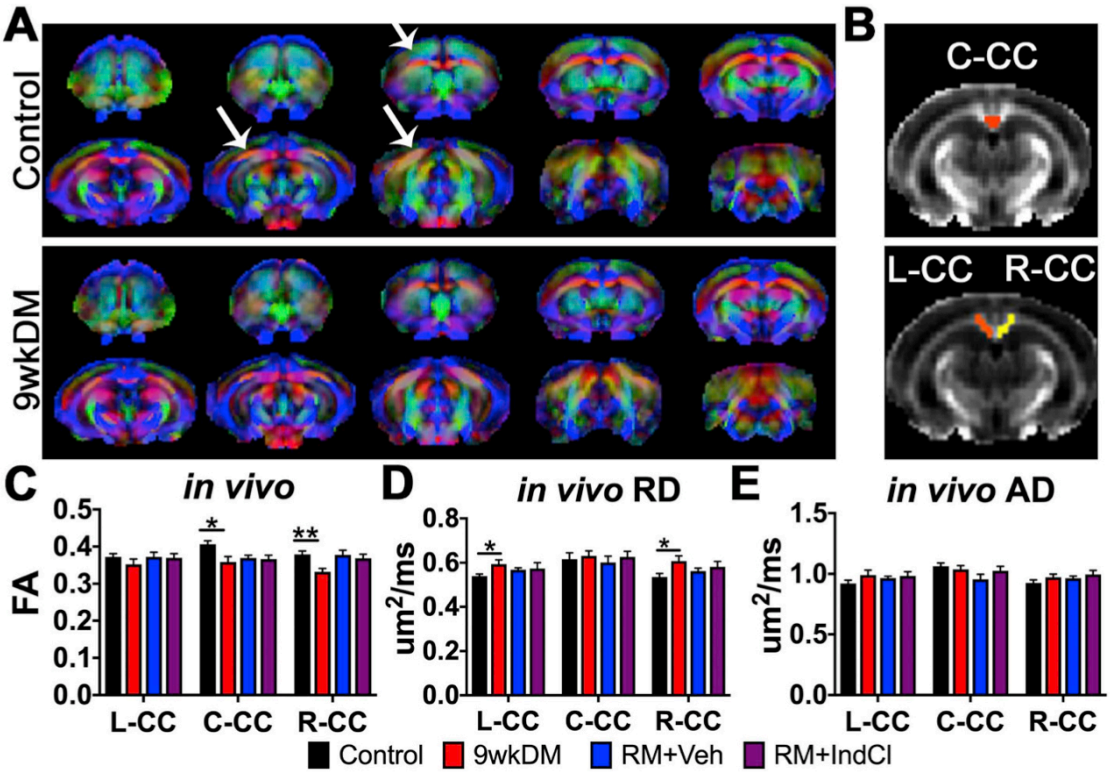

Figure 24. *In vivo* DTI detects CPZ-induced demyelination but not IndCl-induced remyelination. (A) *In vivo* primary diffusion vectors modulated by group average fractional anisotropy (FA) for control and 9wkDM groups (anterior to posterior sections from left to right, red = medial-lateral [X], green = dorsal-ventral [Y], blue = anterior-posterior [Z]). Diffusion data were warped to an anatomical template and used to calculate group averages. White arrows indicate areas that differ in FA between control and 9wkDM groups. (B) *In vivo* regions of interest for C-CC, L-CC, and R-CC were analyzed. (C) FA was decreased in the C- and R-CC of the 9wkDM compared to the control group. No differences in FA were detected between RM+Veh and RM+IndCl groups. (D) Radial diffusivity (RD) was increased in 9wkDM compared to the control groups in the L- and R-CC, while no differences in RD were observed between the RM+IndCl and RM+Veh groups. (E) No differences in axial diffusivity (AD) were observed between the control and 9wkDM groups, or between the RM+Veh and RM+IndCl groups. Control: n = 8; 9wkDM: n = 6; RM+Veh: N = 5; RM+IndCl: n = 6. Data are represented as mean ± SEM. Statistical differences between groups were determined using 2-tailed, unpaired t-tests with Welch's correction. *p < .05, **p < .01.

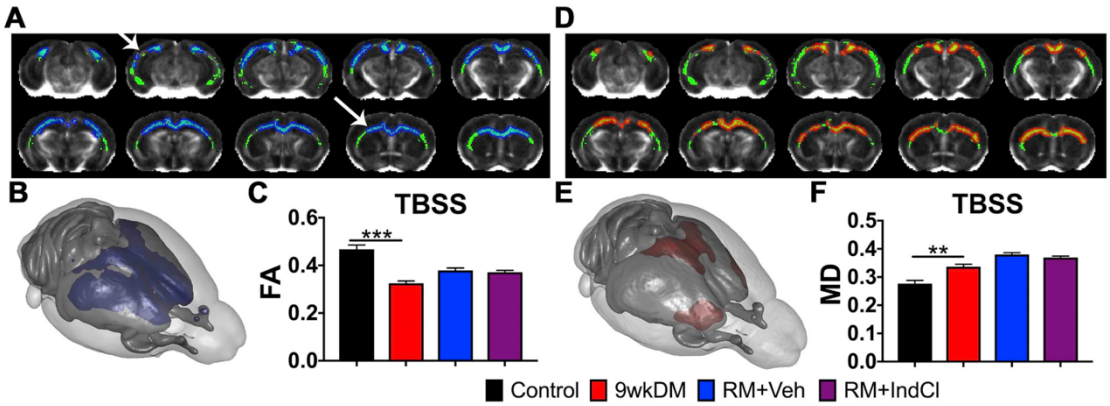

Figure 25. Chronic CPZ diet results in reduced *ex vivo* fractional anisotropy (FA), with no detectable differences between vehicle and IndCl-treated remyelination (RM) groups. (A) Tract-based spatial statistics (TBSS) of the CC comparing the control and 9wkDM groups (green: white matter skeleton; blue: significant decrease). (B) Three-dimensional projection of a mouse brain (purple: a significant decrease in the 9wkDM group compared to the control group). (C) FA was decreased throughout the CC of the 9wkDM group compared to the control group. (D) Mean diffusivity (MD) TBSS ($\mu m^2/ms$) within CC comparing the 9wkDM and control groups (green: white matter skeleton; red: significant increase). (E) Three-dimensional projection of a mouse brain (red: a significant increase in the 9wkDM group compared to the control group). (F) MD was increased in the 9wkDM group compared to the control group. Control: n = 6; 9wkDM: n = 8; RM+Veh: n = 8; RM+IndCl: n = 8. Data are represented as mean $\pm$ SEM. Statistical differences between groups were determined using 2-tailed, unpaired t-tests with Welch's correction. **p < .01, ***p < .001.

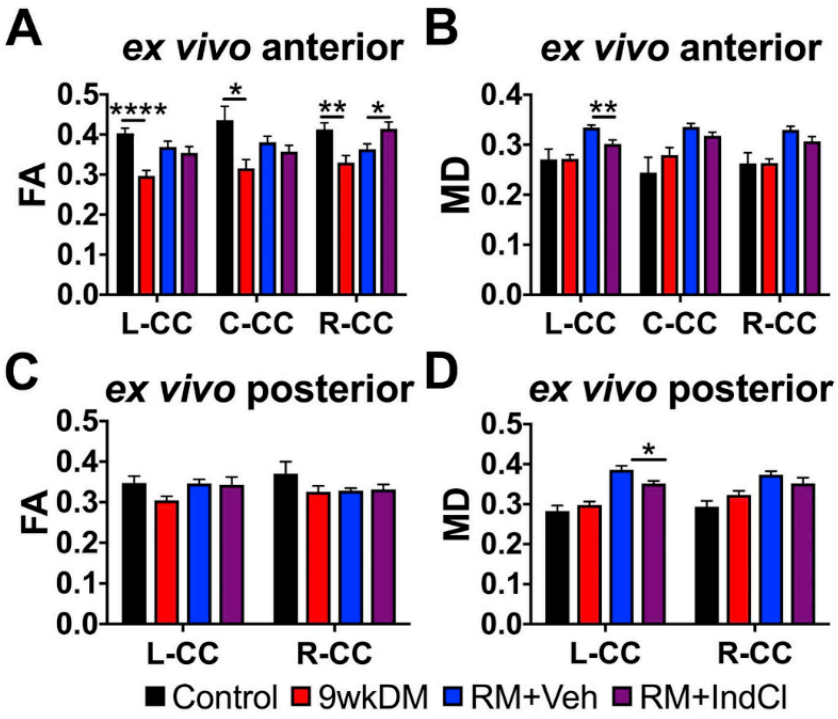

Figure 26. *Ex vivo* DTI reveals differences in corpus callosal (CC) fractional anisotropy (FA) and mean diffusivity (MD) of chronic CPZ versus control groups, and IndCl versus vehicle-treated remyelination (RM) groups. (A) FA in anterior sections was decreased in the L-CC, C-CC, and R-CC of the 9wkDM group compared to the control group. In addition, FA was increased in the R-CC of the RM+IndCl group compared to the RM+Veh group. (B) MD did not differ between the control and 9wkDM groups throughout the CC but was decreased in the L-CC of the RM+IndCl group compared to the RM+Veh group. (C) No differences in FA were detected in the posterior CC of the 9wkDM group compared to the control group, or between the RM+Veh and RM+IndCl groups. (D) No differences were observed in the MD in posterior CC between the control and 9wkDM groups. MD was decreased in the L-CC of the RM+IndCl group compared to the RM+Veh group. Control: n = 6; 9wkDM: n = 8; RM+Veh: n = 8; RM+IndCl: n = 8. Data are represented as mean ± SEM. Statistical differences between groups were determined using 2-tailed, unpaired t-tests with Welch's correction. *p<.05, **p < .01, ****p < .0001.

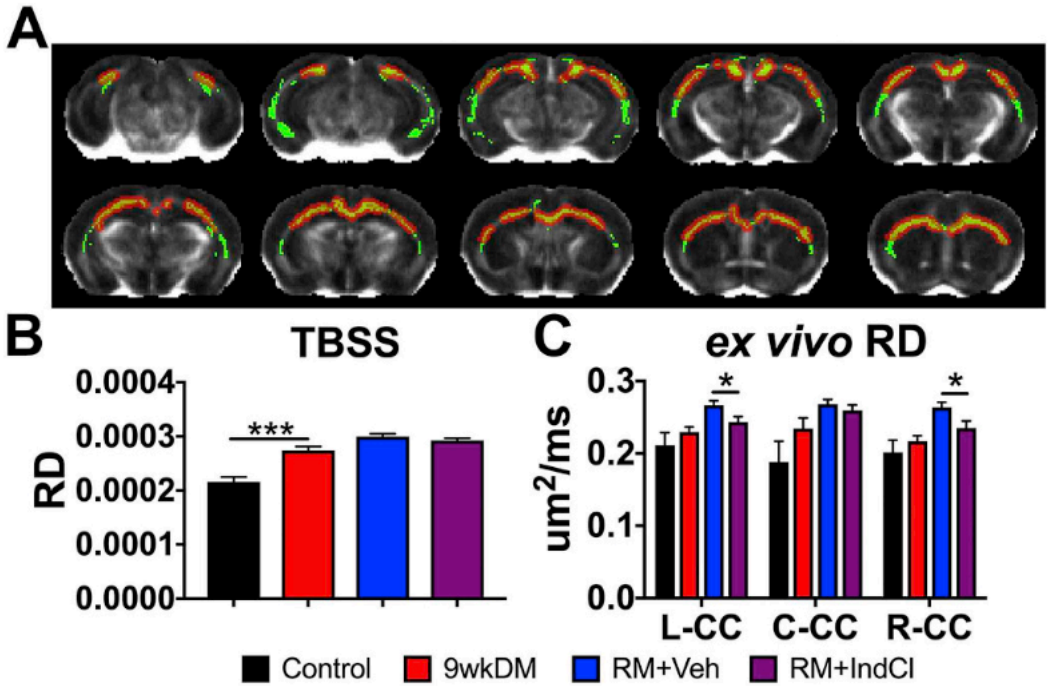

Figure 27. IndCl-treated remyelination group decreases *ex vivo* corpus callosal (CC) radial diffusivity (RD) compared to the vehicle-treated group. (A) Tract-based spatial statistics (TBSS) of the CC comparing the control and 9wkDM groups for RD (green: white matter skeleton; red: significant increase). (B) RD was increased throughout the CC of the 9wkDM group compared to the control group. (C) *Ex vivo* RD in anterior sections had no differences between control and 9wkDM. RD was decreased in the RM+IndCl group compared to the RM+Veh group in the left and right CC. Control: n = 6; 9wkDM: n = 8; RM+Veh: n = 8; RM+IndCl: n = 8. Data are represented as mean ± SEM. Statistical differences between groups were determined using 2-tailed, unpaired t-tests with Welch's correction. *p<.05, ***p < .001.

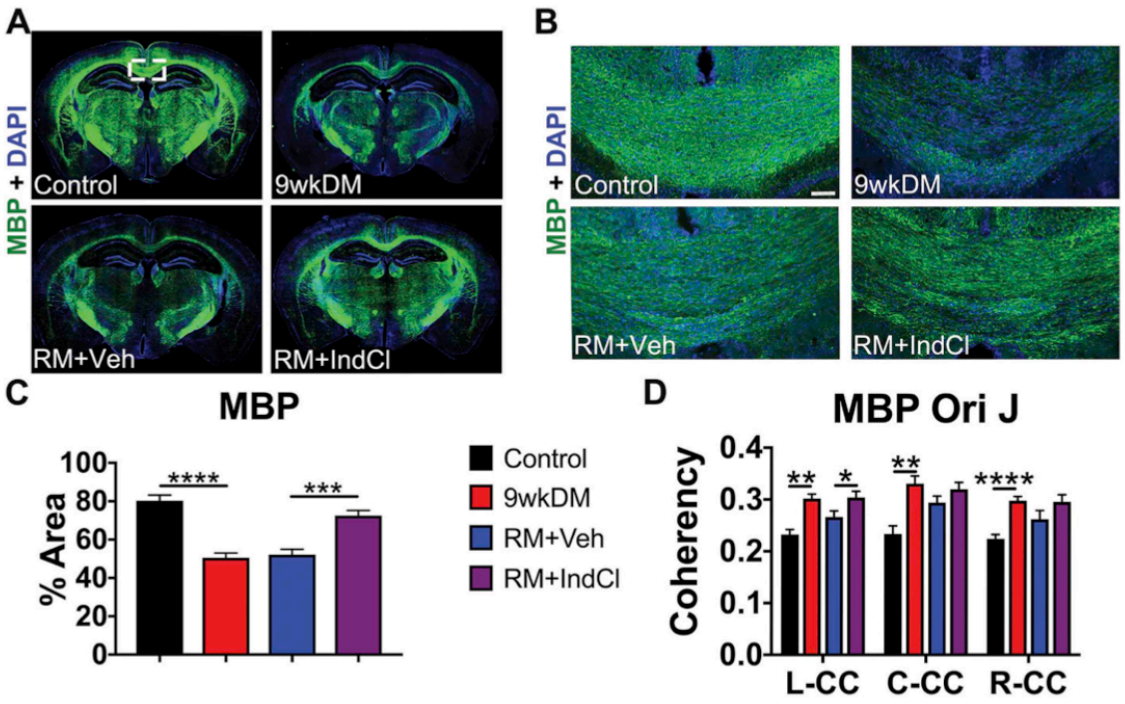

Figure 28. IndCl-treated remyelination group increases myelination. (A) 10X montages displaying coronal sections of myelin basic protein (MBP; green) + 4',6-diamidino-2-phenylindole (DAPI; blue). Representative montage of 9wkDM brain section shows a decrease in MBP staining intensity as compared to the control group. Whereas, RM+IndCl brain section shows an increase in staining intensity as compared to RM+Veh brain section. (B-C) Representative 10X images from the center CC from different groups immunostained with MBP show a similar result as in (A) and were used to quantify MBP intensity (scale bar = 50µm) shown in (C). (D) Analysis of MBP Orientation J (Ori J) in the L-, C-, and R-CC revealed an increase in the anterior sections of the 9wkDM group compared to the control group in the entire CC. However, the RM+IndCl group had an increase in MBP Ori J coherency compared to the RM+Veh group only in the left CC. Control: n = 6; 9wkDM: n = 8; RM+Veh: n = 8; RM+IndCl: n = 8. Data are represented as mean ± SEM. Statistical differences between groups were determined using 2-tailed, unpaired t-tests with Welch's correction. *p<.05, **p < .01, ****p < .0001.

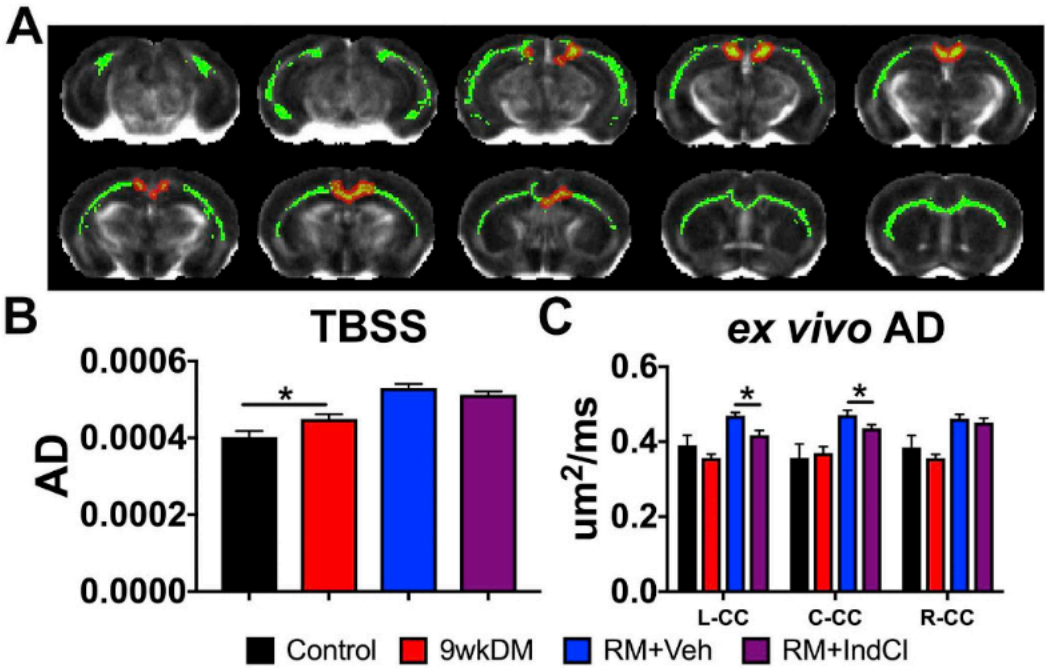

Figure 29. IndCl-treated remyelination group decreases *ex vivo* axial diffusivity (AD). (A) Tract-based spatial statistics (TBSS) of the CC comparing the control and 9wkDM groups for AD (green: white matter skeleton; red: significant increase). (B) AD was increased throughout the CC of the 9wkDM group compared to the control group. (C) *Ex vivo* AD in anterior sections showed no difference between the control group and 9wkDM group. AD was decreased in the RM+IndCl group compard to the RM+Veh group. Control: n = 6; 9wkDM: n = 8; RM+Veh: n = 8; RM+IndCl: n = 8. Data are represented as mean ± SEM. Statistical differences between groups were determined using 2-tailed, unpaired t-tests with Welch's correction. **p < .01, ***p < .001.

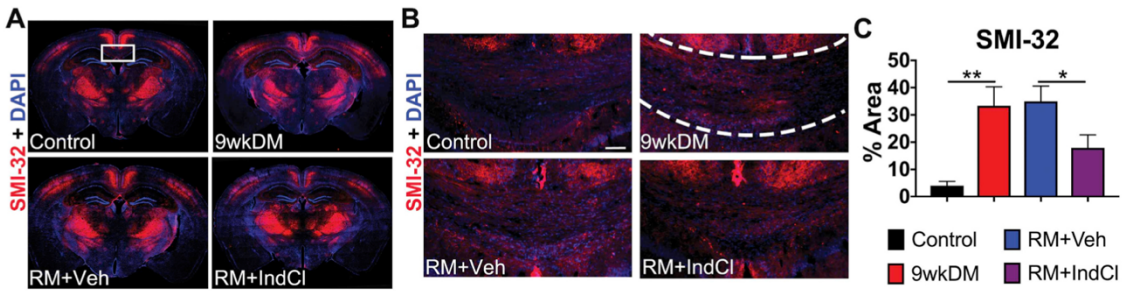

Figure 30. IndCl-treated remyelination group decreases non-phosphorylated neurofilament (SMI-32+) expression. (A) 10X montages displaying SMI-32 (red), a marker for axon damage, + 4',6-diamidino-2-phenylindole (DAPI; blue). The box represents 40X region where axon damage was imaged and analyzed in the C-CC. (B) 10X images for SMI-32 (red) + DAPI (blue). Scale bar = 50µm. (C) The 9wkDM group has more SMI-32 expression compared to the control group in the center CC. In addition, the RM+IndCl group had decreased SMI-32 expression compared to the RM+Veh group. Control: n = 6; 9wkDM: n = 8; RM+Veh: n = 8; RM+IndCl: n = 8. Data are represented as mean ± SEM. Statistical differences between groups were determined using 2-tailed, unpaired t-tests with Welch's correction. *p < .05.

Chapter 7: Discussion and Future Directions

Discussion

Two different models of MS, EAE and CPZ, were utilized to assess demyelination-induced changes in callosal axons by DTI and in mitochondrial health in white matter and Purkinje cells in the cerebellum. While EAE is a chronic mouse model of MS that incorporates demyelination, inflammation, and neurodegeneration, lesions occur throughout the CNS similar to MS, making direct comparison in groups of mice difficult but necessary. CPZ is a copper chelator that causes mature oligodendrocyte death in the brain, causing demyelination and neurodegeneration in a reproducible manner which allows a direct comparison within groups (Matsushima and Morell, 2001; Kipp et al., 2009).

MRI is currently used for the McDonald Diagnostic Criteria for MS (McDonald et al., 2001). While this technique is used to diagnose MS patients and is not invasive, MRI cannot differentiate myelin vs. axonal pathology in the CNS (Song et al., 2002). DTI is a better method to differentiate between myelin vs axonal pathologies due to differential water diffusion, thus identifying aspects of demyelination and remyelination (**Chapter 6**). Investigating advanced imaging methods in rodents has been complicated by the fact that mice have different scalings of gray and white matter compared to primates and humans (Ventura-Antunes et al., 2013). Because there is a larger fraction of neurons connected through WM in rodents, there is no clear distinction between white and gray matter. DTI utilization and comparison to humans with advanced imaging methods in

rodents does not translate well to clinical studies. Even though advancements have been made in the MS field with improved imaging and add-on MRI techniques to assess myelination, translation of these imaging methods have been difficult in diagnosing MS-related myelin changes unless the patients have high disability scores (Barile et al., 2021). The DTI study performed here was a collaboration with UCLA and Loma Linda and involved completion of the imaging DTI data and correlation to IHC. This project increased my knowledge of MS diagnosis and MRI imaging techniques and I learned about the difficulty in assessing demyelination and remyelination with imaging. During this time, I became interested in how larger neurons such as PCs in the cerebellum are affected during demyelination throughout the disease course. I was specifically interested in the energy demand of these cells and how it changes during disease and chose to focus on mitochondrial dynamics.

It is well known that demyelination contributes to diffusion of nodal and juxtaparanodal voltage-gated ion channels throughout the axon.(Dzhashiashvili et al., 2007; Susuki et al., 2013). This reorganization is thought to occur due to increased metabolic demand from the loss of saltatory conduction (Felts et al., 1997). When demyelination is paired with an autoimmune reaction, additional changes are occurring to the cellular milieu. Due to a broken BBB, macrophages are entering the CNS and releasing proinflammatory cytokines (e.g., IL-17, IL-4, IL-10, TNF-α) and reactive oxygen species (ROS) (Almolda et al., 2011; Jiang et al., 2012; Lassmann and van Horssen, 2016). Mitochondria are highly vulnerable to the action of ROS because it can interfere with the respiratory chain

(Lassmann and van Horssen, 2016). All of these changes are affecting mitochondria in neurons, oligodendrocytes, microglia, and astrocytes.

It is well known that neurons need mitochondria and ATP to maintain the resting membrane potential and for neurotransmission (Howarth et al., 2012; Friese et al., 2014). In addition, neurons do not have as many energy stores compared to other cells, such as astrocytes (Almeida et al., 2001; Saez et al., 2014). Oligodendrocytes not only utilize ATP, but also release lactate for the neuron as energy (Funfschilling et al., 2012; Lee et al., 2012; Philips and Rothstein, 2017). As oligodendrocytes collect lactate intracellularly, they can then transport them to the neuron through monocarboxylate transporter 1 (MCT1) into the neuron where they can metabolize it depending on their energy need (Funfschilling et al., 2012; Lee et al., 2012; Morrison et al., 2013). Astrocytes also utilize mitochondria for ATP; however, these cells have significant energy stores and can store glucose as glycogen (Almeida et al., 2001; Saez et al., 2014). Upon glutamate release from neurons, astrocytes can uptake glucose and convert glucose into pyruvate and lactate. Astrocytes can also shuttle metabolic substrates to neurons at the nodes of Ranvier through astrocytic MCT1 and MCT4 (Pellerin and Magistretti, 1994; Kasischke et al., 2004). Astrocyte-derived lactate has been shown to contribute to neuronal metabolism, but contact with neurons is generally limited to specific regions such as the soma, synaptic area, and nodes of Ranvier, whereas oligodendrocytes have extended contact with neurons through their myelin sheaths.

Microglia comprise of about 10% of total cells in the CNS and are the resident immune cells (Nimmerjahn et al., 2005; Salter and Stevens, 2017). Studies have shown that microglia and macrophages contribute to the pathogenesis of disease progression (Rawji and Yong, 2013; Chu et al., 2018). Under normal physiological conditions, there are few infiltrating macrophages into the CNS. However, when coupled with a compromised blood brain barrier (BBB), macrophages enter the CNS and release a combination of proinflammatory cytokines that further contribute to the inflammatory and degenerating milieu. Additional immune cells that could be contributing to neurodegeneration are the leukocytes that migrate into the CNS due to the compromised BBB. T cells require oxidative phosphorylation for Foxp3 transcription factor expression, differentiation, and anti-inflammatory IL-10 cytokine synthesis (Chávez and Tse, 2021). Microglia, the specialized brain macrophages, are known to require lots of energy to perform homeostatic functions. These cells primarily use glucose as the main source of metabolic fuel for oxidative phosphorylation (Vannucci et al., 1997; Wang et al., 2019; Lynch, 2020). *In vitro,* microglia have also been shown to adapt to the resources in their local environment by maintaining oxidative phosphorylation through other substrates, such as glutamine, lactate, pyruvate, and ketone bodies (Nagy et al., 2018). In addition, microglia have increased fission morphologically in the demyelinated cerebellar white matter (Katoh et al., 2017). Axon damage is a characteristic hallmark of EAE and MS. Some studies have shown focal axon degeneration (FAD) in the axon that is present before demyelination, likely due to reactive oxygen species (ROS) and reactive nitrogen species (RNS) released by macrophages (Nikic et al., 2011). Mitochondria are thought to

contribute to axon damage, as a microglia deficiency in peroxisome proliferator-activated-receptor-gamma (PPAR-γ), a nuclear receptor that increases metabolic homeostasis, contributes to exacerbated axonal injury in EAE (Doroshenko et al., 2021).

While there are several studies that have assessed mitochondrial changes in postmortem tissue (Dutta et al., 2006; Dutta et al., 2011), these studies only provide a picture of the pathology at that time. Still, mitochondrial changes are evident in MS postmortem tissue. One study observed increased mitochondria content (measured by porin) in chronic active MS lesions compared with myelinated axons. However, there was no difference in axonal mitochondrial content between remyelinated and demyelinated axons in remyelinated regions close to demyelinated areas in chronic MS lesions (Zambonin et al., 2011). Another study found respiratory deficient neurons that were prevalent within the dorsal root ganglia in progressive MS, noted as mitochondria that lacked COXIV but contained COXII (Licht-Mayer et al., 2020). These respiratory deficient neurons also had increased mitochondria content, size, and number (Licht-Mayer et al., 2020).

Decreased COXIV expression in pattern III MS lesions was observed in axons, astrocytes, and oligodendrocytes (Mahad et al., 2008). In addition, decreased COXIV activity was observed in axons in the rim of chronic active lesions, while axons within inactive lesions displayed increased activity of COXIV (Mahad et al., 2009). However, other studies have demonstrated increased mitochondrial activity. COXIV activity was

upregulated in MS lesions compared to control white matter and NAWM with an additional increase in mtHSP70, a mitochondrial stress protein (Witte et al., 2009). In addition, mitochondrial density in axons and astrocytes was increased in areas with active lesions compared to NAWM with a trend in inactive lesions. The variation in COXIV expression between the groups may be due to the type of lesions in both studies. Pattern III lesions are characterized by extensive oligodendrocyte apoptosis and hypoxia-like tissue injury (Lucchinetti et al., 2000). The MS postmortem tissue used in the study by Witte and colleagues did not have hypoxia-like damage or oligodendrocyte apoptosis. In addition, while Mahad and colleagues demonstrated an increase in COXIV activity in active lesions, they measured this particularly in axons, while Witte and colleagues measured COXIV activity in the entirety of the active lesion. Axonal COXIV activity may be overall decreased, but total COXIV activity in MS lesions may be increased. In addition to ETC changes, an upregulation of SNPH was observed in tissues from progressive MS patients compared to healthy patients (Mahad et al., 2009).

Conclusion

In the preceding work, the goal was to determine mitochondrial changes during the course of demyelinating disease. These studies were performed in two mouse models, EAE and CPZ. In the context of EAE, the inflammation aspect of the disease causes immune cell infiltration, astrocyte activation, and microgliosis, increasing mitochondrial activity in these cell types. However, this change is paired with the demyelination and

neurodegeneration aspect of this MS model, causing oligodendrocyte and neuronal death, decreasing mitochondrial activity. Even though there is little to no immune cell infiltration in the CPZ model, the microgliosis and astrocyte activation is still occurring in the presence of demyelination and neurodegeneration. Due to this, overall mitochondrial changes observed in both demyelinating models was subtle as the entire cerebellum was used for the mitochondrial pathological and functional studies. EAE (**Chapter 3**) showed an increase in coupled respiration at peak EAE disease (EAE D21) with the Seahorse Analyzer, decreased COXIV expression, and decreased Syntaphilin expression at chronic EAE (EAE D40 and EAE D60) with Western Blot. At peak disease when inflammation and demyelination are occurring, there is increased energy demand in the neurons. The decrease in coupled respiration may indicate that ATP Synthase may not be as functional, even when ADP is provided as a substrate. Eventually when the energy demand is not able to be met by the neurons and neurodegeneration occurs, there is a decrease in COXIV expression due to decreased mitochondria activity. The decreased syntaphilin may be a last effort from the neurons to allow the mitochondria to be transported to where they need to be within the axon before they degenerate; however, there may be too much axon damage by this point to allow the mitochondria to transport. Another reason why the changes are subtle could be due to the clinical disease score. In the longitudinal EAE Study (**Chapter 3**), the average EAE score for the mice used was a 2.5. This score is moderately sick for the mice and could be translated to an expanded disability status score in humans to a 4. Due to low disability score, the mice may have to

display a more severe clinical disease severity score of 3-4 to observe more aberrant mitochondrial changes in the cerebellum.

The CPZ model (**Chapter 4**) showed no changes except a decrease in mitochondrial fusion (Mfn2) at 12wkCPZ compared to normal. Mitochondrial fusion typically occurs when there is a decrease in energy demand, so not as much mitochondria are needed (Westermann et al., 2010). The decrease in mitochondrial fusion at 12wkCPZ compared to normal may be due to an increased energy need due to demyelination. When demyelination occurs, we would expect an increase in energy demand and an increase in fission. While we did not see changes in these, likely due to the other cell types in the cerebellum, the decrease in fusion may indicate that the mitochondria are doing the opposite of combining and are trying to scatter throughout the cells. Overall mitochondria in the WM (made up of mostly PC axons of demyelinating 9wkCPZ through EM) look much rounder and swollen, which some studies attribute to mitochondrial fusion (Luo et al., 2017). Similar swollen mitochondria through axons, have been depicted in previous studies with oligodendrocytes. To get a more in depth view on what is occurring with fission and fusion in both EAE and CPZ, 3D EM reconstruction could be performed to assess mitochondrial dynamics (Qi et al., 2006).

ERβ ligand treatment may directly act on mitochondria as a neuroprotective mechanism (Yang et al., 2004), in addition to these ligands' direct effects on oligodendrocytes and

astrocytes (Tiwari-Woodruff et al., 2007; Karim et al., 2018). Furthermore, ERβ is also expressed on neurons and immune cells, so this treatment may also act on mitochondria in all cell types. In Chapter 5, ERβ ligand treatment was able to show changes with COXIV expression in the molecular and Purkinje cell layers of the cerebellar cortex with immunofluorescence. In addition, there was an increase in Syntaphilin expression in the granule cell layer, which is where PC axons would leave the cerebellar cortex. Since these changes with ERβ treatment were observed around PCs, future directions should involve assessing Purkinje cell-specific mitochondrial changes.

As a summary, the changes in mitochondrial dynamics we see are:

- In EAE: Decreased coupled respiration at EAE D21, decreased COXIV expression at EAE D40 and EAE D60, and decreased syntaphilin expression at EAE D40 and EAE D60
- In CPZ: Decreased mitochondrial fusion at 12wkCPZ

Future Directions

Future studies assessing mitochondrial changes in the cerebellum should most importantly assess cell-specific changes. The experiments in this dissertation were performed with the entire cerebellum. While there were some changes observed, we are unable to conclude whether these mitochondrial changes are from neurons, glial cells, or

immune cells. PLP-eGFP mice are currently available at the Jackson Laboratory and express an enhanced green fluorescent protein under the PLP promoter. This line will allow for fluorescent activated cell sorting (FACs) to isolate PLP cells after demyelination to determine mitochondrial changes in PLP cells after EAE or CPZ diet. This technique can not only be performed on oligodendrocytes, but any cell that has a fluorescent probe attached.

Since ERβ ligand treatment showed benefits to mitochondrial dynamics in the cerebellar cortex, selectively deleting ERβ from PCs using the Purkinje Cell Protein 2 (PCP2) promoter will allow us to determine whether ERβ ligand treatment directly acts on PCs. While we know that ERβ ligands directly act on oligodendrocytes and astrocytes, we will be able to determine whether these effects are also directly beneficial to neurons.

Lastly, to be able to determine mitochondrial changes directly in PCs, PCP2-Cre mice can be crossed with MITO-tag mice to be able to see fluorescent, GFP-tagged mitochondria in PCs (Jackson #032290) (Bayraktar et al., 2019). In addition to assessing mitochondria morphology with fluorescence, GFP-tagged mitochondria also have the potential capability to be sorted as well for mitochondria-specific functional and pathological studies. All of these studies will further understand mitochondrial dynamics in the context of MS and MS mouse models. By understanding mitochondrial dynamics

in disease, we can build superior therapeutics and improve the quality of life for patients with MS.

References

Acs P, Komoly S (2012) Selective ultrastructural vulnerability in the cuprizone-induced experimental demyelination. Ideggyogyaszati szemle 65:266-270.

Alarcon De La Lastra C, Villegas I (2005) Resveratrol as an anti-inflammatory and anti-aging agent: Mechanisms and clinical implications. Molecular nutrition & food research 49:405-430.

Alexander AL, Lee JE, Lazar M, Field AS (2007) Diffusion tensor imaging of the brain. Neurotherapeutics 4:316-329.

Almeida A, Almeida J, Bolaños JP, Moncada S (2001) Different responses of astrocytes and neurons to nitric oxide: the role of glycolytically generated ATP in astrocyte protection. Proceedings of the National Academy of Sciences 98:15294-15299.

Almolda B, Gonzalez B, Castellano B (2011) Antigen presentation in EAE: role of microglia, macrophages and dendritic cells. Front Biosci 16:1157-1171.

Andrews H, White K, Thomson C, Edgar J, Bates D, Griffiths I, Turnbull D, Nichols P (2006) Increased axonal mitochondrial activity as an adaptation to myelin deficiency in the shiverer mouse. Journal of Neuroscience Research 83:1533-1539.

Apicco DJ, Shlevkov E, Nezich CL, Tran DT, Guilmette E, Nicholatos JW, Bantle CM, Chen Y, Glajch KE, Abraham NA (2021) The Parkinson's disease-associated gene ITPKB protects against α-synuclein aggregation by regulating ER-to-mitochondria calcium release. Proceedings of the National Academy of Sciences 118.

Atkinson KC, Lee JB, Hasselmann JP, Kim SH, Drew A, Soto J, Katzenellenbogen JA, Harris NG, Obenaus A, Tiwari-Woodruff SK (2019) Diffusion tensor imaging identifies aspects of therapeutic estrogen receptor β ligand-induced remyelination in a mouse model of multiple sclerosis. Neurobiology of disease 130:104501.

Atorino L, Silvestri L, Koppen M, Cassina L, Ballabio A, Marconi R, Langer T, Casari G (2003) Loss of m-AAA protease in mitochondria causes complex I deficiency and increased sensitivity to oxidative stress in hereditary spastic paraplegia. The Journal of cell biology 163:777-787.

Baker JM (2018) Gait disorders. The American journal of medicine 131:602-607.

Baloyannis SJ (2006) Mitochondrial alterations in Alzheimer's disease. Journal of Alzheimer's disease 9:119-126.

Barcelos IPd, Troxell RM, Graves JS (2019) Mitochondrial dysfunction and multiple sclerosis. Biology 8:37.

Barile B, Marzullo A, Stamile C, Durand-Dubief F, Sappey-Marinier D (2021) Ensemble Learning for Multiple Sclerosis Disability Estimation Using Brain Structural Connectivity. Brain Connectivity.

Barnett MH, Mathey E, Kiernan MC, Pollard JD (2016) Axonal damage in central and peripheral nervous system inflammatory demyelinating diseases: common and divergent pathways of tissue damage. Current Opinion in Neurology 29:213-221.

Basser PJ, Mattiello J, LeBihan D (1994) Estimation of the effective self-diffusion tensor from the NMR spin echo. Journal of Magnetic Resonance, Series B 103:247-254.

Baumann N, Pham-Dinh D (2001) Biology of oligodendrocyte and myelin in the mammalian central nervous system. Physiological Reviews 81:871-927.

Baxter AG (2007) The origin and application of experimental autoimmune encephalomyelitis. Nature Reviews Immunology 7:904.

Bayraktar EC, Baudrier L, Özerdem C, Lewis CA, Chan SH, Kunchok T, Abu-Remaileh M, Cangelosi AL, Sabatini DM, Birsoy K (2019) MITO-Tag Mice enable rapid isolation and multimodal profiling of mitochondria from specific cell types in vivo. Proceedings of the National Academy of Sciences 116:303-312.

Belenguer P, Duarte JM, Schuck PF, Ferreira GC (2019) Mitochondria and the brain: bioenergetics and beyond. Neurotoxicity research 36:219-238.

Berg J, Mahmoudjanlou Y, Duscha A, Massa MG, Thöne J, Esser C, Gold R, Haghikia A (2016) The immunomodulatory effect of laquinimod in CNS autoimmunity is mediated by the aryl hydrocarbon receptor. Journal of neuroimmunology 298:9-15.

Black JA, Dib-Hajj S, Baker D, Newcombe J, Cuzner ML, Waxman SG (2000) Sensory neuron-specific sodium channel SNS is abnormally expressed in the brains of mice with experimental allergic encephalomyelitis and humans with multiple sclerosis. Proceedings of the National Academy of Sciences 97:11598-11602.

Blakemore WF (1972) OBSERVATIONS ON OLIGODENDROCYTE DEGENERATION, RESOLUTION OF STATUS SPONGIOSUS AND REMYELINATION IN CUPRIZONE INTOXICATION IN MICE. Journal of Neurocytology 1:413-426.

Blokhin A, Vyshkina T, Komoly S, Kalman B (2008) Variations in mitochondrial DNA copy numbers in MS brains. Journal of Molecular Neuroscience 35:283-287.

Bordone MP, Salman MM, Titus HE, Amini E, Andersen JV, Chakraborti B, Diuba AV, Dubouskaya TG, Ehrke E, Espindola de Freitas A (2019) The energetic brain–A review from students to students. Journal of neurochemistry 151:139-165.

Borra MT, Smith BC, Denu JM (2005) Mechanism of human SIRT1 activation by resveratrol. Journal of Biological Chemistry 280:17187-17195.

Bossy-Wetzel E, Petrilli A, Knott AB (2008) Mutant huntingtin and mitochondrial dysfunction. Trends in neurosciences 31:609-616.

Bowers JL, Tyulmenkov VV, Jernigan SC, Klinge CM (2000) Resveratrol acts as a mixed agonist/antagonist for estrogen receptors α and β. Endocrinology 141:3657-3667.

Brady ST (1985) A NOVEL BRAIN ATPASE WITH PROPERTIES EXPECTED FOR THE FAST AXONAL-TRANSPORT MOTOR. Nature 317:73-75.

Broadwater L, Pandit A, Clements R, Azzam S, Vadnal J, Sulak M, Yong VW, Freeman EJ, Gregory RB, McDonough J (2011) Analysis of the mitochondrial proteome in multiple sclerosis cortex. Biochimica et Biophysica Acta (BBA)-Molecular Basis of Disease 1812:630-641.

Browne P, Chandraratna D, Angood C, Tremlett H, Baker C, Taylor BV, Thompson AJ (2014) ATLAS OF MULTIPLE SCLEROSIS 2013: A GROWING GLOBAL PROBLEM WITH WIDESPREAD INEQUITY. Neurology 83:1022-1024.

Budd SL, Nicholls DG (1998) Mitochondria in the life and death of neurons. Essays in biochemistry 33:43-52.

Campbell G, Mahad DJ (2018) Mitochondrial dysfunction and axon degeneration in progressive multiple sclerosis. FEBS letters 592:1113-1121.

Campbell GR, Mahad DJ (2011) Mitochondria as crucial players in demyelinated axons: lessons from neuropathology and experimental demyelination. Autoimmune diseases 2011.

Campbell GR, Ziabreva I, Reeve AK, Krishnan KJ, Reynolds R, Howell O, Lassmann H, Turnbull DM, Mahad DJ (2011) Mitochondrial DNA deletions and neurodegeneration in multiple sclerosis. Annals of neurology 69:481-492.

Caprariello AV, Rogers JA, Morgan ML, Hoghooghi V, Plemel JR, Koebel A, Tsutsui S, Dunn JF, Kotra LP, Ousman SS (2018) Biochemically altered myelin triggers autoimmune demyelination. Proceedings of the National Academy of Sciences 115:5528-5533.

Carter RJ, Lione LA, Humby T, Mangiarini L, Mahal A, Bates GP, Dunnett SB, Morton AJ (1999) Characterization of progressive motor deficits in mice transgenic for the human Huntington's disease mutation. Journal of Neuroscience 19:3248-3257.

Chan DC (2006) Mitochondria: dynamic organelles in disease, aging, and development. Cell 125:1241-1252.

Chang C-R, Manlandro CM, Arnoult D, Stadler J, Posey AE, Hill RB, Blackstone C (2010) A lethal de novo mutation in the middle domain of the dynamin-related GTPase Drp1 impairs higher order assembly and mitochondrial division. Journal of Biological Chemistry 285:32494-32503.

Chen H, Chan DC (2009) Mitochondrial dynamics–fusion, fission, movement, and mitophagy–in neurodegenerative diseases. Human molecular genetics 18:R169-R176.

Chen H, Vermulst M, Wang YE, Chomyn A, Prolla TA, McCaffery JM, Chan DC (2010) Mitochondrial fusion is required for mtDNA stability in skeletal muscle and tolerance of mtDNA mutations. Cell 141:280-289.

Chen J-Q, Cammarata PR, Baines CP, Yager JD (2009) Regulation of mitochondrial respiratory chain biogenesis by estrogens/estrogen receptors and physiological, pathological and pharmacological implications. Biochimica et Biophysica Acta (BBA)-Molecular Cell Research 1793:1540-1570.

Cheng A, Hou Y, Mattson MP (2010) Mitochondria and neuroplasticity. ASN neuro 2:AN20100019.

Chinopoulos C, Vajda S, Csanády L, Mándi M, Mathe K, Adam-Vizi V (2009) A novel kinetic assay of mitochondrial ATP-ADP exchange rate mediated by the ANT. Biophysical journal 96:2490-2504.

Chu F, Shi M, Zheng C, Shen D, Zhu J, Zheng X, Cui L (2018) The roles of macrophages and microglia in multiple sclerosis and experimental autoimmune encephalomyelitis. Journal of neuroimmunology 318:1-7.

Chudakov DM, Lukyanov S, Lukyanov KA (2007) Tracking intracellular protein movements using photoswitchable fluorescent proteins PS-CFP2 and Dendra2. Nature protocols 2:2024.

Chávez MD, Tse HM (2021) Targeting mitochondrial-derived reactive oxygen species in T cell-mediated autoimmune diseases. Frontiers in Immunology:2646.

Craner MJ, Lo AC, Black JA, Baker D, Newcombe J, Cuzner ML, Waxman SG (2003) Annexin II/p11 is up-regulated in Purkinje cells in EAE and MS. Neuroreport 14:555-558.

Crawford DK, Mangiardi M, Tiwari-Woodruff SK (2009) Assaying the functional effects of demyelination and remyelination: revisiting field potential recordings. J Neurosci Methods 182:25-33.

Csiszar A (2011) Anti-inflammatory effects of resveratrol: possible role in prevention of age-related cardiovascular disease. Annals of the New York Academy of Sciences 1215:117.

Das S, Das DK (2007) Anti-inflammatory responses of resveratrol. Inflammation & Allergy-Drug Targets (Formerly Current Drug Targets-Inflammation & Allergy)(Discontinued) 6:168-173.

De Angelis M, Stossi F, Carlson KA, Katzenellenbogen BS, Katzenellenbogen JA (2005) Indazole estrogens: Highly selective ligands for the estrogen receptor β. Journal of medicinal chemistry 48:1132-1144.

de Bruin N, Schmitz K, Schiffmann S, Tafferner N, Schmidt M, Jordan H, Häußler A, Tegeder I, Geisslinger G, Parnham M (2016) Multiple rodent models and behavioral measures reveal unexpected responses to FTY720 and DMF in experimental autoimmune encephalomyelitis. Behavioural brain research 300:160-174.

de Solages C, Szapiro G, Brunel N, Hakim V, Isope P, Buisseret P, Rousseau C, Barbour B, Léna CJN (2008) High-frequency organization and synchrony of activity in the Purkinje cell layer of the cerebellum. 58:775-788.

Delettre C, Lenaers G, Pelloquin L, Belenguer P, Hamel CP (2002) OPA1 (Kjer type) dominant optic atrophy: a novel mitochondrial disease. Molecular genetics and metabolism 75:97-107.

Demaré S, Kothari A, Calcutt NA, Fernyhough P (2021) Metformin as a potential therapeutic for neurological disease: Mobilizing ampk to repair the nervous system. Expert Review of Neurotherapeutics 21:45-63.

Detmer SA, Chan DC (2007) Functions and dysfunctions of mitochondrial dynamics. Nature reviews Molecular cell biology 8:870-879.

DiMauro S, Schon EA (2003) Mitochondrial respiratory-chain diseases. New England Journal of Medicine 348:2656-2668.

Djordjevic J, Roy Chowdhury S, Snow WM, Perez C, Cadonic C, Fernyhough P, Albensi BC (2020) Early Onset of Sex-Dependent Mitochondrial Deficits in the Cortex of 3xTg Alzheimer's Mice. Cells 9:1541.

Dodson MW, Guo M (2007) Pink1, Parkin, DJ-1 and mitochondrial dysfunction in Parkinson's disease. Current opinion in neurobiology 17:331-337.

Doroshenko ER, Drohomyrecky PC, Gower A, Whetstone H, Cahill LS, Ganguly M, Spring S, Yi TJ, Sled JG, Dunn SE (2021) Peroxisome Proliferator-Activated Receptor-δ Deficiency in Microglia Results in Exacerbated Axonal Injury and Tissue Loss in Experimental Autoimmune Encephalomyelitis. Frontiers in immunology 12:371.

Duncan ID, Marik RL, Broman AT, Heidari M (2017) Thin myelin sheaths as the hallmark of remyelination persist over time and preserve axon function. Proceedings of the National Academy of Sciences 114:E9685-E9691.

Dutta R, Chang A, Doud MK, Kidd GJ, Ribaudo MV, Young EA, Fox RJ, Staugaitis SM, Trapp BD (2011) Demyelination causes synaptic alterations in hippocampi from multiple sclerosis patients. Annals of neurology 69:445-454.

Dutta R, McDonough J, Yin XG, Peterson J, Chang A, Torres T, Gudz T, Macklin EB, Lewis DA, Fox RJ, Rudick R, Mirnics K, Trapp BD (2006) Mitochondrial dysfunction as a cause of axonal degeneration in multiple sclerosis patients. Annals of Neurology 59:478-489.

Dzhashiashvili Y, Zhang Y, Galinska J, Lam I, Grumet M, Salzer JL (2007) Nodes of Ranvier and axon initial segments are ankyrin G–dependent domains that assemble by distinct mechanisms. Journal of Cell Biology 177:857-870.

Eberle M, Ebel P, Mayer CA, Barthelmes J, Tafferner N, Ferreiros N, Ulshöfer T, Henke M, Foerch C, De Bazo AM (2015) Exacerbation of experimental autoimmune encephalomyelitis in ceramide synthase 6 knockout mice is associated with enhanced activation/migration of neutrophils. Immunology and cell biology 93:825-836.

Elshafey R, Hassanien O, Khalil M (2014) Diffusion tensor imaging for characterizing white matter changes in multiple sclerosis. The Egyptian Journal of Radiology and Nuclear Medicine 45:881-888.

Elston T, Wang H, Oster G (1998) Energy transduction in ATP synthase. Nature 391:510-513.

Errea O, Moreno B, Gonzalez-Franquesa A, Garcia-Roves PM, Villoslada P (2015) The disruption of mitochondrial axonal transport is an early event in neuroinflammation. Journal of Neuroinflammation 12:15.

Fabricius C, Berthold CH, Rydmark M (1993) AXOPLASMIC ORGANELLES AT NODES OF RANVIER .2. OCCURRENCE AND DISTRIBUTION IN LARGE MYELINATED SPINAL-CORD AXONS OF THE ADULT CAT. Journal of Neurocytology 22:941-954.

Feldman HM, Yeatman JD, Lee ES, Barde LH, Gaman-Bean S (2010) Diffusion tensor imaging: a review for pediatric researchers and clinicians. Journal of developmental and behavioral pediatrics: JDBP 31:346.

Felts PA, Baker TA, Smith KJ (1997) Conduction in segmentally demyelinated mammalian central axons. Journal of Neuroscience 17:7267-7277.

Ferro A, Carbone E, Zhang J, Marzouk E, Villegas M, Siegel A, Nguyen D, Possidente T, Hartman J, Polley K (2017) Short-term succinic acid treatment mitigates cerebellar mitochondrial OXPHOS dysfunction, neurodegeneration and ataxia in a Purkinje-specific spinocerebellar ataxia type 1 (SCA1) mouse model. PloS one 12:e0188425.

Fetterman JL, Ballinger SW (2019) Mitochondrial genetics regulate nuclear gene expression through metabolites. Proceedings of the National Academy of Sciences 116:15763-15765.

Fiander MD, Stifani N, Nichols M, Akay T, Robertson GS (2017) Kinematic gait parameters are highly sensitive measures of motor deficits and spinal cord injury in mice subjected to experimental autoimmune encephalomyelitis. Behavioural brain research 317:95-108.

Filichia E, Hoffer B, Qi X, Luo Y (2016) Inhibition of Drp1 mitochondrial translocation provides neural protection in dopaminergic system in a Parkinson's disease model induced by MPTP. Scientific reports 6:1-13.

Fonseca-Kelly Z, Nassrallah M, Uribe J, Khan RS, Dine K, Dutt M, Shindler KS (2012) Resveratrol neuroprotection in a chronic mouse model of multiple sclerosis. Frontiers in neurology 3:84.

Friese MA, Schattling B, Fugger L (2014) Mechanisms of neurodegeneration and axonal dysfunction in multiple sclerosis. Nature Reviews Neurology 10:225-238.

Funfschilling U, Supplie LM, Mahad D, Boretius S, Saab AS, Edgar J, Brinkmann BG, Kassmann CM, Tzvetanova ID, Mobius W, Diaz F, Meijer D, Suter U, Hamprecht B, Sereda MW, Moraes CT, Frahm J, Goebbels S, Nave KA (2012) Glycolytic

oligodendrocytes maintain myelin and long-term axonal integrity. Nature 485:517-U130.

Garone C, Minczuk M, Tilokani L, Nagashima S, Paupe V, Prudent J (2018) Mitochondrial dynamics: overview of molecular mechanisms. Essays in biochemistry 62:341-360.

Gautam R, Jachak SM (2009) Recent developments in anti-inflammatory natural products. Medicinal research reviews 29:767-820.

Geisler S, Holmström KM, Skujat D, Fiesel FC, Rothfuss OC, Kahle PJ, Springer W (2010) PINK1/Parkin-mediated mitophagy is dependent on VDAC1 and p62/SQSTM1. Nature cell biology 12:119-131.

Gelfand JM (2014) Multiple sclerosis: diagnosis, differential diagnosis, and clinical presentation. Handbook of clinical neurology 122:269-290.

Ghaiad HR, Nooh MM, El-Sawalhi MM, Shaheen AA (2017) Resveratrol Promotes Remyelination in Cuprizone Model of Multiple Sclerosis: Biochemical and Histological Study. Molecular Neurobiology 54:3219-3229.

Giacomello M, Pyakurel A, Glytsou C, Scorrano L (2020) The cell biology of mitochondrial membrane dynamics. Nature reviews Molecular cell biology 21:204-224.

Glancy B, Balaban RS (2012) Role of mitochondrial Ca2+ in the regulation of cellular energetics. Biochemistry 51:2959-2973.

Groebe A, Clarner T, Baumgartner W, Dang J, Beyer C, Kipp M (2009) Cuprizone treatment induces distinct demyelination, astrocytosis, and microglia cell invasion or proliferation in the mouse cerebellum. The Cerebellum 8:163-174.

Guglielmetti C, Veraart J, Roelant E, Mai Z, Daans J, Van Audekerke J, Naeyaert M, Vanhoutte G, y Palacios RD, Praet J (2016) Diffusion kurtosis imaging probes cortical alterations and white matter pathology following cuprizone induced demyelination and spontaneous remyelination. Neuroimage 125:363-377.

Guo Y, Chan K-H, Lai W-H, Siu C-W, Kwan S-C, Tse H-F, Ho PW-L, Ho JW-M (2013) Human mesenchymal stem cells upregulate CD1dhighCD5+ regulatory B cells in experimental autoimmune encephalomyelitis. Neuroimmunomodulation 20:294-303.

Haines JD, Inglese M, Casaccia PJMSJoMAJoTaPM (2011) Axonal damage in multiple sclerosis. 78:231-243.

Hamilton AM, Forkert ND, Yang R, Wu Y, Rogers JA, Yong VW, Dunn JF (2019) Central nervous system targeted autoimmunity causes regional atrophy: a 9.4 T MRI study of the EAE mouse model of Multiple Sclerosis. Scientific reports 9:1-13.

Harris N, Verley D, Gutman BA, Sutton R (2016) Bi-directional changes in fractional anisotropy after experiment TBI: Disorganization and reorganization? Neuroimage 133:129-143.

Hasselmann JP, Karim H, Khalaj AJ, Ghosh S, Tiwari-Woodruff SK (2017a) Consistent induction of chronic experimental autoimmune encephalomyelitis in C57BL/6 mice for the longitudinal study of pathology and repair. J Neurosci Methods.

Hasselmann JPC, Karim H, Khalaj AJ, Ghosh S, Tiwari-Woodruff SK (2017b) Consistent induction of chronic experimental autoimmune encephalomyelitis in C57BL/6 mice for the longitudinal study of pathology and repair. J Neurosci Methods 284:71-84.

Hasselmann JPC, Karim H, Khalaj AJ, Ghosh S, Tiwari-Woodruff SK (2017c) Consistent induction of chronic experimental autoimmune encephalomyelitis in C57BL/6 mice for the longitudinal study of pathology and repair. Journal of Neuroscience Methods 284:71-84.

Hayes LR, Asress SA, Li Y, Galkin A, Stepanova A, Kawamata H, Manfredi G, Glass JD (2019) Distal denervation in the SOD1 knockout mouse correlates with loss of mitochondria at the motor nerve terminal. Experimental neurology 318:251-257.

Herbert AL, Monk KRJCoin (2017) Advances in myelinating glial cell development. 42:53-60.

Hesseltine S, Law M, Babb J, Rad M, Lopez S, Ge Y, Johnson G, Grossman R (2006) Diffusion tensor imaging in multiple sclerosis: assessment of regional differences in the axial plane within normal-appearing cervical spinal cord. American Journal of Neuroradiology 27:1189-1193.

Hira S, Packialakshmi B, Zhou X (2019) EAE-induced upregulation of mitochondrial MnSOD is associated with increases of mitochondrial SGK1 and Tom20 protein in the mouse kidney cortex. The Journal of Physiological Sciences 69:723-732.

Hiremath M, Saito Y, Knapp G, Ting J-Y, Suzuki K, Matsushima G (1998) Microglial/macrophage accumulation during cuprizone-induced demyelination in C57BL/6 mice. Journal of neuroimmunology 92:38-49.

Hogan V, White K, Edgar J, McGill A, Karim S, McLaughlin M, Griffiths I, Turnbull D, Nichols P (2009) Increase in Mitochondrial Density Within Axons and Supporting

Cells in Response to Demyelination in the Plp1 Mouse Model. Journal of Neuroscience Research 87:452-459.

Hollenbeck PJ, Saxton WM (2005) The axonal transport of mitochondria. Journal of cell science 118:5411-5419.

Honorat JA, Nakatsuji Y, Shimizu M, Kinoshita M, Sumi-Akamaru H, Sasaki T, Takata K, Koda T, Namba A, Yamashita K (2017) Febuxostat ameliorates secondary progressive experimental autoimmune encephalomyelitis by restoring mitochondrial energy production in a GOT2-dependent manner. PloS one 12:e0187215.

Horzum U, Ozdil B, Pesen-Okvur D (2014) Step-by-step quantitative analysis of focal adhesions. MethodsX 1:56-59.

Howarth C, Gleeson P, Attwell D (2012) Updated energy budgets for neural computation in the neocortex and cerebellum. Journal of Cerebral Blood Flow & Metabolism 32:1222-1232.

Hu C, Huang Y, Li L (2017) Drp1-dependent mitochondrial fission plays critical roles in physiological and pathological progresses in mammals. International journal of molecular sciences 18:144.

Imamura H, Nhat KPH, Togawa H, Saito K, Iino R, Kato-Yamada Y, Nagai T, Noji H (2009) Visualization of ATP levels inside single living cells with fluorescence resonance energy transfer-based genetically encoded indicators. Proceedings of the National Academy of Sciences 106:15651-15656.

Imler Jr TJ, Petro TM (2009) Decreased severity of experimental autoimmune encephalomyelitis during resveratrol administration is associated with increased IL-17+ IL-10+ T cells, CD4− IFN-γ+ cells, and decreased macrophage IL-6 expression. International immunopharmacology 9:134-143.

Ineichen BV, Zhu K, Carlström KE (2020) Axonal mitochondria adjust in size depending on g-ratio of surrounding myelin during homeostasis and advanced remyelination. Journal of Neuroscience Research.

Ishihara N, Nomura M, Jofuku A, Kato H, Suzuki SO, Masuda K, Otera H, Nakanishi Y, Nonaka I, Goto Y-i (2009) Mitochondrial fission factor Drp1 is essential for embryonic development and synapse formation in mice. Nature cell biology 11:958-966.

Islam MT (2017) Oxidative stress and mitochondrial dysfunction-linked neurodegenerative disorders. Neurological research 39:73-82.

Jahani-Asl A, Germain M, Slack RS (2010) Mitochondria: joining forces to thwart cell death. Biochimica et Biophysica Acta (BBA)-Molecular Basis of Disease 1802:162-166.

Jang M, Cai L, Udeani GO, Slowing KV, Thomas CF, Beecher CW, Fong HH, Farnsworth NR, Kinghorn AD, Mehta RG (1997) Cancer chemopreventive activity of resveratrol, a natural product derived from grapes. Science 275:218-220.

Jardim FR, de Rossi FT, Nascimento MX, da Silva Barros RG, Borges PA, Prescilio IC, de Oliveira MR (2018) Resveratrol and brain mitochondria: a review. Molecular neurobiology 55:2085-2101.

Jia X, Madireddy L, Caillier S, Santaniello A, Esposito F, Comi G, Stuve O, Zhou Y, Taylor B, Kilpatrick T (2018) Genome sequencing uncovers phenocopies in primary progressive multiple sclerosis. Annals of neurology 84:51-63.

Jiang HR, Milovanović M, Allan D, Niedbala W, Besnard AG, Fukada SY, Alves-Filho JC, Togbe D, Goodyear CS, Linington C (2012) IL-33 attenuates EAE by suppressing IL-17 and IFN-γ production and inducing alternatively activated macrophages. European journal of immunology 42:1804-1814.

Joshi DC, Zhang CL, Lin TM, Gusain A, Harris MG, Tree E, Yin YW, Wu C, Sheng ZH, Dempsey RJ, Fabry Z, Chiu SY (2015) Deletion of Mitochondrial Anchoring Protects Dysmyelinating Shiverer: Implications for Progressive MS. Journal of Neuroscience 35:5293-5306.

Jürgensmeier JM, Xie Z, Deveraux Q, Ellerby L, Bredesen D, Reed JC (1998) Bax directly induces release of cytochrome c from isolated mitochondria. Proceedings of the National Academy of Sciences 95:4997-5002.

Kalinin S, Meares GP, Lin SX, Pietruczyk EA, Saher G, Spieth L, Nave KA, Boullerne AI, Lutz SE, Benveniste EN (2020) Liver kinase B1 depletion from astrocytes worsens disease in a mouse model of multiple sclerosis. Glia 68:600-616.

Kann O, Kovács R (2007) Mitochondria and neuronal activity. American Journal of Physiology-Cell Physiology 292:C641-C657.

Kaplan MR, Meyer-Franke A, Lambert S, Bennett V, Duncan I, Levinson S, Barres B (1997) Induction of sodium channel clustering by oligodendrocytes. Nature 386:724-728.

Karim H, Kim SH, Lapato AS, Yasui N, Katzenellenbogen JA, Tiwari-Woodruff SK (2018) Increase in chemokine CXCL1 by ERβ ligand treatment is a key mediator

in promoting axon myelination. Proceedings of the National Academy of Sciences:201721732.

Karim H, Kim SH, Lauderdale K, Lapato AS, Atkinson K, Yasui N, Yamate-Morgan H, Sekyi M, Katzenellenbogen JA, Tiwari-Woodruff SK (2019) Analogues of ERβ ligand chloroindazole exert immunomodulatory and remyelinating effects in a mouse model of multiple sclerosis. Scientific Reports 9:503.

Kasischke KA, Vishwasrao HD, Fisher PJ, Zipfel WR, Webb WW (2004) Neural activity triggers neuronal oxidative metabolism followed by astrocytic glycolysis. Science 305:99-103.

Katoh M, Wu B, Nguyen HB, Thai TQ, Yamasaki R, Lu H, Rietsch AM, Zorlu MM, Shinozaki Y, Saitoh Y (2017) Polymorphic regulation of mitochondrial fission and fusion modifies phenotypes of microglia in neuroinflammation. Scientific reports 7:1-14.

Kemp K, Gray E, Wilkins A, Scolding N (2012) Purkinje cell fusion and binucleate heterokaryon formation in multiple sclerosis cerebellum. Brain 135:2962-2972.

Kenney MC, Chwa M, Atilano SR, Falatoonzadeh P, Ramirez C, Malik D, Tarek M, Cáceres-del-Carpio J, Nesburn AB, Boyer DS (2014a) Inherited mitochondrial DNA variants can affect complement, inflammation and apoptosis pathways: insights into mitochondrial–nuclear interactions. Human Molecular Genetics 23:3537-3551.

Kenney MC, Chwa M, Atilano SR, Falatoonzadeh P, Ramirez C, Malik D, Tarek M, del Carpio JC, Nesburn AB, Boyer DS (2014b) Molecular and bioenergetic differences between cells with African versus European inherited mitochondrial DNA haplogroups: implications for population susceptibility to diseases. Biochimica et Biophysica Acta (BBA)-Molecular Basis of Disease 1842:208-219.

Khalaj AJ, Hasselmann J, Augello C, Moore S, Tiwari-Woodruff SK (2016) Nudging oligodendrocyte intrinsic signaling to remyelinate and repair: Estrogen receptor ligand effects. The Journal of steroid biochemistry and molecular biology 160:43-52.

Kipp M, Nyamoya S, Hochstrasser T, Amor S (2017) Multiple sclerosis animal models: a clinical and histopathological perspective. Brain Pathology 27:123-137.

Kipp M, Clarner T, Dang J, Copray S, Beyer C (2009) The cuprizone animal model: new insights into an old story. Acta Neuropathologica 118:723-736.

Kiryu-Seo S, Ohno N, Kidd GJ, Komuro H, Trapp BD (2010) Demyelination Increases Axonal Stationary Mitochondrial Size and the Speed of Axonal Mitochondrial Transport. Journal of Neuroscience 30:6658-6666.

Kis B, Rumberg B, Berlit P (2008) Clinical characteristics of patients with late-onset multiple sclerosis. Journal of neurology 255:697-702.

Klawiter EC, Schmidt RE, Trinkaus K, Liang H-F, Budde MD, Naismith RT, Song S-K, Cross AH, Benzinger TL (2011) Radial diffusivity predicts demyelination in ex vivo multiple sclerosis spinal cords. Neuroimage 55:1454-1460.

Klinge CM (2017) Estrogens regulate life and death in mitochondria. Journal of bioenergetics and biomembranes 49:307-324.

Klingenberg M (1980) The ADP-ATP translocation in mitochondria, a membrane potential controlled transport. The Journal of membrane biology 56:97-105.

Koch M, Mostert J, Heersema D, De Keyser J (2007) Tremor in multiple sclerosis. Journal of neurology 254:133-145.

Korshunov SS, Skulachev VP, Starkov AA (1997) High protonic potential actuates a mechanism of production of reactive oxygen species in mitochondria. FEBS letters 416:15-18.

Kumar S, Patel R, Moore S, Crawford DK, Suwanna N, Mangiardi M, Tiwari-Woodruff SK (2013) Estrogen receptor β ligand therapy activates PI3K/Akt/mTOR signaling in oligodendrocytes and promotes remyelination in a mouse model of multiple sclerosis. Neurobiology of disease 56:131-144.

Kurtzke JF, Beebe GW, Nagler B, Kurland LT, Auth TL (1977) Studies on the natural history of multiple sclerosis—8: early prognostic features of the later course of the illness. Journal of chronic diseases 30:819-830.

Kutzelnigg A, Faber-Rod JC, Bauer J, Lucchinetti CF, Sorensen PS, Laursen H, Stadelmann C, Brück W, Rauschka H, Schmidbauer M (2007) Widespread demyelination in the cerebellar cortex in multiple sclerosis. Brain pathology 17:38-44.

Lagouge M, Argmann C, Gerhart-Hines Z, Meziane H, Lerin C, Daussin F, Messadeq N, Milne J, Lambert P, Elliott P (2006) Resveratrol improves mitochondrial function and protects against metabolic disease by activating SIRT1 and PGC-1α. Cell 127:1109-1122.

Lambert AJ, Brand MD (2004) Superoxide production by NADH: ubiquinone oxidoreductase (complex I) depends on the pH gradient across the mitochondrial inner membrane. Biochemical Journal 382:511-517.

Lapato AS, Szu JI, Hasselmann JP, Khalaj AJ, Binder DK, Tiwari-Woodruff SK (2017) Chronic demyelination-induced seizures. Neuroscience 346:409-422.

Lassmann H, van Horssen J (2016) Oxidative stress and its impact on neurons and glia in multiple sclerosis lesions. Biochimica et Biophysica Acta (BBA)-Molecular Basis of Disease 1862:506-510.

Le Bihan D, Mangin JF, Poupon C, Clark CA, Pappata S, Molko N, Chabriat H (2001) Diffusion tensor imaging: concepts and applications. Journal of magnetic resonance imaging 13:534-546.

Lee Y, Morrison BM, Li Y, Lengacher S, Farah MH, Hoffman PN, Liu Y, Tsingalia A, Jin L, Zhang P-W (2012) Oligodendroglia metabolically support axons and contribute to neurodegeneration. Nature 487:443-448.

Li HQ, Yin B, Quan C, Geng DY, Yu H, Bao YF, Liu J, Li YX (2018) Evaluation of patients with relapsing-remitting multiple sclerosis using tract-based spatial statistics analysis: diffusion kurtosis imaging. BMC neurology 18:1-6.

Li S, Clements R, Sulak M, Gregory R, Freeman E, McDonough J (2013) Decreased NAA in gray matter is correlated with decreased availability of acetate in white matter in postmortem multiple sclerosis cortex. Neurochemical research 38:2385-2396.

Li Y, Chiaravalloti ND, Hillary FG, DeLuca J, Liu W-C, Kalnin AJ, Ricker JH (2004) Differential cerebellar activation on functional magnetic resonance imaging during working memory performance in persons with multiple sclerosis. Archives of physical medicine and rehabilitation 85:635-639.

Li Z, Peng Y, Hufnagel RB, Hu Y-C, Zhao C, Queme LF, Khuchua Z, Driver AM, Dong F, Lu QR (2017) Loss of SLC25A46 causes neurodegeneration by affecting mitochondrial dynamics and energy production in mice. Human molecular genetics 26:3776-3791.

Licht-Mayer S, Campbell GR, Canizares M, Mehta AR, Gane AB, McGill K, Ghosh A, Fullerton A, Menezes N, Dean J (2020) Enhanced axonal response of mitochondria to demyelination offers neuroprotection: implications for multiple sclerosis. Acta neuropathologica:1-25.

Liesa M, Palacín M, Zorzano A (2009) Mitochondrial dynamics in mammalian health and disease. Physiological reviews 89:799-845.

Lin MT, Beal MF (2006) Mitochondrial dysfunction and oxidative stress in neurodegenerative diseases. Nature 443:787-795.

Lindberg MK, Movérare S, Skrtic S, Gao H, Dahlman-Wright K, Gustafsson J-Ak, Ohlsson C (2003) Estrogen receptor (ER)-β reduces ERα-regulated gene transcription, supporting a "Ying Yang" relationship between ERα and ERβ in mice. Molecular endocrinology 17:203-208.

Liu YJ, McIntyre RL, Janssens GE, Houtkooper RH (2020) Mitochondrial fission and fusion: A dynamic role in aging and potential target for age-related disease. Mechanisms of Ageing and Development 186:111212.

Llinas R, Sugimori M (1980) Electrophysiological properties of in vitro Purkinje cell dendrites in mammalian cerebellar slices. The Journal of physiology 305:197-213.

Llinás R, Hess R (1976) Tetrodotoxin-resistant dendritic spikes in avian Purkinje cells. Proceedings of the National Academy of Sciences 73:2520-2523.

Lopez-Diego RS, Weiner HL (2008) Novel therapeutic strategies for multiple sclerosis—a multifaceted adversary. Nature Reviews Drug Discovery 7:909.

Louis ED (2018) Essential tremor and the cerebellum. Handbook of clinical neurology 155:245-258.

Lucchinetti C, Bruck W, Parisi J, Scheithauer B, Rodriguez M, Lassman H (2000) Heterogeneity of multiple sclerosis lesions: implications for the pathogenesis of demyelination. Annals of neurology 47:707-717.

Ludwin SK (1978) CENTRAL NERVOUS-SYSTEM DEMYELINATION AND REMYELINATION IN MOUSE - ULTRASTRUCTURAL-STUDY OF CUPRIZONE TOXICITY. Laboratory Investigation 39:597-612.

Luo F, Herrup K, Qi X, Yang Y (2017a) Inhibition of Drp1 hyper-activation is protective in animal models of experimental multiple sclerosis. Exp Neurol 292:21-34.

Luo F, Herrup K, Qi X, Yang Y (2017b) Inhibition of Drp1 hyper-activation is protective in animal models of experimental multiple sclerosis. Experimental neurology 292:21-34.

Lynch MA (2020) Can the emerging field of immunometabolism provide insights into neuroinflammation? Progress in neurobiology 184:101719.

MacKenzie-Graham A, Tiwari-Woodruff SK, Sharma G, Aguilar C, Vo KT, Strickland LV, Morales L, Fubara B, Martin M, Jacobs RE (2009) Purkinje cell loss in experimental autoimmune encephalomyelitis. Neuroimage 48:637-651.

MacKenzie-Graham AJ, Rinek GA, Avedisian A, Morales LB, Umeda E, Boulat B, Jacobs RE, Toga AW, Voskuhl RR (2012) Estrogen treatment prevents gray matter atrophy in experimental autoimmune encephalomyelitis. Journal of neuroscience research 90:1310-1323.

Madsen PM, Pinto M, Patel S, McCarthy S, Gao H, Taherian M, Karmally S, Pereira CV, Dvoriantchikova G, Ivanov D, Tanaka KF, Moraes CT, Brambilla R (2017) Mitochondrial DNA double-strand breaks in oligodendrocytes cause demyelination, axonal injury and CNS inflammation. J Neurosci.

Mahad D, Ziabreva I, Lassmann H, Turnbull D (2008) Mitochondrial defects in acute multiple sclerosis lesions. Brain 131:1722-1735.

Mahad DJ, Ziabreva I, Campbell G, Lax N, White K, Hanson PS, Lassmann H, Turnbull DM (2009) Mitochondrial changes within axons in multiple sclerosis. Brain 132:1161-1174.

Mallon BS, Shick HE, Kidd GJ, Macklin WB (2002) Proteolipid promoter activity distinguishes two populations of NG2-positive cells throughout neonatal cortical development. J Neurosci 22:876-885.

Mancini A, Tantucci M, Mazzocchetti P, de Iure A, Durante V, Macchioni L, Giampà C, Alvino A, Gaetani L, Costa C (2018) Microglial activation and the nitric oxide/cGMP/PKG pathway underlie enhanced neuronal vulnerability to mitochondrial dysfunction in experimental multiple sclerosis. Neurobiology of disease 113:97-108.

Mangiardi M, Crawford DK, Xia X, Du S, Simon-Freeman R, Voskuhl RR, Tiwari-Woodruff SK (2011a) An animal model of cortical and callosal pathology in multiple sclerosis. Brain Pathol 21:263-278.

Mangiardi M, Crawford DK, Xia X, Du S, Simon-Freeman R, Voskuhl RR, Tiwari-Woodruff SK (2011b) An animal model of cortical and callosal pathology in multiple sclerosis. Brain Pathology 21:263-278.

Mar FM, Simões AR, Leite S, Morgado MM, Santos TE, Rodrigo IS, Teixeira CA, Misgeld T, Sousa MM (2014) CNS axons globally increase axonal transport after peripheral conditioning. Journal of Neuroscience 34:5965-5970.

Matsushima GK, Morell P (2001) The neurotoxicant, cuprizone, as a model to study demyelination and remyelination in the central nervous system. Brain Pathology 11:107-116.

McDonald WI, Compston A, Edan G, Goodkin D, Hartung HP, Lublin FD, McFarland HF, Paty DW, Polman CH, Reingold SC (2001) Recommended diagnostic criteria for multiple sclerosis: guidelines from the International Panel on the diagnosis of multiple sclerosis. Annals of neurology 50:121-127.

McWilliams TG, Prescott AR, Allen GF, Tamjar J, Munson MJ, Thomson C, Muqit MM, Ganley IG (2016) mito-QC illuminates mitophagy and mitochondrial architecture in vivo. Journal of Cell Biology 214:333-345.

Mink JW, Blumenschine RJ, Adams DB (1981) Ratio of central nervous system to body metabolism in vertebrates: its constancy and functional basis. American Journal of Physiology-Regulatory, Integrative and Comparative Physiology 241:R203-R212.

Misgeld T, Kerschensteiner M, Bareyre FM, Burgess RW, Lichtman JW (2007) Imaging axonal transport of mitochondria in vivo. Nature methods 4:559-561.

Misko AL, Sasaki Y, Tuck E, Milbrandt J, Baloh RH (2012) Mitofusin2 mutations disrupt axonal mitochondrial positioning and promote axon degeneration. Journal of Neuroscience 32:4145-4155.

Moore SM, Khalaj AJ, Kumar S, Winchester Z, Yoon JH, Yoo T, Martinez-Torres L, Yasui N, Katzenellenbogen JA, Tiwari-Woodruff SK (2014) Multiple functional therapeutic effects of the estrogen receptor beta agonist indazole-Cl in a mouse model of multiple sclerosis. Proceedings of the National Academy of Sciences of the United States of America 111:18061-18066.

Morell P, Wiesmann U (1984) A CORRELATIVE SYNOPSIS OF THE LEUKODYSTROPHIES. Neuropediatrics 15:62-65.

Mori S, Zhang J (2006) Principles of diffusion tensor imaging and its applications to basic neuroscience research. Neuron 51:527-539.

Morrison BM, Lee Y, Rothstein JD (2013) Oligodendroglia: metabolic supporters of axons. Trends in cell biology 23:644-651.

Morton SM, Bastian AJ (2004) Cerebellar control of balance and locomotion. The Neuroscientist 10:247-259.

Mutsaers S, Carroll W (1998) Focal accumulation of intra-axonal mitochondria in demyelination of the cat optic nerve. Acta neuropathologica 96:139-143.

Nagy AM, Fekete R, Horvath G, Koncsos G, Kriston C, Sebestyen A, Giricz Z, Kornyei Z, Madarasz E, Tretter L (2018) Versatility of microglial bioenergetic machinery under starving conditions. Biochimica et Biophysica Acta (BBA)-Bioenergetics 1859:201-214.

Ng X, Sadeghian M, Heales S, Hargreaves IP (2019) Assessment of Mitochondrial Dysfunction in Experimental Autoimmune Encephalomyelitis (EAE) Models of Multiple Sclerosis. International journal of molecular sciences 20:4975.

Nicholson SK, Tucker GA, Brameld JM (2010) Physiological concentrations of dietary polyphenols regulate vascular endothelial cell expression of genes important in cardiovascular health. British Journal of Nutrition 103:1398-1403.

Nikic I, Merkler D, Sorbara C, Brinkoetter M, Kreutzfeldt M, Bareyre FM, Bruck W, Bishop D, Misgeld T, Kerschensteiner M (2011) A reversible form of axon damage in experimental autoimmune encephalomyelitis and multiple sclerosis. Nature Medicine 17:495-U135.

Nimmerjahn A, Kirchhoff F, Helmchen F (2005) Resting microglial cells are highly dynamic surveillants of brain parenchyma in vivo. Science 308:1314-1318.

Offner H, Adlard K, Zamora A, Vandenbark AA (2000) Estrogen potentiates treatment with T-cell receptor protein of female mice with experimental encephalomyelitis. The Journal of clinical investigation 105:1465-1472.

Ohno N, Chiang H, Mahad DJ, Kidd GJ, Liu LP, Ransohoff RM, Sheng ZH, Komuro H, Trapp BD (2014) Mitochondrial immobilization mediated by syntaphilin facilitates survival of demyelinated axons. Proceedings of the National Academy of Sciences of the United States of America 111:9953-9958.

Ontaneda D, Sakaie K, Lin J, Wang X, Lowe MJ, Phillips MD, Fox RJ (2014) Identifying the start of multiple sclerosis injury: a serial DTI study. Journal of Neuroimaging 24:569-576.

Pallàs M, Porquet D, Vicente A, Sanfeliu C (2013) Resveratrol: new avenues for a natural compound in neuroprotection. Current pharmaceutical design 19:6726-6731.

Pellerin L, Magistretti PJ (1994) Glutamate uptake into astrocytes stimulates aerobic glycolysis: a mechanism coupling neuronal activity to glucose utilization. Proceedings of the National Academy of Sciences 91:10625-10629.

Person AL, Raman IMJN (2012) Purkinje neuron synchrony elicits time-locked spiking in the cerebellar nuclei. 481:502.

Pfanner N, Warscheid B, Wiedemann N (2019) Mitochondrial proteins: from biogenesis to functional networks. Nature reviews Molecular cell biology 20:267-284.

Pham AH, McCaffery JM, Chan DC (2012) Mouse lines with photo-activatable mitochondria to study mitochondrial dynamics. Genesis 50:833-843.

Philips T, Rothstein JD (2017) Oligodendroglia: metabolic supporters of neurons. The Journal of clinical investigation 127:3271-3280.

Popescu BFG, Pirko I, Lucchinetti CF (2013) Pathology of multiple sclerosis: where do we stand? CONTINUUM: Lifelong Learning in Neurology 19:901.

Praet J, Guglielmetti C, Berneman Z, Van der Linden A, Ponsaerts P (2014) Cellular and molecular neuropathology of the cuprizone mouse model: clinical relevance for multiple sclerosis. Neuroscience & Biobehavioral Reviews 47:485-505.

Qi X, Lewin AS, Sun L, Hauswirth WW, Guy J (2006) Mitochondrial protein nitration primes neurodegeneration in experimental autoimmune encephalomyelitis. Journal of Biological Chemistry 281:31950-31962.

Rawji KS, Yong VW (2013) The benefits and detriments of macrophages/microglia in models of multiple sclerosis. Clinical and Developmental Immunology 2013.

Redondo J, Kemp K, Hares K, Rice C, Scolding N, Wilkins A (2015) Purkinje cell pathology and loss in multiple sclerosis cerebellum. Brain Pathology 25:692-700.

Ren W, Ji A, Karmach O, Carter DG, Martins-Green MM, Ai HW (2016) A membrane-activatable near-infrared fluorescent probe with ultra-photostability for mitochondrial membrane potentials. Analyst 141:3679-3685.

Rice GP, Hartung H-P, Calabresi PA (2005) Anti-α4 integrin therapy for multiple sclerosis: mechanisms and rationale. Neurology 64:1336-1342.

Rolfe D, Brown GC (1997) Cellular energy utilization and molecular origin of standard metabolic rate in mammals. Physiological reviews 77:731-758.

Ross JM, Stewart JB, Hagström E, Brené S, Mourier A, Coppotelli G, Freyer C, Lagouge M, Hoffer BJ, Olson L (2013) Germline mitochondrial DNA mutations aggravate ageing and can impair brain development. Nature 501:412-415.

Rottenberg H, Scarpa A (1974) Calcium uptake and membrane potential in mitochondria. Biochemistry 13:4811-4817.

Sadeghian M, Mastrolia V, Haddad AR, Mosley A, Mullali G, Schiza D, Sajic M, Hargreaves I, Heales S, Duchen MR, Smith KJ (2016) Mitochondrial dysfunction is an important cause of neurological deficits in an inflammatory model of multiple sclerosis. Scientific Reports 6:14.

Saez I, Duran J, Sinadinos C, Beltran A, Yanes O, Tevy MF, Martínez-Pons C, Milán M, Guinovart JJ (2014) Neurons have an active glycogen metabolism that contributes to tolerance to hypoxia. Journal of Cerebral Blood Flow & Metabolism 34:945-955.

Saijo K, Collier JG, Li AC, Katzenellenbogen JA, Glass CK (2011) An ADIOL-ERβ-CtBP transrepression pathway negatively regulates microglia-mediated inflammation. Cell 145:584-595.

Salabei JK, Gibb AA, Hill BG (2014) Comprehensive measurement of respiratory activity in permeabilized cells using extracellular flux analysis. Nature protocols 9:421-438.

Salter MW, Stevens B (2017) Microglia emerge as central players in brain disease. Nature medicine 23:1018.

Sato F, Martinez NE, Shahid M, Rose JW, Carlson NG, Tsunoda I (2013) Resveratrol exacerbates both autoimmune and viral models of multiple sclerosis. The American journal of pathology 183:1390-1396.

Schmidt T, Awad H, Slowik A, Beyer C, Kipp M, Clarner T (2013) Regional heterogeneity of cuprizone-induced demyelination: topographical aspects of the midline of the corpus callosum. Journal of Molecular Neuroscience 49:80-88.

Sekyi MT, Lauderdale K, Atkinson KC, Golestany B, Karim H, Feri M, Soto JS, Diaz C, Kim SH, Cilluffo M (2021) Alleviation of extensive visual pathway dysfunction by a remyelinating drug in a chronic mouse model of multiple sclerosis. Brain Pathology 31:312-332.

Sen MK, Almuslehi MS, Shortland PJ, Coorssen JR, Mahns DA (2020) Revisiting the pathoetiology of multiple sclerosis: has the tail been wagging the mouse? Frontiers in Immunology 11.

Shepherd GM (1988) Neurobiology: Oxford University Press.

Shepherd TM, Thelwall PE, Stanisz GJ, Blackband SJ (2009) Aldehyde fixative solutions alter the water relaxation and diffusion properties of nervous tissue. Magnetic resonance in medicine 62:26-34.

Shields SD, Butt RP, Dib-Hajj SD, Waxman SG (2015) Oral administration of PF-01247324, a subtype-selective Nav1. 8 blocker, reverses cerebellar deficits in a mouse model of multiple sclerosis. PloS one 10:e0119067.

Shields SD, Cheng X, Gasser A, Saab CY, Tyrrell L, Eastman EM, Iwata M, Zwinger PJ, Black JA, Dib-Hajj SD (2012) A channelopathy contributes to cerebellar dysfunction in a model of multiple sclerosis. Annals of neurology 71:186-194.

Shin T, Ahn M, Matsumoto Y (2012) Mechanism of experimental autoimmune encephalomyelitis in Lewis rats: recent insights from macrophages. Anatomy & cell biology 45:141-148.

Shindler KS, Ventura E, Rex TS, Elliott P, Rostami A (2007) SIRT1 activation confers neuroprotection in experimental optic neuritis. Investigative ophthalmology & visual science 48:3602-3609.

Shindler KS, Ventura E, Dutt M, Elliott P, Fitzgerald DC, Rostami A (2010) Oral resveratrol reduces neuronal damage in a model of multiple sclerosis. Journal of Neuro-Ophthalmology 30:328.

Sicotte NL, Liva SM, Klutch R, Pfeiffer P, Bouvier S, Odesa S, Wu T, Voskuhl RR (2002) Treatment of multiple sclerosis with the pregnancy hormone estriol. Annals of neurology 52:421-428.

Silver I, Erecińska M (1998) Oxygen and ion concentrations in normoxic and hypoxic brain cells. In: Oxygen Transport to Tissue XX, pp 7-16: Springer.

Singh I, Samuvel DJ, Choi S, Saxena N, Singh AK, Won J (2018) Combination therapy of lovastatin and AMP-activated protein kinase activator improves mitochondrial and peroxisomal functions and clinical disease in experimental autoimmune encephalomyelitis model. Immunology 154:434-451.

Singh NP, Hegde VL, Hofseth LJ, Nagarkatti M, Nagarkatti P (2007) Resveratrol (trans-3, 5, 4′-trihydroxystilbene) ameliorates experimental allergic encephalomyelitis, primarily via induction of apoptosis in T cells involving activation of aryl hydrocarbon receptor and estrogen receptor. Molecular pharmacology 72:1508-1521.

Singhal NK, Sternbach S, Fleming S, Alkhayer K, Shelestak J, Popescu D, Weaver A, Clements R, Wasek B, Bottiglieri T (2020) Betaine restores epigenetic control and supports neuronal mitochondria in the cuprizone mouse model of multiple sclerosis. Epigenetics 15:871-886.

Skripuletz T, Bussmann JH, Gudi V, Koutsoudaki PN, Pul R, Moharregh-Khiabani D, Lindner M, Stangel M (2010) Cerebellar cortical demyelination in the murine cuprizone model. Brain pathology 20:301-312.

Song S-K, Sun S-W, Ramsbottom MJ, Chang C, Russell J, Cross AH (2002) Dysmyelination revealed through MRI as increased radial (but unchanged axial) diffusion of water. Neuroimage 17:1429-1436.

Song S-K, Sun S-W, Ju W-K, Lin S-J, Cross AH, Neufeld AH (2003) Diffusion tensor imaging detects and differentiates axon and myelin degeneration in mouse optic nerve after retinal ischemia. Neuroimage 20:1714-1722.

Song S-K, Yoshino J, Le TQ, Lin S-J, Sun S-W, Cross AH, Armstrong RC (2005) Demyelination increases radial diffusivity in corpus callosum of mouse brain. Neuroimage 26:132-140.

Steelman AJ, Thompson JP, Li J (2012) Demyelination and remyelination in anatomically distinct regions of the corpus callosum following cuprizone intoxication. Neuroscience research 72:32-42.

Sterky FH, Lee S, Wibom R, Olson L, Larsson N-G (2011) Impaired mitochondrial transport and Parkin-independent degeneration of respiratory chain-deficient dopamine neurons in vivo. Proceedings of the National Academy of Sciences 108:12937-12942.

Stys PK, Zamponi GW, Van Minnen J, Geurts JJ (2012) Will the real multiple sclerosis please stand up? Nature Reviews Neuroscience 13:507-514.

Susuki K, Chang K-J, Zollinger DR, Liu Y, Ogawa Y, Eshed-Eisenbach Y, Dours-Zimmermann MT, Oses-Prieto JA, Burlingame AL, Seidenbecher CI (2013) Three mechanisms assemble central nervous system nodes of Ranvier. Neuron 78:469-482.

Suzuki K (1969) Giant hepatic mitochondria: production in mice fed with cuprizone. Science 163:81-82.

Taylor RW, Turnbull DM (2005) Mitochondrial DNA mutations in human disease. Nature Reviews Genetics 6:389-402.

Thai TQ, Nguyen HB, Sui Y, Ikenaka K, Oda T, Ohno N (2019) Interactions between mitochondria and endoplasmic reticulum in demyelinated axons. Medical Molecular Morphology 52:135-146.

Thiessen JD, Zhang Y, Zhang H, Wang L, Buist R, Del Bigio MR, Kong J, Li XM, Martin M (2013) Quantitative MRI and ultrastructural examination of the cuprizone mouse model of demyelination. NMR in Biomedicine 26:1562-1581.

Titus HE, Chen Y, Podojil JR, Robinson AP, Balabanov R, Popko B, Miller SD (2020) Pre-clinical and clinical implications of "Inside-Out" vs."Outside-In" paradigms in multiple sclerosis etiopathogenesis. Frontiers in cellular neuroscience 14.

Tiwari-Woodruff S, Morales LBJ, Lee R, Voskuhl RR (2007) Differential neuroprotective and antiinflammatory effects of estrogen receptor (ER) α and ERβ ligand treatment. Proceedings of the National Academy of Sciences 104:14813-14818.

Tjoa C, Benedict R, Weinstock-Guttman B, Fabiano A, Bakshi R (2005) MRI T2 hypointensity of the dentate nucleus is related to ambulatory impairment in multiple sclerosis. Journal of the neurological sciences 234:17-24.

Tranah GJ, Santaniello A, Caillier SJ, D'Alfonso S, Boneschi FM, Hauser SL, Oksenberg JR (2015) Mitochondrial DNA sequence variation in multiple sclerosis. Neurology 85:325-330.

Underwood E, Redell JB, Zhao J, Moore AN, Dash PK (2020) A method for assessing tissue respiration in anatomically defined brain regions. Scientific reports 10:1-14.

Van der Bliek AM, Shen Q, Kawajiri S (2013) Mechanisms of mitochondrial fission and fusion. Cold Spring Harbor perspectives in biology 5:a011072.

van Hameren G, Campbell G, Deck M, Berthelot J, Gautier B, Quintana P, Chrast R, Tricaud N (2019) In vivo real-time dynamics of ATP and ROS production in axonal mitochondria show decoupling in mouse models of peripheral neuropathies. Acta neuropathologica communications 7:1-16.

Vannucci RC, Brucklacher RM, Vannucci SJ (1997) Effect of carbon dioxide on cerebral metabolism during hypoxia-ischemia in the immature rat. Pediatric research 42:24-29.

Varga E, Pandur E, Abrahám H, Horváth A, Ács P, Komoly S, Miseta A, Sipos K (2018) Cuprizone Administration Alters the Iron Metabolism in the Mouse Model of Multiple Sclerosis. Cellular and molecular neurobiology:1-17.

Ventura-Antunes L, Mota B, Herculano-Houzel S (2013) Different scaling of white matter volume, cortical connectivity, and gyrification across rodent and primate brains. Frontiers in neuroanatomy 7:3.

Vyshkina T, Sylvester A, Sadiq S, Bonilla E, Canter JA, Perl A, Kalman B (2008) Association of common mitochondrial DNA variants with multiple sclerosis and systemic lupus erythematosus. Clinical Immunology 129:31-35.

Wallace DC (1992) DISEASES OF THE MITOCHONDRIAL-DNA. Annual Review of Biochemistry 61:1175-1212.

Walshe J, Munro N (1995) Zinc-induced deterioration in Wilson's disease aborted by treatment with penicillamine, dimercaprol, and a novel zero copper diet. Archives of neurology 52:10-11.

Wang D, Li S-P, Fu J-S, Zhang S, Bai L, Guo L (2016) Resveratrol defends blood-brain barrier integrity in experimental autoimmune encephalomyelitis mice. Journal of neurophysiology 116:2173-2179.

Wang L, Pavlou S, Du X, Bhuckory M, Xu H, Chen M (2019) Glucose transporter 1 critically controls microglial activation through facilitating glycolysis. Molecular neurodegeneration 14:1-15.

Wang X, Su B, Fujioka H, Zhu X (2008) Dynamin-like protein 1 reduction underlies mitochondrial morphology and distribution abnormalities in fibroblasts from sporadic Alzheimer's disease patients. The American journal of pathology 173:470-482.

Wang X, Su B, Zheng L, Perry G, Smith MA, Zhu X (2009) The role of abnormal mitochondrial dynamics in the pathogenesis of Alzheimer’s disease. Journal of neurochemistry 109:153-159.

Waxman S, Black J (1995) Axoglial interactions at the cellular and molecular levels in central nervous system myelinated fibers. Neuroglia Oxford University Press, Oxford:587-610.

Weinshenker BG, Rice G, Noseworthy J, Carriere W, Baskerville J, Ebers G (1991) The natural history of multiple sclerosis: a geographically based study: 3. Multivariate analysis of predictive factors and models of outcome. Brain 114:1045-1056.

Westermann B (2010) Mitochondrial fusion and fission in cell life and death. Nature reviews Molecular cell biology 11:872-884.

Wise AK, Cerminara NL, Marple-Horvat DE, Apps RJTJop (2010) Mechanisms of synchronous activity in cerebellar Purkinje cells. 588:2373-2390.

Witte ME, Nijland PG, Drexhage JA, Gerritsen W, Geerts D, van het Hof B, Reijerkerk A, de Vries HE, van der Valk P, van Horssen J (2013) Reduced expression of PGC-

1α partly underlies mitochondrial changes and correlates with neuronal loss in multiple sclerosis cortex. Acta neuropathologica 125:231-243.

Witte ME, Bo L, Rodenburg RJ, Belien JA, Musters R, Hazes T, Wintjes LT, Smeitink JA, Geurts JJG, De Vries HE, van der Valk P, van Horssen J (2009) Enhanced number and activity of mitochondria in multiple sclerosis lesions. Journal of Pathology 219:193-204.

Wu QZ, Yang Q, Cate HS, Kemper D, Binder M, Wang HX, Fang K, Quick MJ, Marriott M, Kilpatrick TJ (2008) MRI identification of the rostral-caudal pattern of pathology within the corpus callosum in the cuprizone mouse model. Journal of Magnetic Resonance Imaging 27:446-453.

Xie M, Tobin JE, Budde MD, Chen C-I, Trinkaus K, Cross AH, McDaniel DP, Song S-K, Armstrong RC (2010) Rostrocaudal analysis of corpus callosum demyelination and axon damage across disease stages refines diffusion tensor imaging correlations with pathological features. Journal of Neuropathology & Experimental Neurology 69:704-716.

Xu W, Barrientos T, Andrews NC (2013) Iron and copper in mitochondrial diseases. Cell metabolism 17:319-328.

Yan Z, Yang W, Parkitny L, Gibson SA, Lee KS, Collins F, Deshane JS, Cheng W, Weinmann AS, Wei H (2019) Deficiency of Socs3 leads to brain-targeted experimental autoimmune encephalomyelitis via enhanced neutrophil activation and ROS production. JCI Insight 4.

Yang S-H, Liu R, Perez EJ, Wen Y, Stevens SM, Valencia T, Brun-Zinkernagel A-M, Prokai L, Will Y, Dykens J (2004) Mitochondrial localization of estrogen receptor β. Proceedings of the National Academy of Sciences 101:4130-4135.

Yano R, Hata J, Abe Y, Seki F, Yoshida K, Komaki Y, Okano H, Tanaka KF (2017) Quantitative temporal changes in DTI values coupled with histological properties in cuprizone-induced demyelination and remyelination. Neurochemistry international.

Yin XH, Kidd GJ, Ohno N, Perkins GA, Ellisman MH, Bastian C, Brunet S, Baltan S, Trapp BD (2016) Proteolipid protein-deficient myelin promotes axonal mitochondrial dysfunction via altered metabolic coupling. Journal of Cell Biology 215:531-542.

Yoshiura T, Mihara F, Tanaka A, Ogomori K, Ohyagi Y, Taniwaki T, Yamada T, Yamasaki T, Ichimiya A, Kinukawa N (2003) High b value diffusion-weighted

imaging is more sensitive to white matter degeneration in Alzheimer's disease. Neuroimage 20:413-419.

Youle RJ, Van Der Bliek AM (2012) Mitochondrial fission, fusion, and stress. Science 337:1062-1065.

Yu X, Koczan D, Sulonen A-M, Akkad DA, Kroner A, Comabella M, Costa G, Corongiu D, Goertsches R, Camina-Tato M (2008) mtDNA nt13708A variant increases the risk of multiple sclerosis. PLoS One 3:e1530.

Yu-Wai-Man P, Spyropoulos A, Duncan HJ, Guadagno JV, Chinnery PF (2016) A multiple sclerosis-like disorder in patients with OPA1 mutations. Annals of clinical and translational neurology 3:723-729.

Zambonin JL, Zhao C, Ohno N, Campbell GR, Engeham S, Ziabreva I, Schwarz N, Lee SE, Frischer JM, Turnbull DM, Trapp BD, Lassmann H, Franklin RJM, Mahad DJ (2011) Increased mitochondrial content in remyelinated axons: implications for multiple sclerosis. Brain 134:1901-1913.

Zeviani M, Di Donato S (2004) Mitochondrial disorders. Brain 127:2153-2172.

Zhan J, Fegg FN, Kaddatz H, Rühling S, Frenz J, Denecke B, Amor S, Ponsaerts P, Hochstrasser T, Kipp M (2021) Focal white matter lesions induce long-lasting axonal degeneration, neuroinflammation and behavioral deficits. Neurobiology of Disease 155:105371.

Zhang J, Jones MV, McMahon MT, Mori S, Calabresi PA (2012) In vivo and ex vivo diffusion tensor imaging of cuprizone-induced demyelination in the mouse corpus callosum. Magnetic resonance in medicine 67:750-759.

Zhang K, Sejnowski TJ (2000) A universal scaling law between gray matter and white matter of cerebral cortex. Proceedings of the National Academy of Sciences 97:5621-5626.

Zheng P, Chen Q, Tian X, Qian N, Chai P, Liu B, Hu J, Blackstone C, Zhu D, Teng J (2018) DNA damage triggers tubular endoplasmic reticulum extension to promote apoptosis by facilitating ER-mitochondria signaling. Cell research 28:833-854.

Zhou B, Yu PP, Lin MY, Sun T, Chen YM, Sheng ZH (2016) Facilitation of axon regeneration by enhancing mitochondrial transport and rescuing energy deficits. Journal of Cell Biology 214:103-119.

Zlotkin SH, Lay DM, Kjarsgaard J, Longley T (1995) Determination of iron absorption using erythrocyte iron incorporation of two stable isotopes of iron (57Fe and 58Fe)

in very low birthweight premature infants. Journal of pediatric gastroenterology and nutrition 21:190-199.